

AD-A153 859

SDAC-TR-80-7b

EFFECT OF CRUSTAL STRUCTURE ON L_g

D.W. Rivers

TELEDYNE GEOTECH
Alexandria Laboratories
314 Montgomery Street
Alexandria, VA 22314

09 October 1980

Technical Report

APPROVED FOR PUBLIC RELEASE; DISTRIBUTION UNLIMITED.

Prepared for:

DEFENSE ADVANCED RESEARCH PROJECTS AGENCY
1400 Wilson Boulevard
Arlington, VA 22209

Monitored by:

AFTAC/TG
Patrick Air Force Base
Florida 32925

DTIC FILE COPY

DTIC
ELECTE
MAY 20 1985
S A D

85 4 25 015

Sponsored by
Defense Advanced Research Project Agency (DARPA)
ARPA Order No. 2551

Disclaimer: Neither the Defense Advanced Research Projects Agency nor the Air Force Technical Applications Center will be responsible for information contained herein which has been supplied by other organizations or contractors, and this document is subject to later revision as may be necessary. The views and conclusions presented are those of the authors and should not be interpreted as necessarily representing the official policies, either expressed or implied, of the Defense Advanced Research Projects Agency, the Air Force Technical Applications Center, or the US Government.

Unclassified

SECURITY CLASSIFICATION OF THIS PAGE

REPORT DOCUMENTATION PAGE

1a. REPORT SECURITY CLASSIFICATION Unclassified			1b. RESTRICTIVE MARKINGS		
2a. SECURITY CLASSIFICATION AUTHORITY			3. DISTRIBUTION/AVAILABILITY OF REPORT Approved for public release; distribution is unlimited.		
2b. DECLASSIFICATION/DOWNGRADING SCHEDULE					
4. PERFORMING ORGANIZATION REPORT NUMBER(S) SDAC-TR-80-7b			5. MONITORING ORGANIZATION REPORT NUMBER(S)		
6a. NAME OF PERFORMING ORGANIZATION TELEDYNE GEOTECH Alexandria Laboratories		6b. OFFICE SYMBOL (If applicable)	7a. NAME OF MONITORING ORGANIZATION AFTAC/TG		
6c. ADDRESS (City, State and ZIP Code) 314 Montgomery Street Alexandria, Virginia 22314			7b. ADDRESS (City, State and ZIP Code) Patrick Air Force Base Florida 32925		
8a. NAME OF FUNDING/SPONSORING ORGANIZATION DARPA		8b. OFFICE SYMBOL (If applicable)	9. PROCUREMENT INSTRUMENT IDENTIFICATION NUMBER F08606-79-C-0007		
8c. ADDRESS (City, State and ZIP Code) 1400 Wilson Boulevard Arlington, Virginia 22209			10. SOURCE OF FUNDING NOS.		
11. TITLE (Include Security Classification) (See Block 16)			PROGRAM ELEMENT NO.	PROJECT NO.	TASK NO.
				VT/9709	WORK UNIT NO.
12. PERSONAL AUTHOR(S) D. W. Rivers					
13a. TYPE OF REPORT Technical		13b. TIME COVERED FROM _____ TO _____		14. DATE OF REPORT (Yr., Mo., Day) 80-10-09	
				15. PAGE COUNT 118	
16. SUPPLEMENTARY NOTATION EFFECT OF CRUSTAL STRUCTURE ON L _g					
17. COSATI CODES			18. SUBJECT TERMS (Continue on reverse if necessary and identify by block number)		
FIELD	GROUP	SUB. GR.			
08	11		L Attenuation, Synthetic Seismogram		
			sub-g		
19. ABSTRACT (Continue on reverse if necessary and identify by block number)					
<p>→ The transverse component of the regional phase ^{sub-g}L_g was synthesized by the superposition of higher-order Love-wave modes at frequencies of up to 2.5 Hz. The synthetic seismograms represent the signals which would be generated by earthquakes at various depths in a tectonic shield. Two alternative earth models were also used: one in which the shield structure was overlain by 2 km of low-velocity sediments, and another in which this sedimentary layer was further assumed to be highly attenuating. The synthetics were used to calculate the amplitude-versus-distance relations for ^{sub-g}L_g and to analyze its phase-velocity structure as a possible depth discriminant.</p> <p>→ cont keywords include:</p> <p>The phase velocity of the synthetics was found to increase with earthquake focal depth in the shield structure, but this trend was masked by the large scatter in the data which was introduced by varying the focal mechanism and by analyzing different segments of the wavetrain. In the strongly attenuating earth structure, the ^{sub-g}L_g phase velocity</p> <p style="text-align: right;">(continued)</p>					
20. DISTRIBUTION/AVAILABILITY OF ABSTRACT UNCLASSIFIED/UNLIMITED <input checked="" type="checkbox"/> SAME AS RPT. <input type="checkbox"/> DTIC USERS <input type="checkbox"/>			21. ABSTRACT SECURITY CLASSIFICATION Unclassified		
22a. NAME OF RESPONSIBLE INDIVIDUAL Capt. Kenneth M. Ols		22b. TELEPHONE NUMBER (Include Area Code) 305-494-5263		22c. OFFICE SYMBOL TGR	

DD FORM 1473, 83 APR

EDITION OF 1 JAN 73 IS OBSOLETE.

Unclassified

SECURITY CLASSIFICATION OF THIS PAGE

19) Continued

is also dependent on the propagation path length. These complications render the L_g phase velocity to be only a weak seismic discriminant.

In the shield model with no sediments, the synthetics for shallow sources were dominated by fundamental mode Airy phases which are not observed on actual seismograms. Adding the sedimentary layer causes the fundamental mode to appear as a dispersed later phase, which is also not present in real data. The fundamental mode vanishes when the sedimentary layer is made to be strongly attenuating, but in this case the predicted amplitude decay with distance is stronger than is actually observed. In each case the synthetic L_g coda was too short. The principal reason for the disagreement between the synthetic and observed L_g seismograms is the neglect in the earth model of lateral inhomogeneities.

TABLE OF CONTENTS

LIST OF FIGURES	iv
LIST OF TABLES	viii
INTRODUCTION	1
BACKGROUND	3
SEISMOGRAM SYNTHESIS	8
RESULTS	52
Hard Rock Model	52
Soft Rock Model	69
Constant Q Model	74
Deficiency of the Model	94
CONCLUSIONS	97
REFERENCES	99
DISTRIBUTION LIST	

Accession For	
NTIS GRA&I	<input checked="checked" type="checkbox"/>
DTIC TAB	<input type="checkbox"/>
Unannounced	<input type="checkbox"/>
Justification	
By _____	
Distribution/	
Availability Codes	
Dist	Avail and/or Special
A-1	



LIST OF FIGURES

Figure No.	Title	Page
1	Shear wave velocity versus depth for the Canadian shield model with no sediments.	13
2	Density versus depth for the Canadian shield model with no sediments.	14
3	Modulus of rigidity versus depth for the Canadian shield model with no sediments.	15
4	Phase velocity versus frequency for twenty-six Love-wave modes of the Canadian shield model with no sediments.	16
5	Group velocity versus frequency for twenty-six Love-wave modes of the Canadian shield model with no sediments.	19
6	Layered medium amplitude response for twenty-six Love-wave modes of the Canadian shield model with no sediments.	21
7	Phase velocity versus frequency for twenty-eight Love-wave modes of the Canadian shield model with 1 km of sediments.	23
8	Group velocity versus frequency for twenty-eight Love-wave modes of the Canadian shield model with 1 km of sediments.	25
9	Layered medium amplitude response for twenty-eight Love-wave modes of the Canadian shield model with 1 km of sediments. The arrows indicate the strong amplitude response of the Airy phases of the first two modes, which correspond to the broad group-velocity minima in Figure 8.	26
10	Phase velocity versus frequency for twenty-nine Love-wave modes of the Canadian shield model with 2 km of sediments.	27
11	Group velocity versus frequency for twenty-nine Love-wave modes of the Canadian shield model with 2 km of sediments.	28
12	Layered medium amplitude response for twenty-nine Love-wave modes of the Canadian shield model with 2 km of sediments.	29
13	Quality factor versus frequency for twenty-nine Love-wave modes of the Canadian shield model with 2 km of sediments.	31

LIST OF FIGURES (Continued)

Figure No.	Title	Page
14	Particle displacement eigenfunction versus depth for selected Love-wave modes of the Canadian shield model with no sediments.	
	a) $f = 0.48 \text{ Hz}$	35
	b) $f = 1.48 \text{ Hz}$	36
	c) $f = 2.48 \text{ Hz.}$	37
15	Stress eigenfunction versus depth for selected Love-wave modes of the Canadian shield model with no sediments.	
	a) $f = 0.48 \text{ Hz}$	38
	b) $f = 1.48 \text{ Hz}$	39
	c) $f = 2.48 \text{ Hz.}$	40
16	Particle displacement eigenfunction versus depth for selected Love-wave modes of the Canadian shield model with 2 km of sediments.	
	a) $f = 0.48 \text{ Hz}$	41
	b) $f = 1.48 \text{ Hz}$	42
	c) $f = 2.48 \text{ Hz.}$	43
17	Stress eigenfunction versus depth for the selected Love-wave modes of the Canadian shield model with 2 km of sediments.	
	a) $f = 0.48 \text{ Hz}$	44
	b) $f = 1.48 \text{ Hz}$	45
	c) $f = 2.48 \text{ Hz.}$	46
18	Shear wave velocity versus depth for the Basin-Range model.	48
19	Phase velocity versus frequency for four Love-wave modes of the Basin-Range model.	49
20	Layered medium amplitude response for four Love-wave modes of the Basin-Range model. The fundamental mode is labelled mode 1, with modes 2-4 as the first three higher order modes.	50
21	Synthetic seismogram for a strike-slip source 0.5 km deep in the hard-rock model.	53

LIST OF FIGURES (Continued)

Figure No.	Title	Page
22	Synthetic seismogram for a strike-slip source 10 km deep in the hard-rock model.	55
23	Synthetic seismogram for a strike-slip source 20 km deep in the hard-rock model.	56
24	Synthetic seismogram for different focal mechanisms at a depth of 10 km in the hard- rock model.	57
25	Amplitudes of envelope maxima of synthetic seismograms for source at various depths in the hard-rock model. Circles: rake = 0°, dip: 90°, strike = 0°, Δ = 500 km. Triangles: rake = 40°, dip = 70°, strike = 30°, Δ = 500 km. Squares: rake = 0°, dip = 90°, strike = 0°, Δ = 1000 km.	59
26	Amplitudes of envelope maxima of synthetic seismograms for the hard-rock model as observed at various distances:	
	a) depth = 0.5 km, rake = 0°, dip = 90°: γ = 0.1229 deg	60
	b) depth = 5 km, rake = 0°, dip = 90°: γ = 0.1505 deg	61
	c) depth = 10 km, rake = 0°, dip = 90°: γ = 0.1421 deg	62
	d) depth = 20 km, rake = 0°, dip = 90°: γ = 0.1785 deg	63
	e) depth = 30 km, rake = 0°, dip = 90°: γ = 0.1778 deg	64
	f) depth = 10 km, rake = 90°, dip = 90°: γ = 0.1698 deg	65
	g) depth = 10 km, rake = 45°, dip = 60°: γ = 0.1415 deg	66
27	Synthetic seismogram for a strike-slip source 0.5 km deep in the soft-rock model.	70

LIST OF FIGURES (Continued)

Figure No.	Title	Page
28	Synthetic seismogram for a strike-slip source 10.0 km deep in the soft-rock model as observed at a distance of 500 km.	71
29	Synthetic seismogram for a strike-slip source 10.0 km deep in the soft-rock model as observed at a distance of 1000 km.	72
30	Amplitudes of envelope maxima of synthetic seismograms for sources at various depths in the soft-rock model. Circles: rake = 0°, dip = 90°, strike = 0°, Δ = 500 km. Triangles: rake = 40°, dip = 70°, strike = 30°, Δ = 500 km. Squares: rake = 0°, dip = 90°, strike = 0°, Δ = 1000 km.	73
31	Amplitudes of envelope maxima of synthetic seismograms for the soft-rock model as observed at various distances:	
	a) depth = 0.5 ₁ km, rake = 0°, dip = 90°: γ = 0.2946 deg	75
	b) depth = 3.0 ₁ km, rake = 0°, dip = 90°: γ = 0.2955 deg	76
	c) depth = 5.0 ₁ km, rake = 0°, dip = 90°: γ = 0.3041 deg	77
	d) depth = 10.0 ₁ km, rake = 0°, dip = 90°: γ = 0.2601 deg	78
	e) depth = 20.0 ₁ km, rake = 0°, dip = 90°: γ = 0.2807 deg	79
	f) depth = 30.0 ₁ km, rake = 0°, dip = 90°: γ = 0.2514 deg	80
	g) depth = 10.0 ₁ km, rake = 45°, dip = 60°: γ = 0.2760 deg	81
32	Amplitudes of envelope maxima of synthetic seismograms for sources at various depths in the high-Q soft-rock model. Circles: rake = 0°, dip = 90°, strike = 0°, Δ = 500 km. Triangles: rake = -30°, dip = 70°, strike = 40°, Δ = 500 km. Squares: rake = 0°, dip = 90°, strike = 0°, Δ = 1000 km.	84

LIST OF FIGURES (Continued)

Figure No.	Title	Page
33	Amplitudes of envelope maxima of synthetic seismograms for the high-Q soft-rock model as observed at various distances:	
	a) depth = 0.5 ₁ km, rake = 0°, dip = 90°: γ = 0.2096 deg	86
	b) depth = 3.0 ₁ km, rake = 0°, dip = 90°: γ = 0.1704 deg	87
	c) depth = 5.0 ₁ km, rake = 0°, dip = 90°: γ = 0.1538 deg	88
	d) depth = 10.0 ₁ km, rake = 0°, dip = 90°: γ = 0.1555 deg	89
	e) depth = 20.0 ₁ km, rake = 0°, dip = 90°: γ = 0.1665 deg	90
	f) depth = 30.0 ₁ km, rake = 0°, dip = 90°: γ = 0.1632 deg	91
	g) depth = 10.0 km, rake = 45 ₁ °, dip = 60°, strike = 40°: γ = 0.1611 deg	92
	h) depth = 10.0 km, rake = 70 ₁ °, dip = 70°, strike = 40°: γ = 0.1820 deg	93

LIST OF TABLES

Table No.	Title	
I	Canadian Shield Earth Model (from Brune & Dorman, 1963).	12
II	Phase Velocities for Synthetic Waveforms Generated Using the Hard-Rock Model.	68
III	Phase Velocities for Synthetic Waveforms Generated Using the Soft-Rock Model.	82
IV	Temporal Variation of the Measured L _g Phase Velocity.	95

INTRODUCTION

In the earliest years of the application of seismic techniques to the investigation of nuclear explosions and their discrimination from earthquakes, very little emphasis was placed on observations made at short distances from the seismic source. Recently, however, there has arisen the possibility of negotiating a treaty which would permit the USA to install seismic stations inside the USSR, and so attention is being paid to the analysis of measurements made at regional distances. With the techniques which have been developed in the years subsequent to the early investigations of regional seismology, particularly the advances which have been made in the application of digital computers to a variety of complex problems, it may now be possible to analyze quantitatively many of the complicated features of regional seismograms which hampered the previous studies.

If regional seismic phases such as P_n , P_g and L_g are to be used for event location, discrimination, and/or yield estimation, it will be necessary to understand the mechanism responsible for their generation and the effects of the geological medium on their propagation. For example, the rate of decay of the signal amplitude with distance must be known in order to determine the event magnitude from the observations, but several previous studies summarized by Pomeroy et al. (1982) have shown that the decay rates of regional phases are strongly dependent upon the particular source-to-receiver propagation path and that the amplitudes are also strongly dependent upon the geological structure at the observation site (Der et al., 1981). Path- and site-dependent effects also hinder any simple interpretation of other signal measurements, such as the coda duration or the phase velocity, in terms of seismic source characteristics such as depth. If regional phases are to be used to study the earthquakes or explosions which generate them, then, it will be necessary to evaluate quantitatively the effects introduced into the observed records by the propagation paths and the receiver sites. The effects of local structure at the receivers have been investigated in certain previous studies (e.g., Barker et al., 1980a; Der et al., 1980); in this report we shall examine the effects of the propagation path. On account of its structural simplicity and its

relevance to the geology of the USSR, we shall concentrate on an earth model of a tectonic shield, with and without sedimentary cover. We shall restrict our discussions to the single phase L_g , but we shall also discuss briefly how our methodology might be generalized to incorporate other regional phases as well.

BACKGROUND

In 1952 Press and Ewing identified as distinct seismic phases two short-period surface waves which were observed to propagate across North America. The phase which was characterized by particle motion transverse to the direction of propagation was designated " L_g ", and the phase which exhibited Rayleigh-type particle motion was designated " R_g ". The subscript "g" referred to the granitic layer of the crust, along the base of which the two phases were conjectured to propagate. It was soon shown, however, that these surface waves are observationally complex and hence that the simple "granitic" model for their propagation is inadequate. In particular, Bath (1954) divided the L_g wavetrain into two distinct arrivals, which he denoted as " L_{g1} " and " L_{g2} ", and Bath (1954) and Gutenberg (1955) showed that the L_g particle motion is not simply transverse but that it has large vertical and radial components as well. These investigations proposed that the observations should be explained by considering L_g and R_g to be channel waves in the crust or upper mantle, i.e., waves which propagate along a low-velocity zone (LVZ) waveguide capped by a higher-velocity lid. A major step towards understanding the true nature of L_g was taken by Oliver and Ewing (1957; 1958a,b), who noted that the group velocities of prominent maxima in the L_g wavetrain correspond to stationary points in the group velocity-versus-frequency dispersion curves for higher-mode Love waves. The distinct arrivals such as L_{g1} and L_{g2} were therefore identified as Airy phases, and their amplitudes and rates of decay could be predicted using well-known formulas derived by means of the stationary phase approximation (e.g., Bath, 1968, Chapter 3).

The identification of the transverse component of L_g as the superposition of higher-mode Love waves has permitted the observed group velocities of that regional phase to be used as a tool in the computation of earth models, since the values of the group velocity minima in the dispersion curves are sensitive to the details of the layered structure which is responsible for the Love-wave propagation. Kovach and Anderson (1964) calculated the group velocities for low-frequency L_g waves in order to test various assumed values for the thickness and the shear-wave velocity of the LVZ in the mantle. For the low-frequency

surface waves which are affected by such deep structures, Kovach and Anderson (1964) demonstrated that the group velocities must be calculated for a spherical, rather than a flat, layered earth model. An important result of these computations of the group velocity minima for higher-mode Love waves in various earth models is that no high-velocity lid overlying a crustal LVZ is required for L_g propagation, at least at the low frequencies ($f \leq 1.0$ Hz) considered by these authors. Instead, a simple layered crustal structure in which the shear-wave velocity increases monotonically with depth can be used for many of the observed features of L_g . In this report we shall use such a structure with no crustal LVZ in order to study the propagation of L_g in a tectonic shield region.

Schwab and Knopoff (1971) investigated the effect of anelasticity upon the phase velocities and group velocities of higher-mode Love waves. They showed that introducing a realistic value of the shear-wave figure of merit Q_β into the calculations produces only a small change in the values which are determined for the velocities, a result which we shall use when we analyze the effect upon L_g of an attenuating sedimentary layer overlying the shield structure. By examining the Love-wave particle motion as a function of both depth and frequency for several higher modes, Schwab and Knopoff (1971) also showed that for an earth model appropriate for an oceanic region, most of the low-frequency L_g energy is transported by LVZ channel waves in the mantle. If, as they assumed, Q_β is low in the LVZ, the energy would thus be damped out rather rapidly by elastic attenuation. By means of this mode-by-mode and frequency-by-frequency analysis of the effect of anelasticity on the particle displacement at depth, Schwab and Knopoff (1971) were able to provide a plausible explanation of the failure of L_g to propagate across long oceanic paths. Although the shield model which we shall consider in this report contains no crustal LVZ and although L_g is unaffected by the mantle LVZ at the high frequencies which we shall consider, we shall find this same method of analysis useful for explaining the differences in L_g propagation which are introduced when an attenuating sedimentary layer is added to the shield structure.

An important development in the analysis of the phase L_g was the generation of synthetic seismograms by Knopoff et al. (1973). These investigators used the phase velocity-versus-frequency relations and the stress and particle displacement-versus-depth relations described previously, and they combined them with the excitation coefficients for the various higher modes which were computed by assuming various double-couple source mechanisms. The Love-wave higher modes were summed and transformed from the frequency domain into the time domain, resulting in synthetic seismograms which exhibited many of the observed features of L_g . The synthetics were a convincing demonstration of the identification of L_g as the sum of higher-mode Love waves, an identification which had previously been surmised simply on the basis of the group-velocity minima, since the synthetics displayed not only the proper group velocities but also the proper amplitudes and frequency content. Knopoff et al. (1973) also showed by means of these synthetic seismograms that, contrary to the original conjectures of Bath (1954) and Gutenberg (1955) but in accordance with the results of Kovach and Anderson (1964), no crustal LVZ is necessary for the propagation of L_g . Realistic L_g seismograms can be synthesized by assuming a crustal model composed of layers for which the shear-wave velocity increases monotonically with depth. In this report we shall verify that this result holds at higher frequencies than the cutoff ($f = 1.0$ Hz) which was apparently used by Knopoff et al. (1973).

Computation of higher-mode Love-wave group-velocity minima and L_g synthetic seismograms was also used by Knopoff et al. (1974) to determine shear-wave velocity profiles for different types of continental crustal structures. Because the synthetics were generated for the long-period WWSSN instrument, lower frequencies and deeper earth models were used in that study than will be considered in this report, but many of their results are important for understanding the characteristics of L_g which are observed on short-period instruments as well. In particular, Knopoff et al. (1974) found that both the minimum group velocity and the period of the lowest-frequency Airy phase for each Love-wave mode increase monotonically with crustal thickness. By scaling the crustal thickness from a continental to an oceanic earth model,

Knopoff et al. (1979) showed why L_g does not propagate through even short paths of oceanic crust (as opposed to the upper mantle, which was investigated by Schwab and Knopoff (1971)). The absence of oceanic L_g can be attributed to the scaling with crustal thickness of the dispersion curves, surface-wave scattering due to lateral variations in oceanic sediment thickness, and anelastic attenuation in the sediments. These same features will also be important, although to a lesser extent, in our examination of L_g propagation through attenuating sediments in a continental earth model.

All of the analyses of L_g which have been mentioned thus far have considered particle motion in only the transverse direction. This restriction was brought about by the modeling of L_g as the superposition of many Love-wave modes, all of which have, of course, only a transverse component of motion. It was shown by Bath (1954) and Gutenberg (1955), however, that L_g has a significant vertical component of motion. A quantitative explanation of both this and vertical and the radial components of L_g was provided by Panza and Calcagnile (1975), who demonstrated that these components are the superposition of higher-mode Rayleigh waves. They also demonstrated that the phase R_g is the fundamental Rayleigh mode and that no LVZ in either the crust or the upper mantle is necessary for the propagation of either R_g or the Rayleigh-type of L_g motion. Although we shall confine our synthetic seismograms to the superposition of Love-wave modes and hence to the transverse component only, we shall show the necessity of including the Rayleigh modes in order to reproduce observed signals. If the phase L_g is to be used as a seismic discriminant, it will be important to understand the partitioning of surface-wave energy between SH-type and P-SV-type motion.

In this report we have undertaken to utilize the modal superposition technique in order to answer some questions about L_g propagation which ought to be understood if L_g is to be used in a program of seismic discrimination and yield determination at regional distances. In particular, it is well known that L_g not only fails to propagate through the ocean but also attenuates rapidly in certain continental regions. It is also known that the amplitude of L_g , as well as its group velocity, is

strongly influenced by surficial geology. In order to interpret observations of L_g in terms of the source mechanism, as well as to choose the best sites for locating future seismic stations, it is important to have a quantitative estimate of these path effects. We should also like to know, for a given source-to-receiver earth model, how large a variability in the characteristics of L_g can be anticipated from earthquakes of different source mechanisms and of different depth. It is especially important to know whether certain earthquakes have some L_g signal characteristics which can be used as diagnostics in discrimination studies. Our study of L_g synthetic seismograms has been aimed at investigating these questions.

SEISMOGRAM SYNTHESIS

The theory of surface-wave propagation through a stratified medium is addressed in a host of previous studies; herein we shall discuss only a few points of the theory which are relevant to the generation of the synthetic seismograms. Our synthetics were calculated using formulas for far-field surface waves given by Mendiguren (1977), which we shall not reproduce herein. The actual computation of the quantities which appear in these formulas, however, was performed using a computer program based on the method of Harkrider (1970). We are able to make this substitution since the results obtained by both methods are equivalent, although the method of Mendiguren (1977) permits the use of a more general seismic source function than does the method of Harkrider (1970), which considers only certain specific source functions. Since all of our synthetic seismograms will be based upon one of these special cases, namely a double-couple source mechanism, the two formulations may be considered identical except for differences in notation and sign conventions.

In order to generate synthetic surface-wave seismograms, the following quantities must be computed:

1) the seismic source function. Since our synthetics are meant to be valid for the far-field displacement only, we assume that the seismic source is of infinitesimal spatial extent and thus may be represented by a second-order moment tensor, M_{ij} . For the special case of a double-couple mechanism, the nine terms of this moment tensor (only six of which are distinct) can be expressed in terms of the strike and dip of the fault plane and the rake of the slip vector. We should point out that if an isotropic explosion rather than a double couple were used as the source mechanism, the moment tensor would become simply $M_{ij} = M_0 \delta_{ij}$, in which case there is no shear displacement at the source and all Love-wave motion would therefore disappear. We are thus unable to model the transverse component of L_g from an explosion, since it is the departures from the idealized case which give rise to the transverse component of motion, and we shall restrict our analyses to idealized earthquakes instead. We shall assume that the seismic source

is a temporal step function, although we can generate the synthetics equally well using some other source time function if we wish to do so.

2) the phase velocity of the surface waves as a function of frequency. For a given earth model consisting of a vertical sequence of constant-thickness, flat strata in which the density and the compressional- and shear-wave velocities are specified, the computation of the Love-wave and Rayleigh-wave phase velocities for any frequency is an eigenvalue program (the "period equation") which may be solved by the well-known matrix method expounded by Haskell (1953) and formalized by Gilbert and Backus (1966). We will find a sequence of roots as the solution to this eigenvalue problem, corresponding to the sequence of fundamental and higher modes.

3) the transfer function of the earth model. This term, denoted for the Love and Rayleigh waves as A_L and A_R by Harkrider (1970) and as $1/2C_{U I_1}^{L L}$ and $1/2C_{U I_1}^{R R}$ by Mendiguren (1977), is inversely proportional to the integral over depth of the kinetic energy density of the surface wave. This term shows the excitation of motion at the surface by a wave with a given frequency and a given mode number.

4) the stress and particle displacement as a function of both frequency and depth. For the Love wave this involves only the transverse direction, but for the Rayleigh wave both the vertical and radial components must be calculated. The stress and the displacement may be found by substituting back into the period equation each root which was found for that equation, resulting in an eigenfunction for every frequency and each mode. This computation involves a product of matrices, one matrix for each layer in the earth model, which "propagate" the surface boundary conditions downward to the focal depth of the source. This product of "propagator" matrices may be numerically unwieldy, since round-off errors will be compounded by each successive multiplication and thus will increase with depth. We have therefore found it necessary to impose a priori upon the computation the constraint that the eigenfunctions in the bottom layer decay exponentially. The error in the multiplication of the propagator matrices will of course be increased greatly by inaccuracy in the

calculation of the roots of the period equation. The calculation of these roots is in fact an error-prone process, since the eigenvalue equation is based on the vanishing of a determinant which is subject to significant numerical imprecision due to round-off. For the Love waves, the propagator matrices describe the stress and displacement in only one component and thus are 2×2 matrices; for the Rayleigh waves, there are two components and so the matrices are 4×4 , causing the determinantal equation to be more difficult to solve accurately than is the case for the Love waves, particularly at high frequencies. The imprecision in the eigenvalues leads to eigenfunctions which are sometimes ill behaved with depth. It is therefore easier to synthesize the Love-type motion of L_g than the Rayleigh-type motion.

5) the azimuth and distance from the seismic source to the point of observation. The azimuth, measured with respect to the same reference frame as are the source function coefficients M_{1j} , gives the location of the observer on the radiation pattern of the source mechanism for Love and for Rayleigh waves. We shall make the distance dependence of the amplitudes of our synthetic seismograms slightly more realistic by replacing Mendiguren's (1977) assumption of cylindrical wavefront spreading with a term appropriate to the spreading of a wavefront on the surface of a sphere:

$$\text{amplitude} \propto (R_0 \sin(r/R_0))^{-1/2}$$

where r is the source-to-receiver distance and R_0 is the radius of the earth. We reserve for later a discussion of how the decay of amplitude with distance is affected by anelastic attenuation.

On account of its prevalence in many different regions of the world, including the USSR, the earth model which we shall use for studying L_g propagation is that of a tectonic shield. We shall take our model from the study of the Canadian shield by Brune and Dorman (1963). The use of this particular shield model may facilitate the comparison of our synthetics with observed seismograms recorded at North American stations, and we anticipate that the synthetics generated with this model will have many salient features in common with those which would

be generated using shield models appropriate to other continents. The model of Brune and Dorman (1963) is reproduced in Table I. We note that since our L_g synthetics are confined to Love-wave motion, we shall not use the tabulated values of the P-wave velocity. The shear-wave velocity, density, and modulus of rigidity are illustrated as functions of depth in Figures 1-3. It is shown in those figures that, as a computational aid, we have subdivided the bottom layer of the crust so that the transition to the mantle is slightly less abrupt than is the case in Table I. This subdivision of the transition zone will improve the accuracy of the computations at high frequencies, since imprecision can result if the exponentially attenuating layer in which the particle motion dies out is allowed to be many wavelengths thick. By making the base of the crust into several layers, this problem is avoided, since the program ignores the sublayers below the depth at which (for a given frequency) the particle motion vanishes. We see that there is no crustal LVZ for this shield model. The mantle LVZ, which lies at a depth of greater than 100 km, will have little effect upon L_g at the frequencies which we shall consider in this report. For this hard-rock model, a value of 1000 has been chosen for shear wave figure of merit Q , independent of both frequency and depth. Such an assumption represents the limiting case of only slight attenuation of L_g .

Figure 4 shows how the phase velocity of each the first twenty-six Love-wave modes behaves as a function of frequency from 0.02 to 2.50 Hz. For the sake of visual clarity, the odd-numbered modes (counting the fundamental as mode 1) are shown as solid lines and the even-numbered modes as shown as dashed lines. Phase velocities greater than 4.51 km/sec are not considered, because this cut-off corresponds to the shear-wave velocity in the mantle LVZ (cf. Table I). The Love-wave modes osculate at this phase velocity, so the separate curves shown in Figure 4 link up at the velocity $C_L = 4.51$ km/sec to form a continuous curve which is almost flat across the entire frequency range of 0.02 to 2.50 Hz. The separate modes thus combine to form a single non-dispersive phase propagating at the shear wave velocity of the mantle LVZ, and an examination of the behavior with depth of the particle displacement eigenfunctions reveals that this phase is in fact the mantle LVZ channel

TABLE I

Canadian Shield Earth Model
(from Brune and Dorman, 1963).

Layer Thickness (km)	Depth at Bottom (km)	P-Wave Velocity (km/sec)	S-Wave Velocity (km/sec)	Density (gm/cm ³)
6.0	6.0	5.64	3.47	2.70
10.5	16.5	6.15	3.64	2.80
18.7	35.2	6.60	3.85	2.85
80.0	115.2	8.10	4.72	3.30
100.0	215.2	8.20	4.54	3.44
100.0	315.2	8.30	4.51	3.53
80.0	395.2	8.70	4.76	3.60
∞	∞	9.30	5.12	3.76

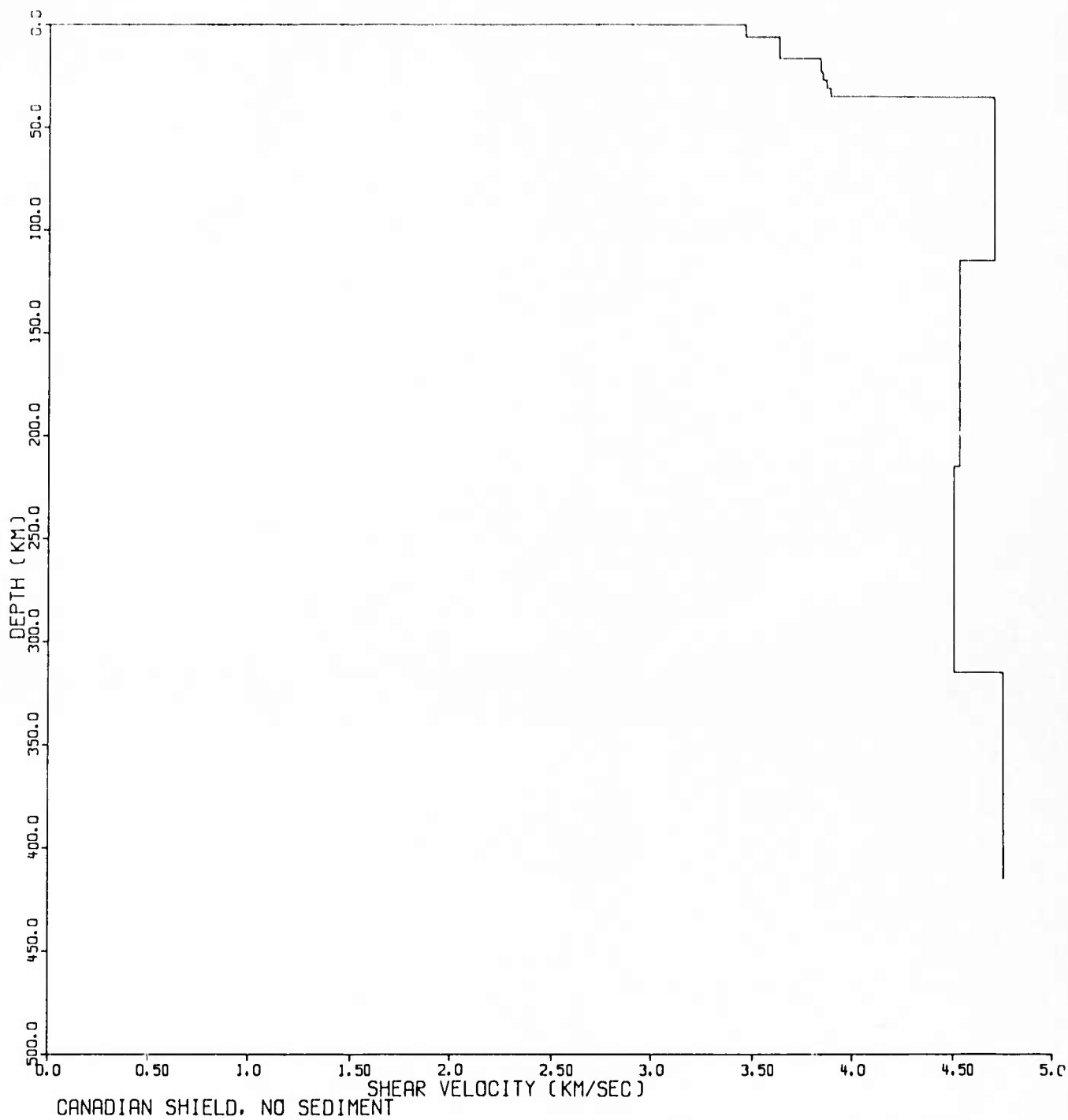


Figure 1. Shear wave velocity versus depth for the Canadian shield model with no sediments.

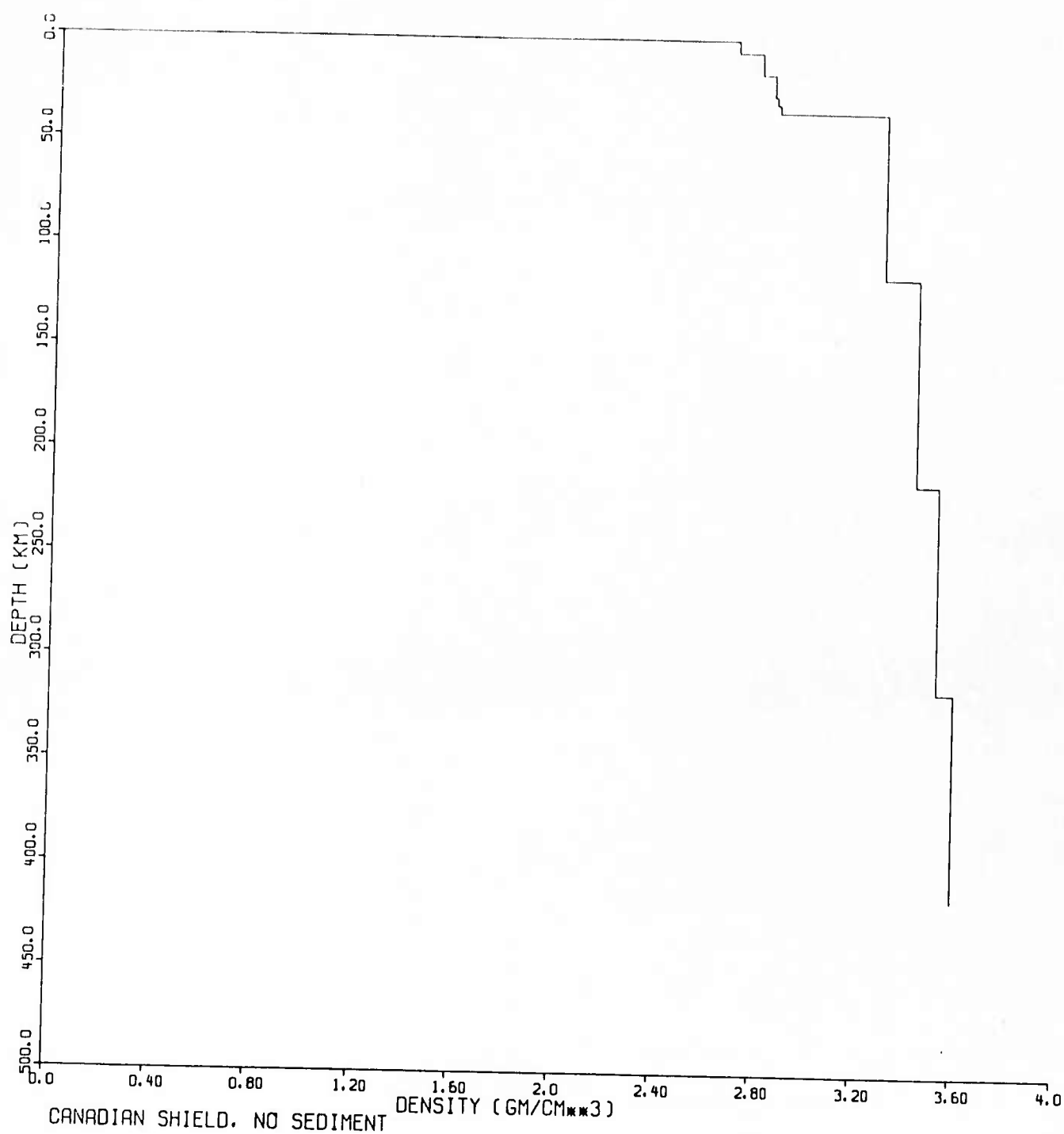


Figure 2. Density versus depth for the Canadian shield model with no sediments.

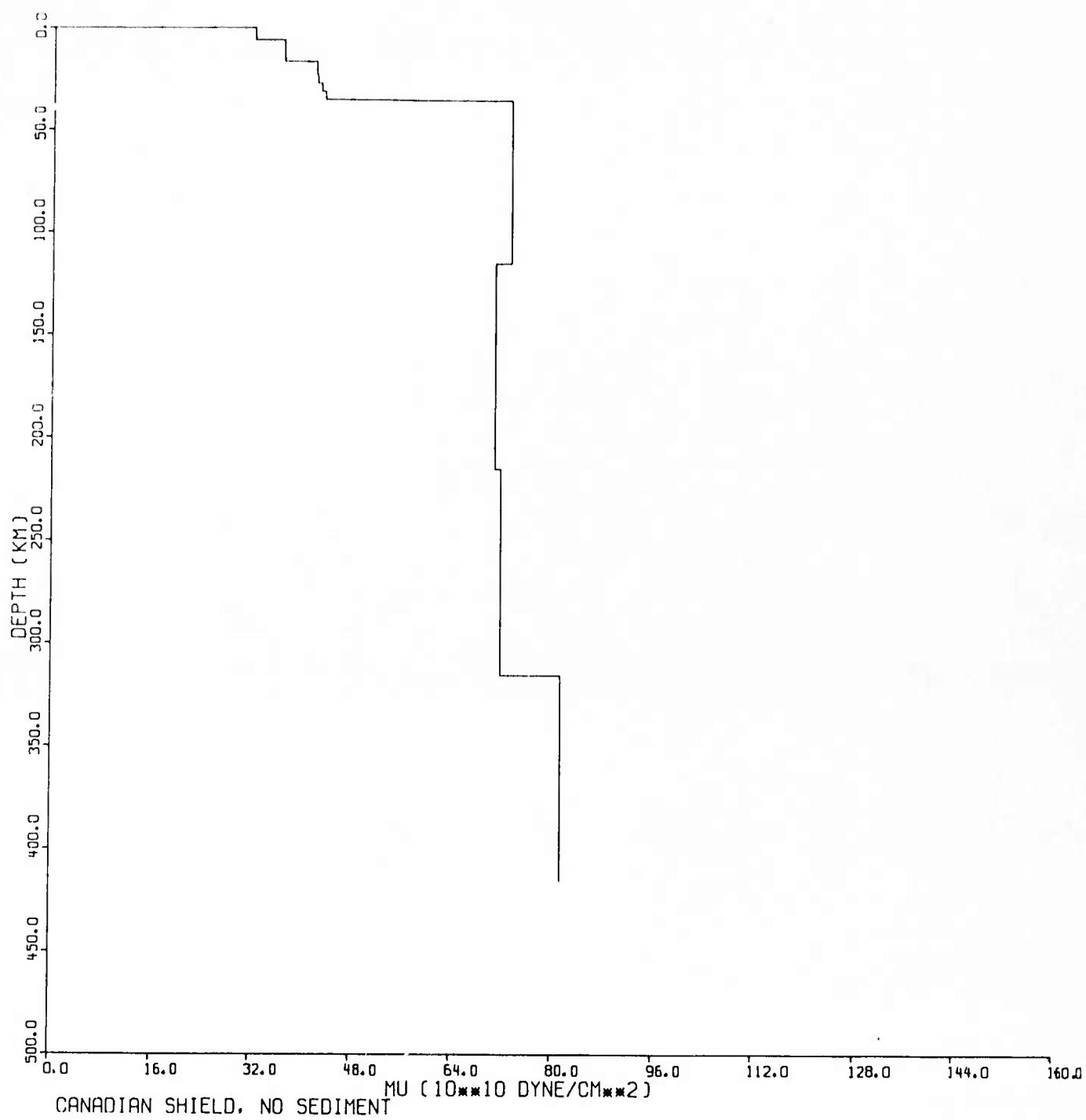


Figure 3. Modulus of rigidity versus depth for the Canadian shield model with no sediments.

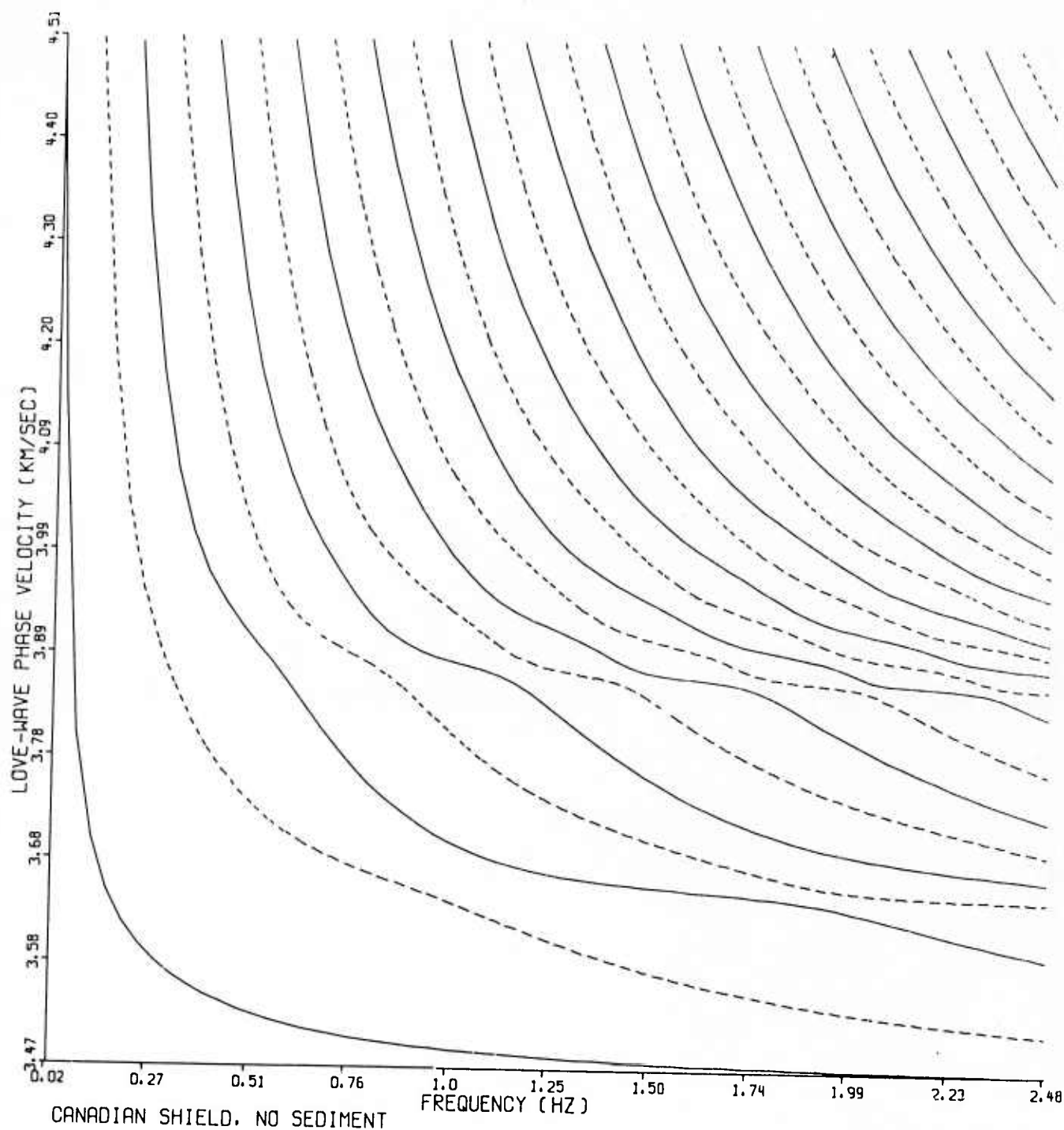


Figure 4. Phase velocity versus frequency for twenty-six Love-wave modes of the Canadian shield model with no sediments.

wave S_n . The generation of S_n by the superposition of higher Love-wave modes is examined in detail by Stephens and Isacks (1977) and by Mantovani et al. (1977). Because S_n is a guided wave in the LVZ, it is inefficient at exciting motion at the earth's surface, a fact which is demonstrated by the very small values which are computed for the propagation medium transfer function for frequencies at which the Love-wave phase velocities are greater than 4.51 km/sec. We are therefore justified in limiting our synthetic seismograms to the velocity range shown in Figure 4, $C_L < 4.51$ km/sec, effectively defining " L_g " for our purposes as being "that portion of the transverse component of motion which occurs after the S_n arrival." The cut-off in frequency of 2.5 Hz was chosen for computational efficiency; our synthetic seismograms will have this cut-off as their Nyquist frequency, and hence they will be generated at a sampling rate of 5 samples per second. This data density is high enough for a reasonable comparison with L_g as observed on most short-period seismographs. Twenty-six modes were treated because these are all the Love-wave modes there are (for this particular model) for which the roots of the period equation lie within the two ranges $C_L < 4.51$ km/sec and $f < 2.50$ Hz.

It is instructive to compare the graph of the phase velocity-versus-frequency dispersion relation shown in Figure 4 with the velocity profile listed in Table I. The figure shows that at high frequencies the phase velocity of the fundamental mode asymptotically approaches the shear-wave velocity at the earth's surface. Since the graph is almost horizontal at this velocity, the fundamental mode becomes almost nondispersive, so we expect that the energy contained in this mode will arrive in almost a single pulse at high frequencies. In several figures to be shown later, we shall demonstrate that the fundamental mode does in fact have a prominent Airy phase with a group velocity of 3.47 km/sec which causes the synthetic seismograms for this mode to be impulse-like.

Figure 4 shows further that the higher modes approach, but do not reach, osculatory behavior at phase velocities equal to the shear-wave velocities in the second and third layers within the crust (cf. Table I). This nearly osculating behavior reflects a tendency of the sharp

interfaces between the crustal layers to act as waveguides, trapping by successive reflections the higher-mode energy within the individual layers as crustal channel waves. Because the modes do not actually osculate, these crustal channel waves do not fully develop; we shall see, however, that the medium transfer function does exhibit minima at the frequencies and mode numbers corresponding to the nearly horizontal segments of the graphs in Figure 4, showing that these points of near-osculation represent values at which L_g is inefficient at generating particle motion at the earth's surface. We note that the modes would truly osculate and crustal channel waves would be formed in a structure with a crustal LVZ, such as the Basin and Range province of the southwestern United States.

Figure 5 shows the group velocity as a function of frequency for the twenty-six Love-wave modes. Although the group-velocity values of course represent the derivative $2\pi \cdot df/dk_L$ which would be calculated numerically from the values of $C_L(f) = 2\pi f/K_L$ shown in Figure 4, the group velocities were in fact calculated directly from Haskell's (1953) matrices using Harkrider's (1970) computer program. The curves shown in Figure 5 are thus an analytic, rather than a numerical, result (although they are subject to the same numerical imprecisions as are the other quantities which are computed from the products of the propagator matrices). Inspection of the figure shows that, as was anticipated on the basis of Figure 4, the fundamental mode has a very broad group-velocity minimum at $U_L = 3.47$ km/sec. The higher modes have a complex pattern of stationary points at which Airy phases will occur. Since most of the energy will propagate at the velocities corresponding to the Airy phases, Figure 5 shows that most of the energy in the L_g phase travels at velocities of between 3.41 and 3.81 km/sec in the hard rock Canadian shield model. This range exceeds the velocity which is commonly taken for L_g propagation $U_{Lg} = 3.54$ km/sec. We shall later adjust our earth model in order to reconcile this discrepancy, but first we shall compute the synthetic seismograms and thereupon see how much energy is predicted to arrive with these high velocities.

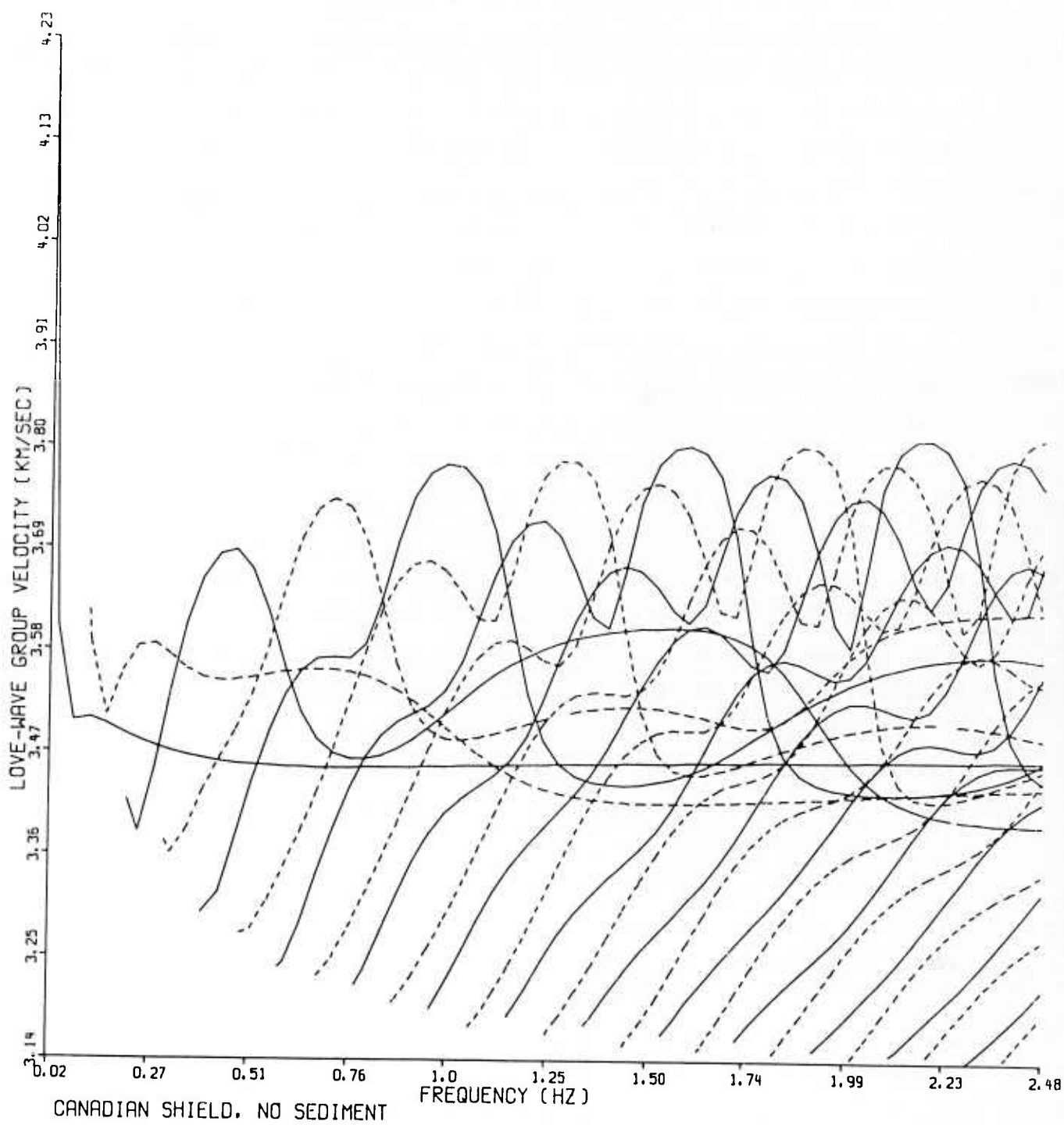


Figure 5. Group velocity versus frequency for twenty-six Love-wave modes of the Canadian shield model with no sediments.

Some idea of the frequency- and modal-dependent distribution of energy in L_g is given by the medium amplitude response, or transfer function, which is shown in Figure 6. The transfer function is a measure of the efficiency of each mode for producing motion at the earth's surface as a function of frequency. More exactly, treating the layered earth structure as a linear network, the transfer function is the frequency-dependent ratio of an output (in microns of particle motion) at the surface, to input (in dynes of the impulse) which generated that motion. We emphasize that this is not equivalent to the surface motion which would be generated by an arbitrary seismic source, since the transfer function must be multiplied in the frequency domain by an appropriate source function. For a double-couple mechanism, for example, the spatial orientation of the double couple determines the relative excitation of the stress and particle displacement eigenfunctions, so the transfer function must be multiplied by a quantity which is dependent upon frequency, mode number, and focal depth. What the transfer function does show is the surface motion's dependence upon frequency and mode number when the other parameters are held constant. In particular, it shows the surface response to an event which is itself at the surface, since in this special case the stress eigenfunctions vanish and the (normalized) particle displacement eigenfunctions yield a value of unity, independent of frequency and mode number. This significance of the transfer function is reinforced by an examination of Figure 6, which in light of the previous discussion may be interpreted as showing that for a surface source only the first three modes make a major contribution to the surface motion of L_g within the frequency band of interest. This is hardly surprising, since the propagation of these modes is confined to shallow depths, as we shall subsequently demonstrate, and hence they are more easily excited by a surface source than are the higher modes which propagate at greater depths. In this discussion we are using the "depth of propagation" in a rather nebulous sense, which we shall refine later, to indicate the distribution with depth of the kinetic energy density. Figure 6 also shows that, all other factors being held constant (which, we emphasize, they actually will not be), most of the low-frequency energy present in L_g would be contained within the fundamental and first higher Love-wave modes. This

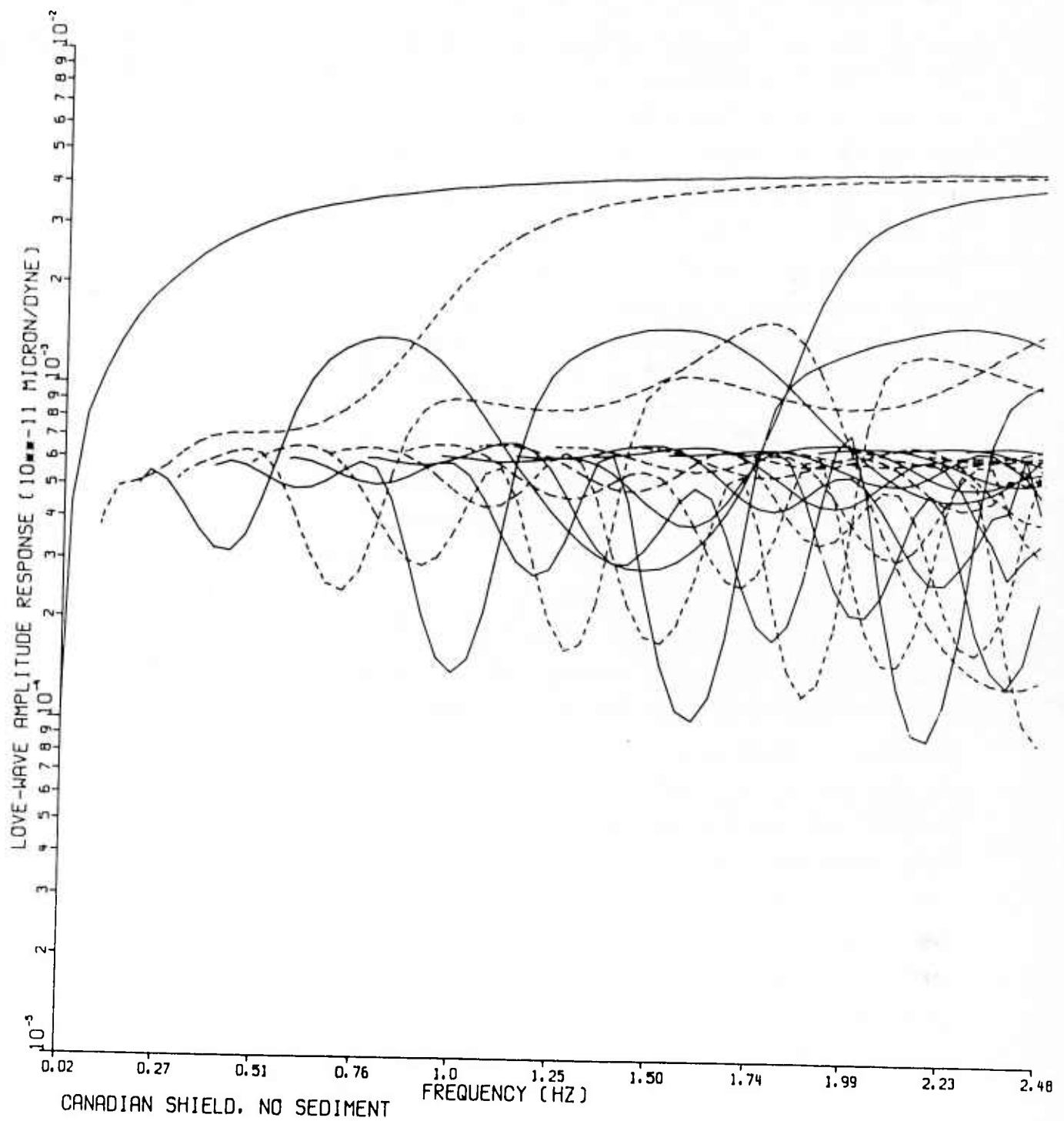


Figure 6. Layered medium amplitude response for twenty-six Love-wave modes of the Canadian shield model with no sediments.

concentration of low-frequency energy will be especially significant later, when we alter our hard-rock model by adding a sedimentary layer through which these shallow modes will propagate. Finally, we note the pattern in Figure 6 of prominent minima in the transfer functions. A comparison with Figure 4 reveals that, as we had anticipated, the nulls in the amplitude response occur at the same frequencies and mode numbers (e.g., mode 7 at 1.56 Hz) as do the nearly horizontal segments of the phase velocity-versus-frequency graphs. The flat portions of these graphs correspond to channel wave-like behavior of those modes, which at those frequencies propagate mainly in waveguides within the crust and hence are inefficient at generating motion at the surface.

In addition to computing synthetic L_g seismograms using the earth model whose parameters are illustrated in Figures 1-6, we will wish for the sake of comparison to generate L_g synthetics using an alternate earth model. In particular, we will wish to examine the effect upon L_g propagation of a sedimentary layer overlying the shield structure. This alternate earth model of a tectonic shield with a sedimentary cover will be applicable, in at least a gross sense, to many regions of the world, such as central North America, and we anticipate that a wide range of potential characteristics which L_g may exhibit will be bounded by the two extremes of the hard-rock and the soft-rock cases. We shall thus consider the effect of replacing the topmost 1 km of the hard-rock earth model described in Table I by a 1 km-thick sedimentary layer which we shall take to have a shear-wave velocity of 2.11 km/sec and a density of 2.39 gm/cm³. These values were deliberately chosen to be significantly smaller than those in the hard-rock case, so that the effect upon L_g of adding the sediments would be prominent. Figure 7 shows that adding the sedimentary layer affects the phase velocity of the lowest-order modes most strongly. This behavior of the dispersion relation is predictable, since it is the lowest-order modes which propagate largely in the topmost layer and whose phase velocity asymptotically approaches at high frequency the shear-wave velocity of the sediments. The higher-order modes penetrate deeper into the crust, so they are less perturbed by the presence of the sedimentary veneer.

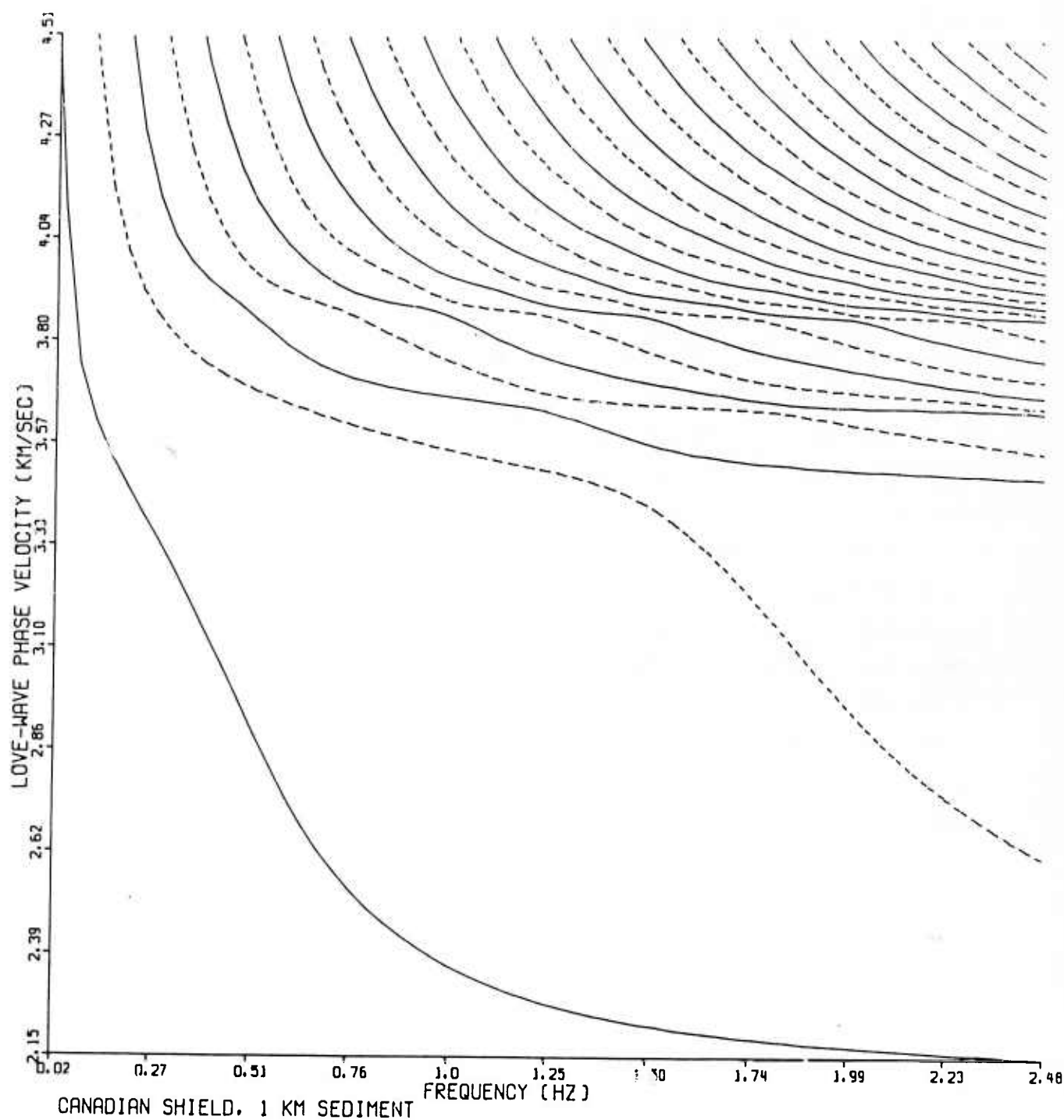


Figure 7. Phase velocity versus frequency for twenty-eight Love-wave modes of the Canadian shield model with 1 km of sediments.

The sedimentary layer has a dramatic effect not only on the phase velocity but also on the group velocity of the lowest-order modes, as is shown in Figure 8. This graph indicates that L_g propagation in this earth model will be characterized by two strong phases arriving significantly later than the rest of the energy in the signal: first a low-frequency (≈ 0.6 Hz) Airy phase due to the fundamental mode, and then a high-frequency one (≈ 2.15 Hz) due to the first higher mode. In the discussion which follows, we shall discuss why waveforms with this unusual signature will not be observed in practice.

Figure 9 shows that not only do the two Airy phases arrive much later than the rest of the signal but they also are much greater in amplitude than the preceding L_g arrivals. Specifically, the figure indicates that the layered medium's amplitude response is quite large for the two lowest modes, especially at frequencies close to or greater than those corresponding to the group-velocity minima in Figure 8. We once again point out that in the process of generating the synthetic seismograms, the values shown in Figure 9 must be multiplied by frequency-, modal-, and depth-dependent source terms, so the two prominent lowest order modes may not be excited for a given particular case. Figure 9 does show, however, that these two modes will be more prominent for a seismogram generated using the soft-rock model than for one with the same source mechanism and focal depth in the hard-rock model. This difference should especially be evident for shallow events, which excite the lowest modes preferentially, and in particular it should be prominent for events with hypocenters within the sedimentary layer.

In Figures 10-12 the effect is shown of increasing the thickness of the sedimentary layer from 1 km to 2 km. The phenomena which were described in Figures 7-9 are seen to be enhanced, but the changes are less dramatic than those which were introduced by the addition of the 1 km of sediments to the hard-rock model. In our synthetics we shall use the 2-km thick sediments rather than the 1-km thick layer in order to maximize the differences between the hard-rock and the soft-rock cases.

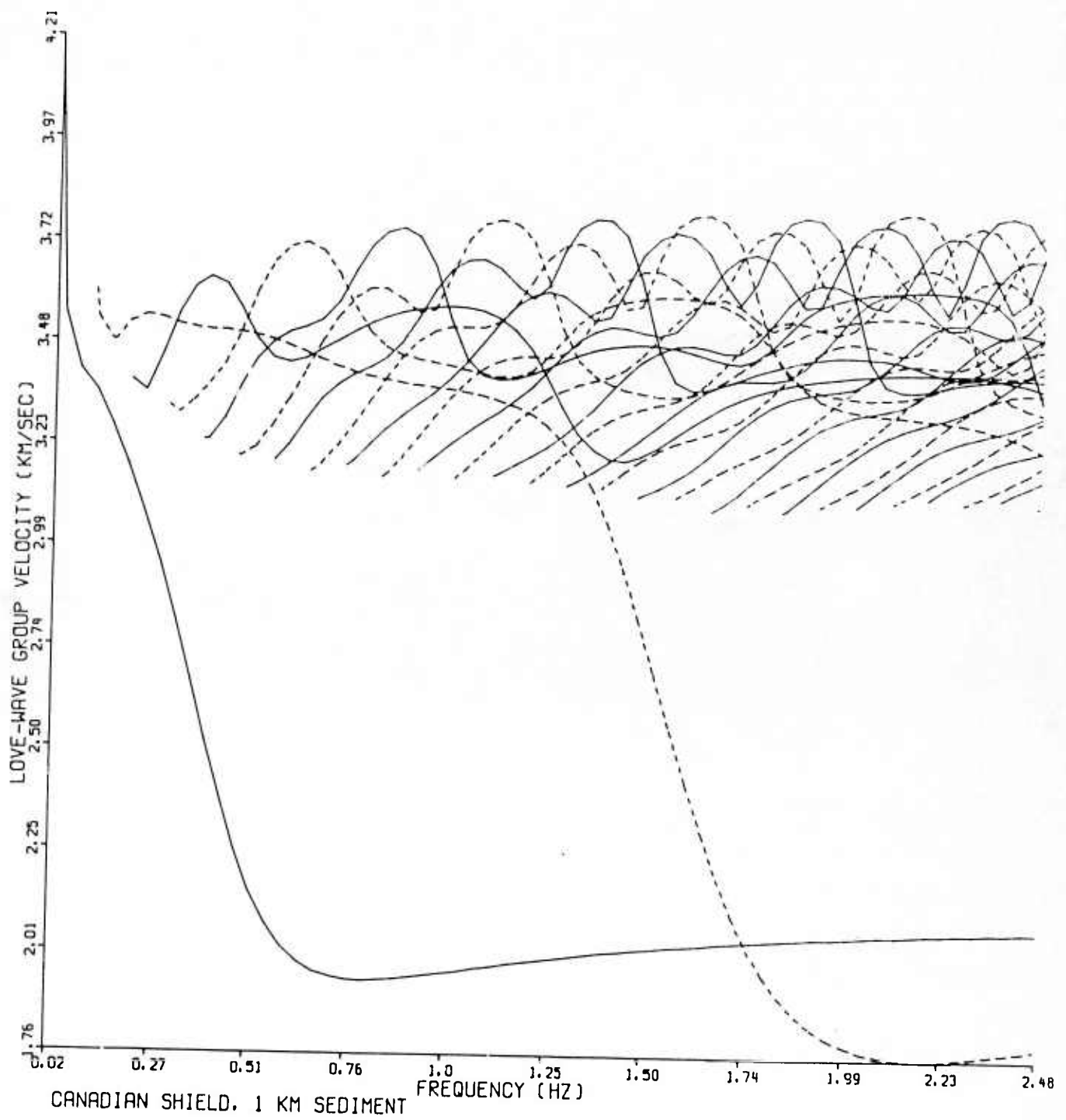


Figure 8. Group velocity versus frequency for twenty-eight Love-wave modes of the Canadian shield model with 1 km of sediments.

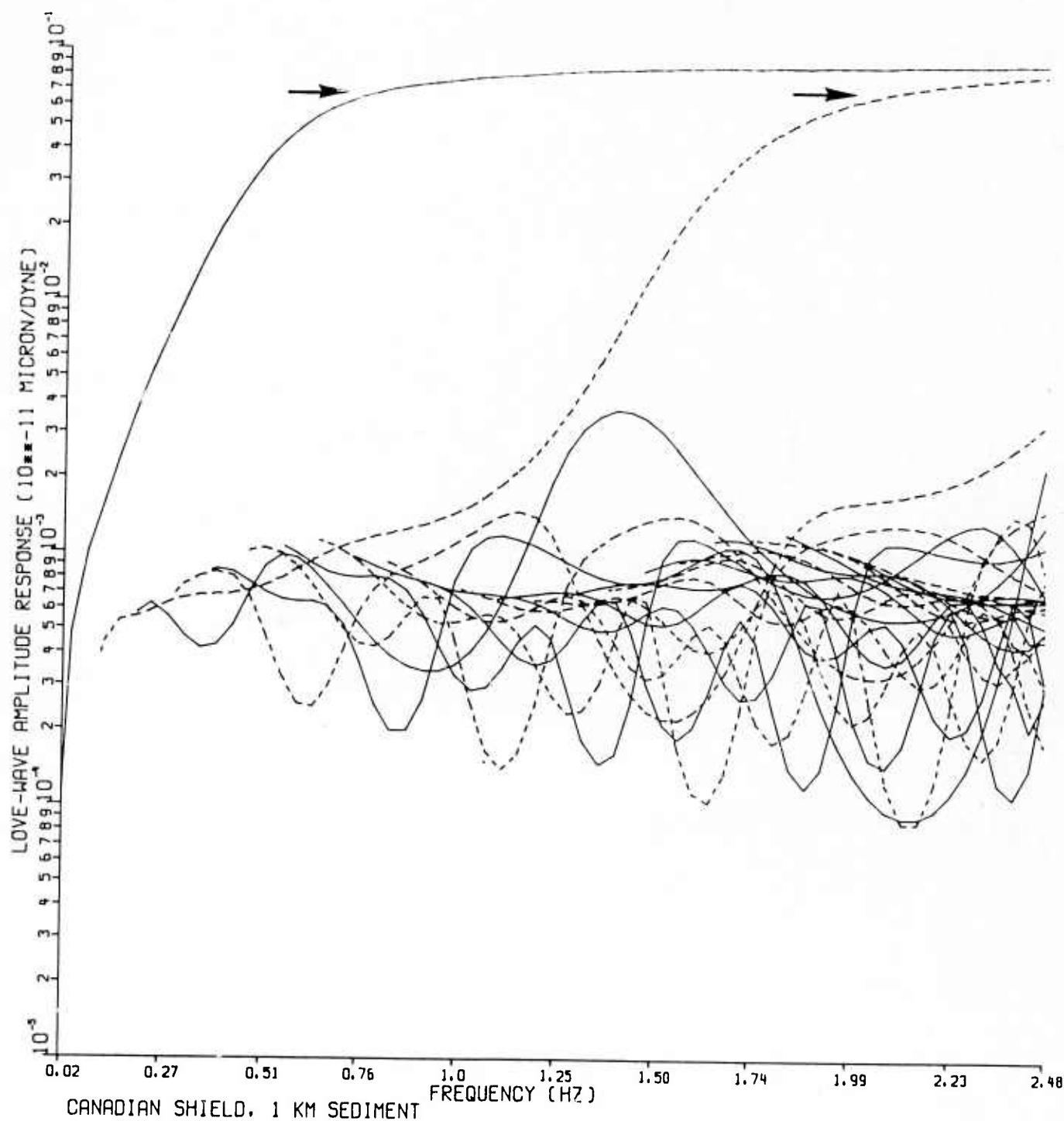


Figure 9. Layered medium amplitude response for twenty-eight Love-wave modes of the Canadian shield model with 1 km of sediments. The arrows indicate the strong amplitude response of the Airy phases of the first two modes, which correspond to the broad group-velocity minima in Figure 8.

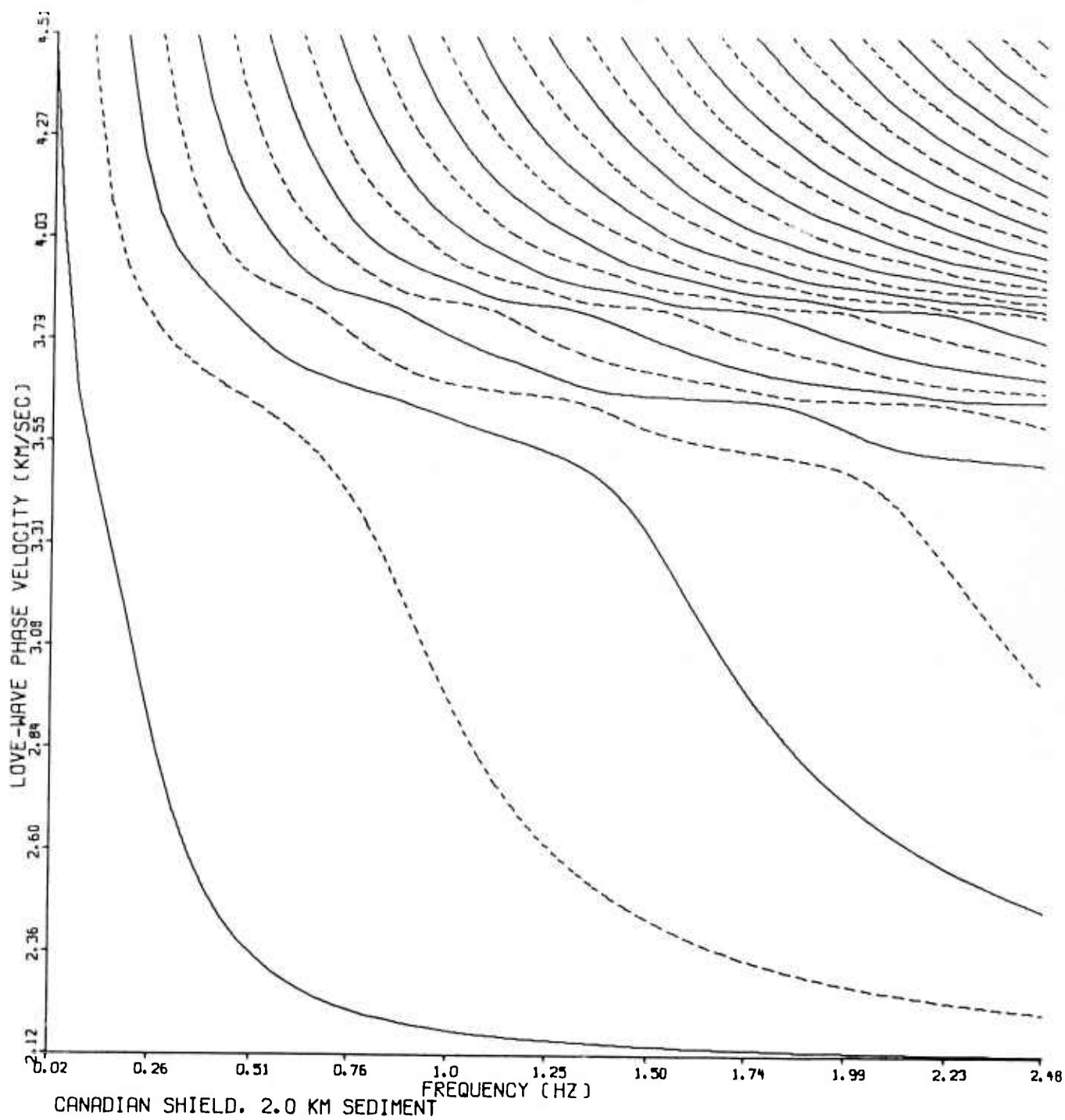


Figure 10. Phase velocity versus frequency for twenty-nine Love-wave modes of the Canadian shield model with 2 km of sediments.

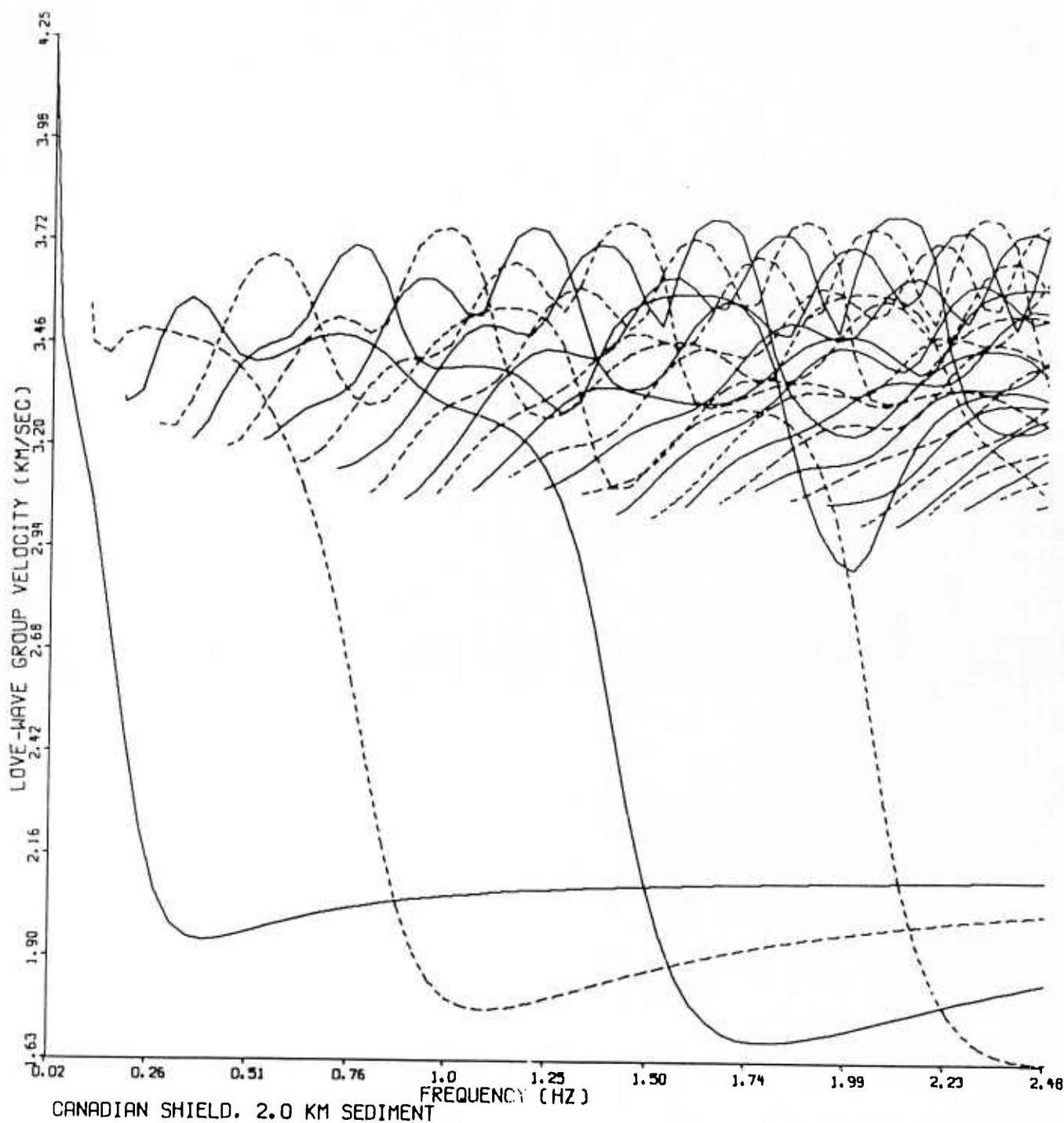


Figure 11. Group velocity versus frequency for twenty-nine Love-wave modes of the Canadian shield model with 2 km of sediments.

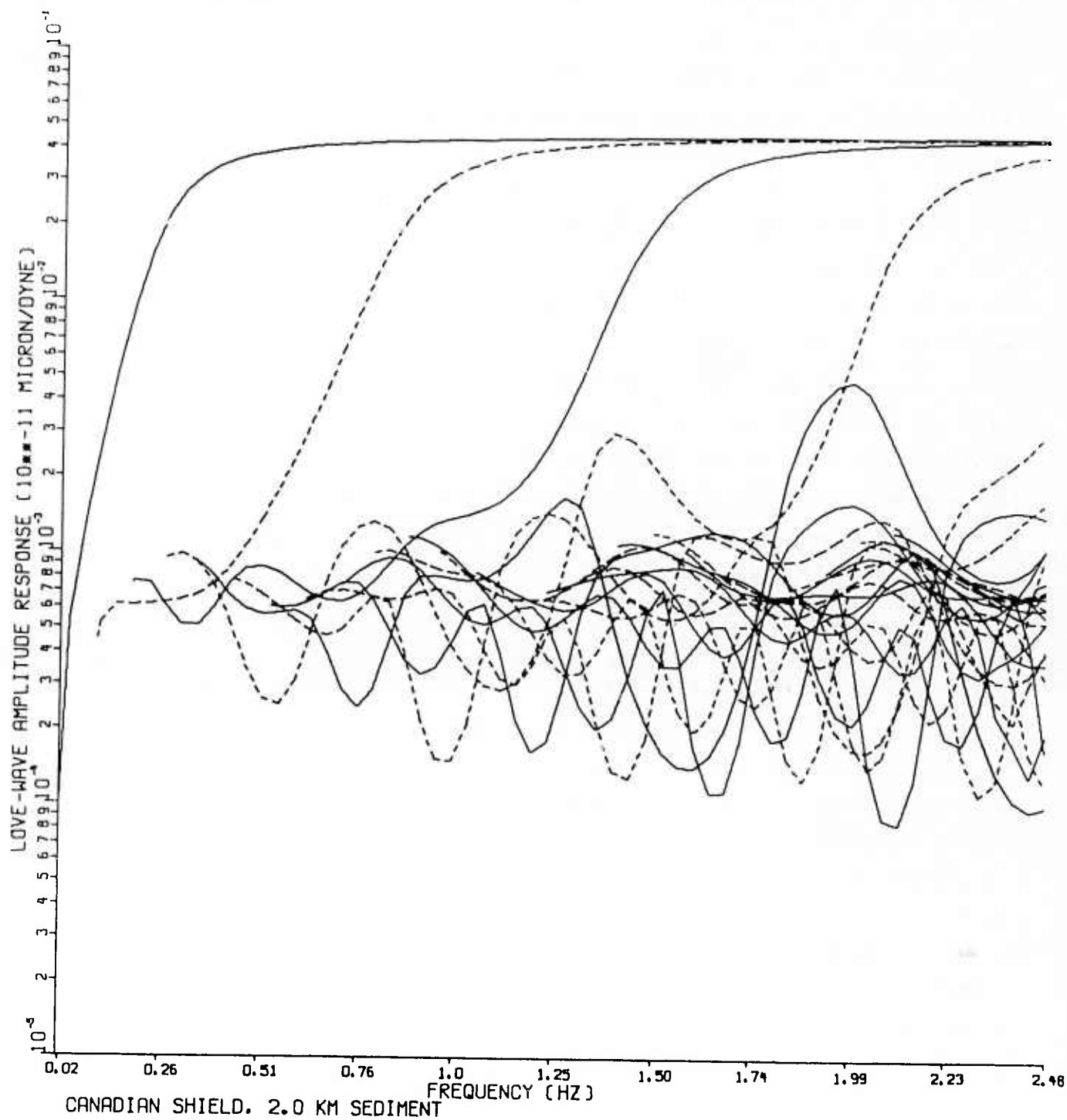


Figure 12. Layered medium amplitude response for twenty-nine Love-wave modes of the Canadian shield model with 2 km of sediments.

Figure 13 illustrates the effect of anelastic attenuation, which was not shown for the hard-rock model. The reason for ignoring attenuation in the discussion of the hard-rock model is that in that particularly simple case, for which the shear-wave quality factor Q_β was assigned the frequency-independent value 1000 in every layer, the trivial result is obtained that $Q_L = 1000$ for all Love-wave modes and all frequencies. In the soft-rock model, however, Q_β is a function of depth, and Q_L is a complicated function of frequency and of mode number. In order to emphasize the effect of attenuation in the soft-rock case, we have set $Q_\beta = 20$ in the 2-km thick sedimentary layer, independent of frequency. This anomalously low value of Q_β was deliberately chosen in order to model a "worst possible case" of attenuation by a sedimentary layer. As we have already discussed, the use of the hard-rock model in the synthetic seismograms leads to the appearance of prominent fundamental-mode Airy phases which are not observed in actual seismograms of L_g . One way to diminish the contribution of the fundamental mode to the synthetics is to make the value of Q much lower in the topmost layer than in the underlying crust, thereby preferentially damping out the shallowest modes. This "worst possible case" model will serve to illustrate the effects of the sedimentary layer by maximizing them; in a realistic earth model, the attenuation will be significantly less than that which is shown in Figure 13, so we expect realistic L_g behavior to be bounded by the extremes of our hard-rock and soft-rock limits. As typical of the values of the anelasticity quality factor which one might expect to observe in the earth, we note that Bache et al. (1978) inverted Rayleigh-wave data (which, like Love waves, are sensitive mainly to Q_β rather than Q_α) measured at periods of $T \geq 3.0$ sec to obtain an earth model for the Nevada Test Site-to-Albuquerque profile consisting of a 2.5-km thick layer for which $Q_\beta = 20$, a 21.5-km thick layer for which $Q_\beta = 300$, and an 18-km thick layer for which $Q_\beta = 1000$. Since we are concerned with shorter-period surface waves than those which were analyzed by Bache et al. (1978), we expect the upper-layer value of Q_β to be significantly higher than the value of $Q_\beta = 20$ which they found and which is used in Figure 13. We shall therefore examine alternative methods to the introduction of an anomalously low Q in order to diminish the contribution to L_g of the fundamental mode.

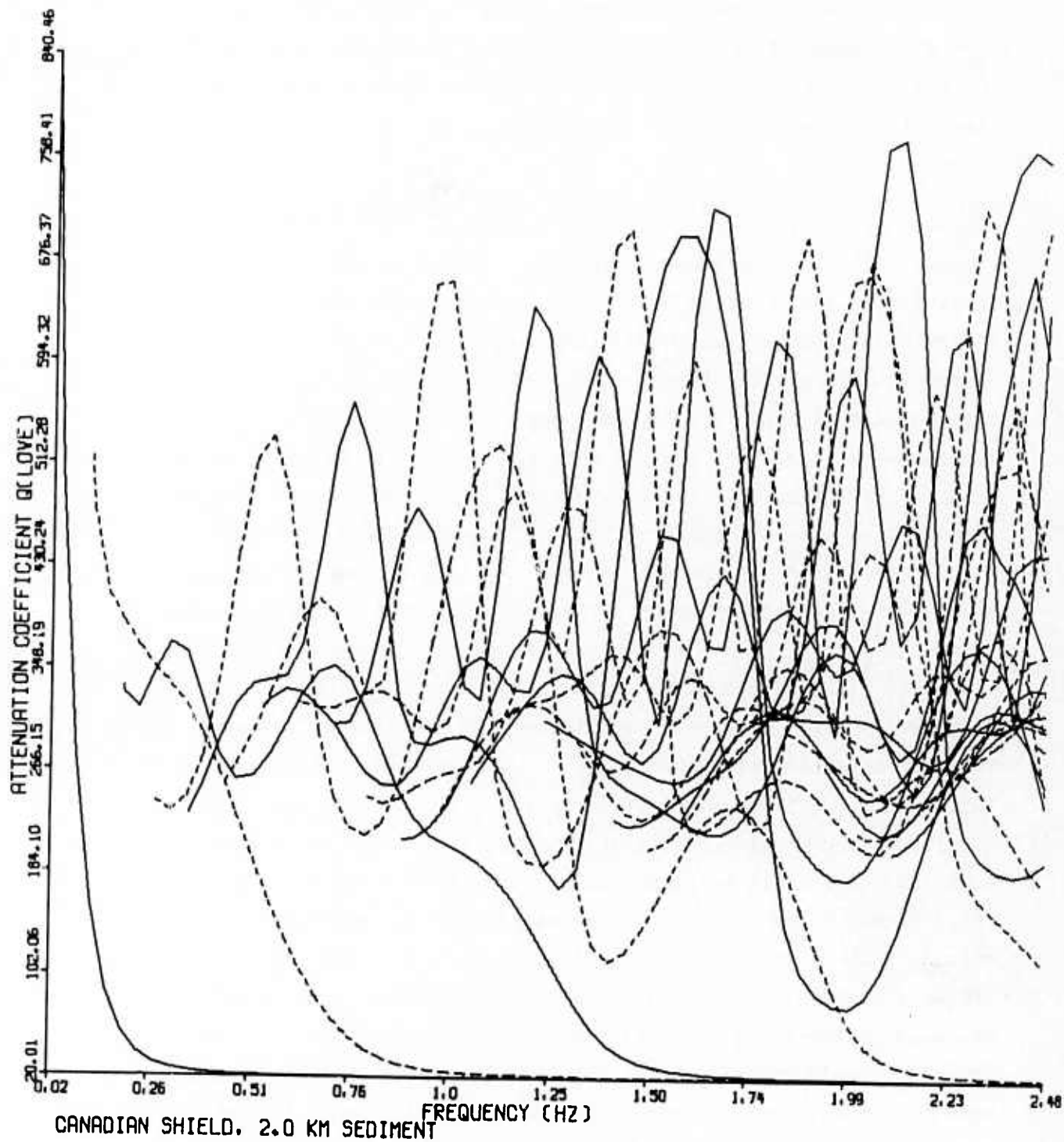


Figure 13. Quality factor versus frequency for twenty-nine Love-wave modes of the Canadian shield model with 2 km of sediments.

For our worst-case (i.e., most strongly attenuating) model, we set $Q_\beta = 20$ independent of frequency in the surficial layer, and we obtain the frequency- and modal-dependent values for Q_L which are shown in Figure 13. These curves were calculated using the formula

$$Q_L^{-1} = \sum_{i=1}^N (2\mu_i U_L / c_L^2) (\partial c_L / \partial \mu_i) Q_{\beta i}^{-1} \text{ for } N \text{ layers} \quad (1)$$

(Knopoff, 1964). The behavior of this function is difficult to estimate intuitively, but we are able to anticipate certain gross features of Figure 13 by considering the behavior with depth of the particle displacement eigenfunctions for the various modes. At low frequencies, the fundamental mode "sees" (i.e., has a significant particle displacement) down into the upper mantle, and so it is not greatly affected by the attenuation in the top 2 km of the crust. At higher frequencies, however, there is little fundamental-mode particle displacement at depth, and so the mode is largely confined to the attenuating sedimentary layer. The quality factor Q_L thus effectively becomes $Q_{\beta \text{sediments}}$, as is shown in Figure 13. A similar behavior is exhibited by the first higher mode. Figure 13 shows that Q_L for all modes of number 3 or higher oscillates with increasing frequency before decaying asymptotically to $Q_{\beta \text{sediments}}$. The reason for this oscillating behavior is that the eigenfunctions for these modes, which will be illustrated shortly, oscillate with depth, and as the frequency increases there will be an increasing amount of a vertical "wavelength" (in a rather loose sense) of these oscillations contained within the topmost 2 km of the crust. If, for a given mode number and a given frequency, the particle displacement eigenfunction is large in the top 2 km, much of the energy of that mode will be attenuated. If the frequency is increased so that the "wavelength" of the oscillations with depth is diminished, the eigenfunction will have a null rather than a maximum in the topmost 2 km, so most of the energy in the mode at that frequency is localized below the attenuating layer and Q_L is therefore 'more representative of the lower crust. The figure of merit Q_L thus oscillates in frequency as alternating maxima and nulls in the eigenfunctions move into the sedimentary layer.

Figure 13 shows an important frequency dependence of Q_L for the lowest-order modes in this earth model: the sedimentary layer causes the crust to behave like a low-pass filter. This situation contrasts with that of the higher-order modes, for which Q_L is not a monotonic function of frequency. It is instructive to compare the quality factor in Figure 13 with the transfer function in Figure 12. The graphs of the lowest-order modes exhibit complimentary behavior in the two figures, with Q_L becoming small at those frequencies where A_L becomes large. This means that, as was indicated earlier, the prominent Airy phases which would be anticipated on the basis of Figures 11 and 12 will in fact not be seen, because they will damp out rapidly with increasing source-to-receiver separation as the energy which is confined to the sedimentary layer diminishes due to anelasticity.

The soft-rock values of Q_L which are shown in Figure 13 and the constant hard-rock value $Q_L = 1000$ will be applied to the synthetic seismograms by computing an attenuation coefficient

$$\gamma_L(f) = \pi f / (Q_L(f) U_L(f)).$$

This coefficient will be applied to the amplitudes by multiplying each point in the frequency-domain seismogram by $\exp(-\gamma_L r)$ where r is the source-to-receiver separation in km. Even though anelasticity affects not only the amplitude but also the velocity of seismic waves, we shall not consider the influence of Q_β on the phase and group velocities of L_g , since this is a small effect (Schwab and Knopff, 1971). As evidence of this smallness (for realistic values of Q_β), we note that at the frequencies under consideration body waves may effectively be treated as nondispersive. Another approximation which we have made with regard to attenuation is that Q_β is independent of frequency. Across the frequency band under consideration, this approximation is probably a poor one. We shall nevertheless disregard the behavior of Q_β with frequency, since we are more interested in its behavior with depth. The approximation $Q_\beta(f) = \text{constant}$ is more nearly valid than is the deliberately exaggerated approximation $Q_\beta(h) = 20 + 880H(h-2)$, where h denotes depth and H is the Heaviside step function. Our soft-rock model is thus meant to be more nearly a limiting case than a realistic model,

and we shall not introduce higher order corrections into it. Instead we shall present alternative methods to this model for diminishing the influence of the fundamental mode at shallow depths.

The particle displacement and stress eigenfunctions, to which reference was made in the preceding discussion, are shown in Figures 14 and 15 for the hard-rock model and in Figures 16 and 17 for the soft-rock model. In each figure the eigenfunctions are shown for three specific frequencies and for several specific mode numbers. (Refer to Figures 4 and 10 in order to see how many modes exist with $C_L < 4.51$ km/sec at each of these three frequencies.) We wish to point out several features of these plots and explain their significance for L_g propagation. First, it is important to note that the transverse displacement eigenfunctions are normalized to a value of unity at the surface and that the different modes are not plotted to the same scale. The stress eigenfunctions vanish at the surface, and in some cases this means that the stress changes rapidly from zero at zero depth to the first value which is shown on the plots, at a depth of 0.1 km. This rapid change will not concern us, since we shall consider no focal depths of less than 0.5 km, and it is the value of the eigenfunctions only at the depth of the hypocenter which enters into the source function. Next, we note that the eigenfunctions are in certain cases somewhat ill behaved in the layer immediately above that layer in which they cease to oscillate and instead decay exponentially (i.e., the depth at which $\beta > C_L$). Part of this behavior is due to the familiar problem of cumulative numerical imprecision in the multiplication of a sequence of propagator matrices, and part is due to the true behavior of the eigenfunctions in the region which marks the transition from sinusoidal to exponential behavior (the "turning point" of the WKBJ approximation). We also point out that the first derivative with respect to depth of the tangential stress eigenfunctions is discontinuous at the interfaces between the layers defined in Table I; this discontinuity is due to the discontinuities of the modulus of rigidity as a function of depth (cf. Figure 3). Finally, we point out that Figures 14 and 16 illustrate a phenomenon which we have mentioned several times previously, namely the concentration of energy at shallow depths for the lowest-order modes

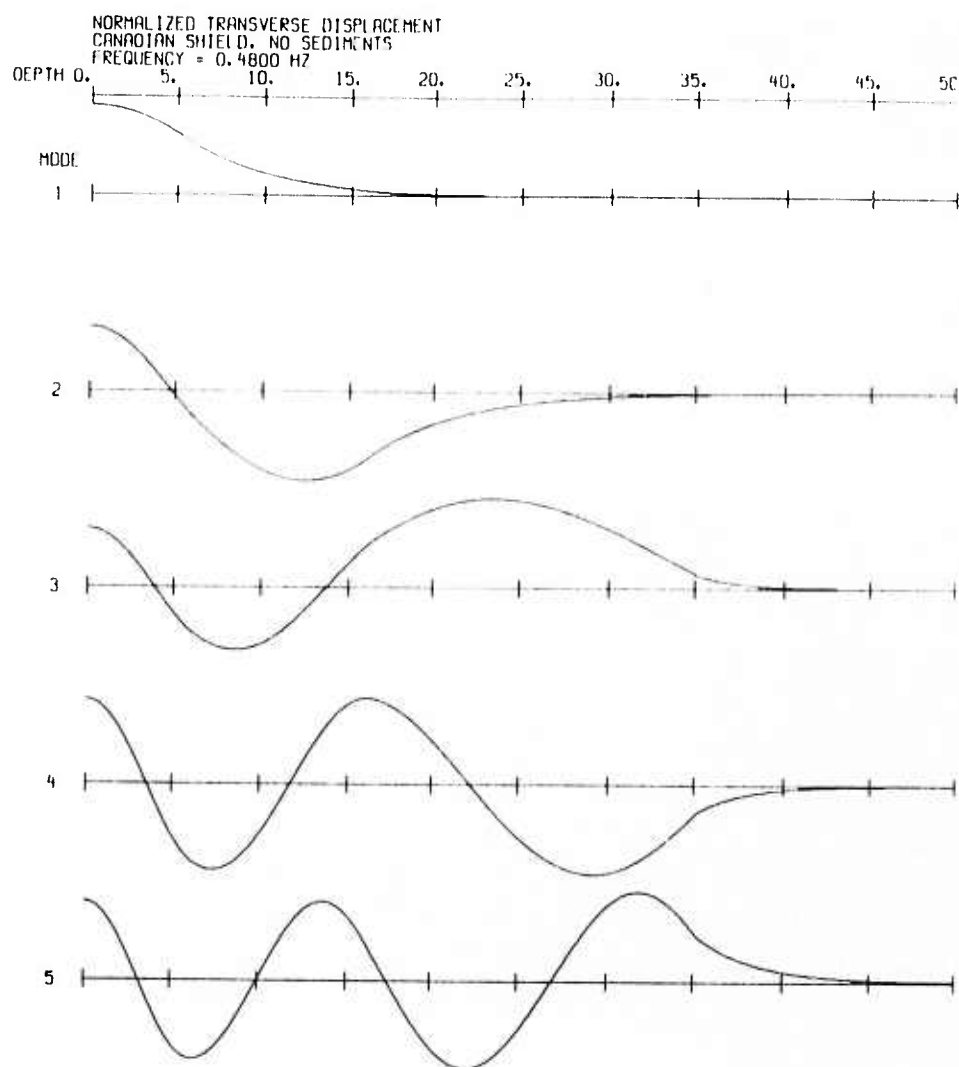


Figure 14a. $f = 0.48$ Hz
Particle displacement eigenfunction versus depth
for selected Love-wave modes of the Canadian
shield model with no sediments.

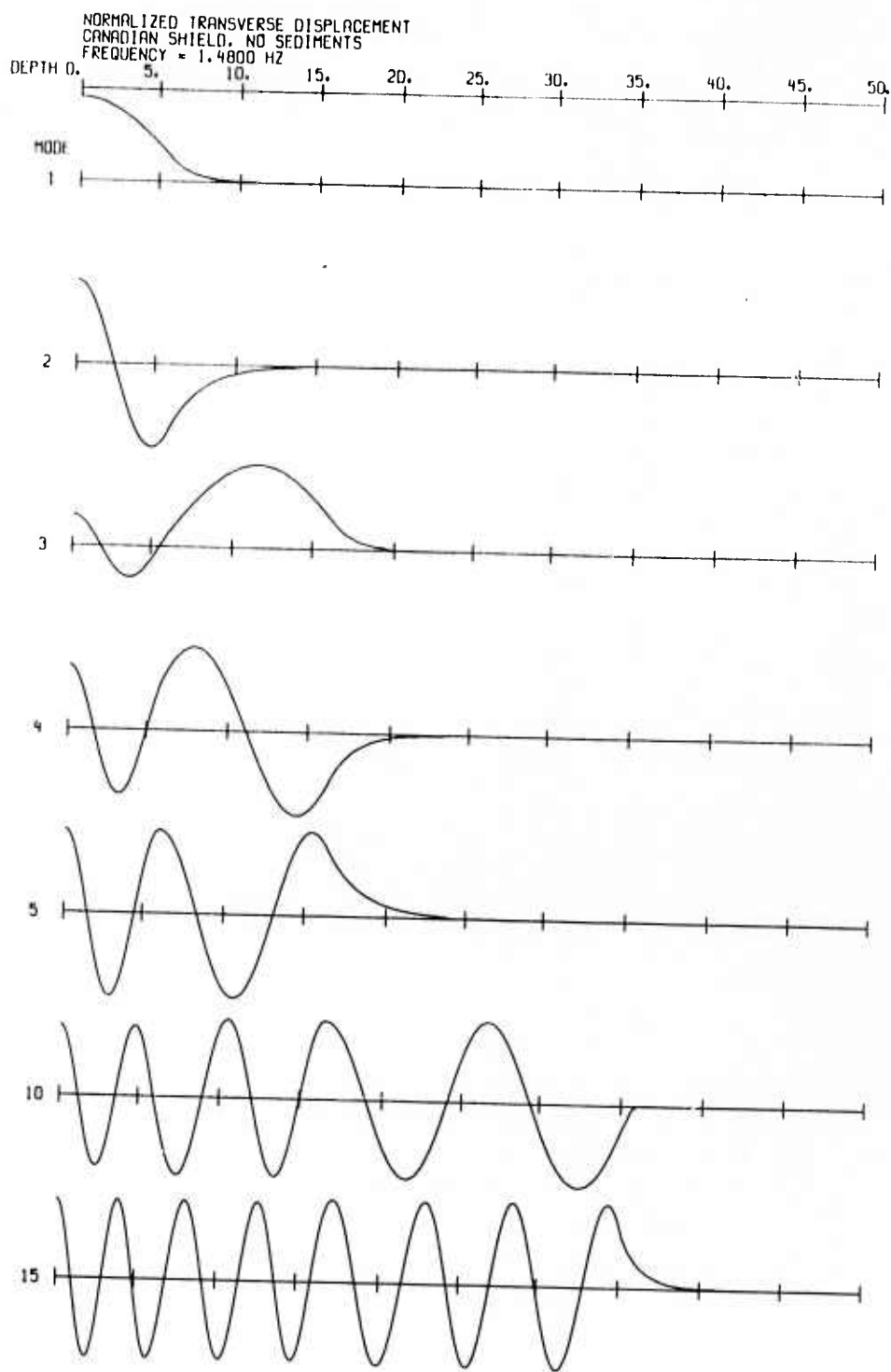


Figure 14b. $f = 1.48$ Hz
Particle displacement eigenfunction versus depth
for selected Love-wave modes of the Canadian
shield model with no sediments.

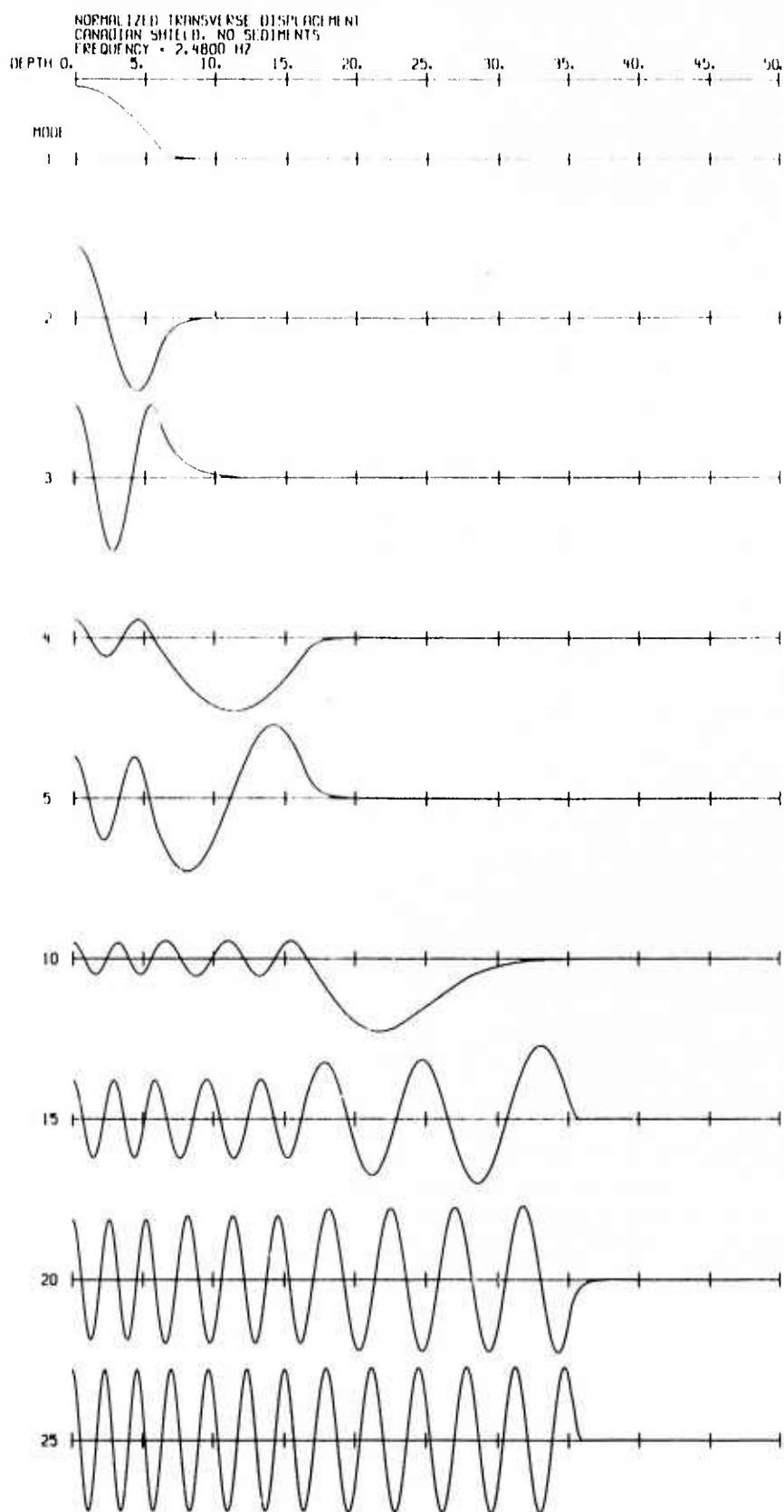


Figure 14c. $f = 2.48$ Hz
Particle displacement eigenfunction versus depth
for selected Love-wave modes of the Canadian
shield model with no sediments.

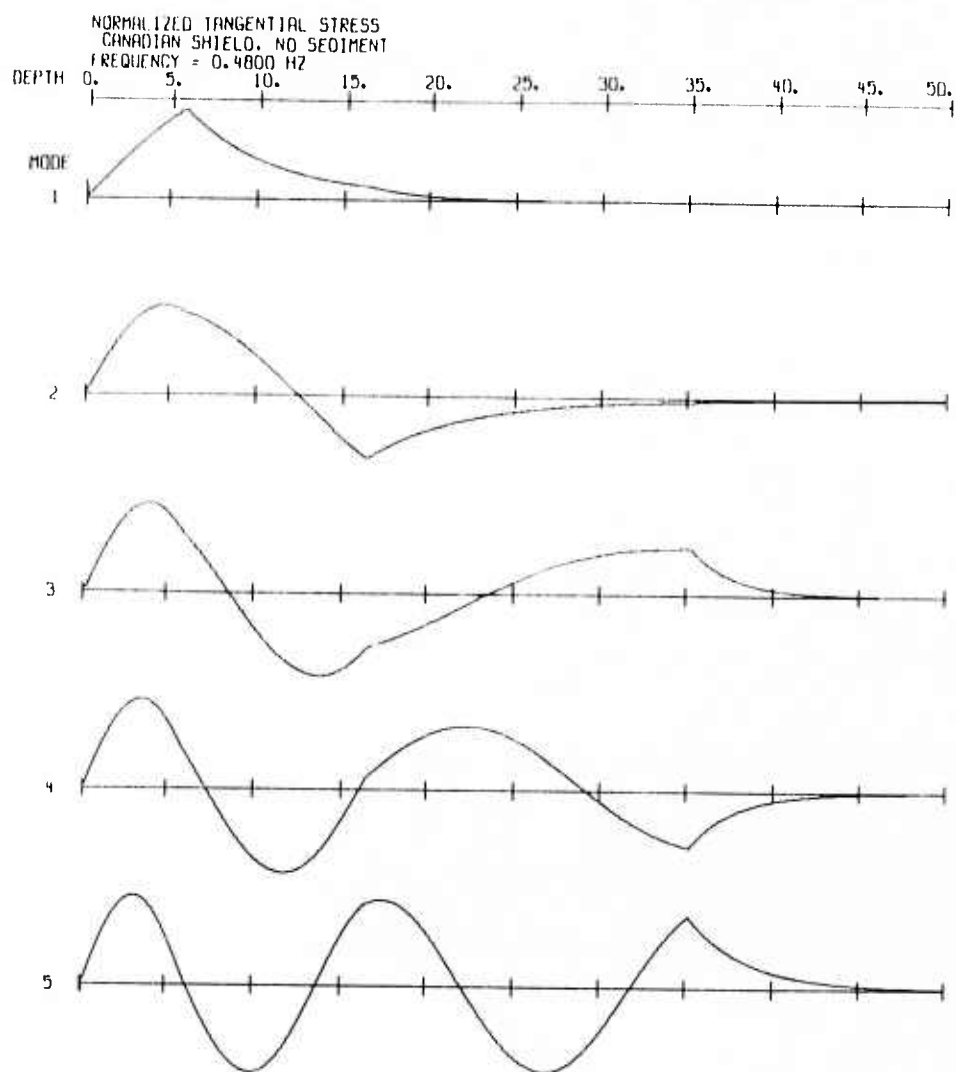


Figure 15a. $f = 0.48$ Hz
Stress eigenfunction versus depth for selected
Love-wave modes of the Canadian shield model
with no sediments.

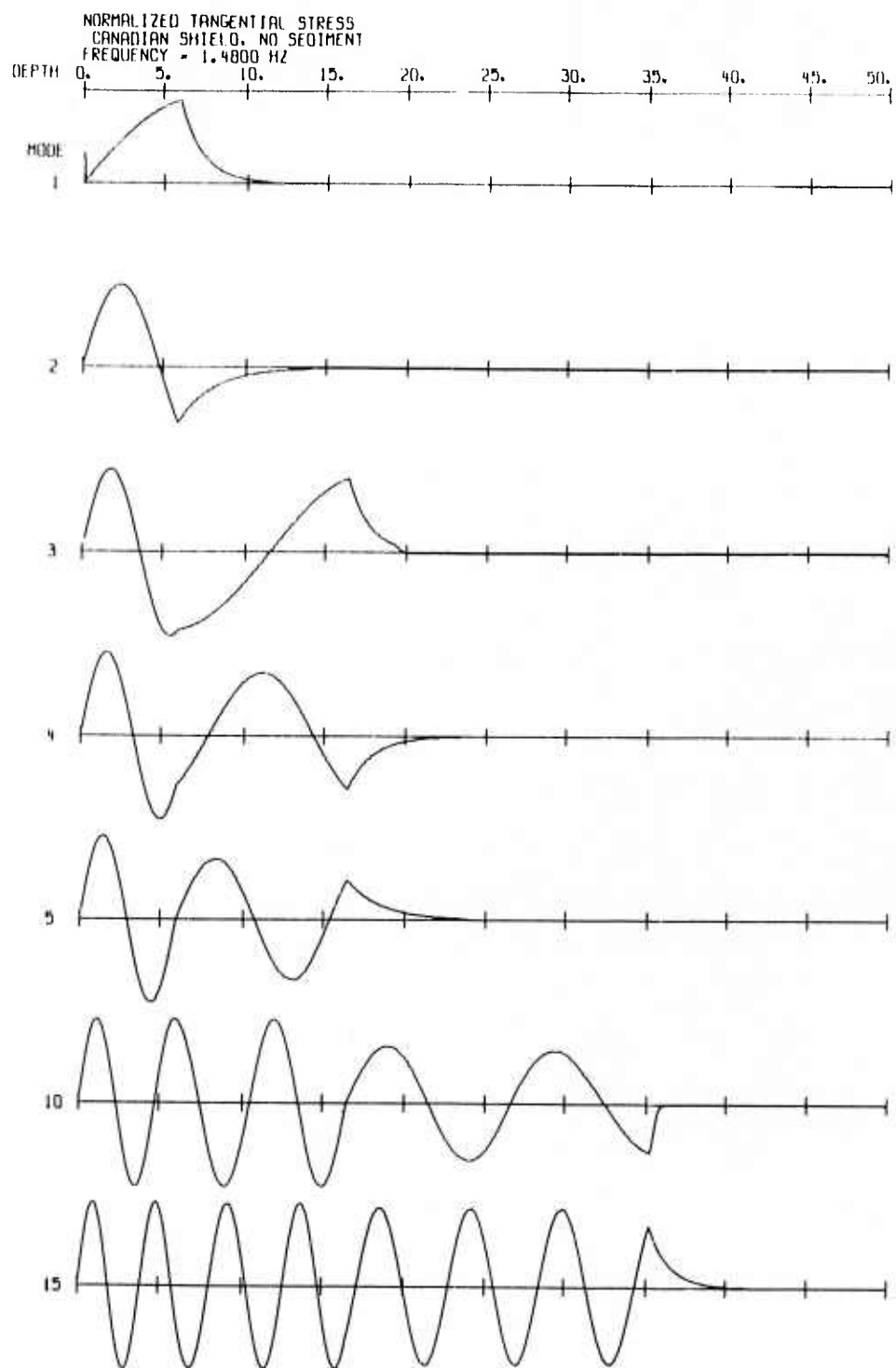


Figure 15b. $f = 1.48$ Hz
Stress eigenfunction versus depth for selected
Love-wave modes of the Canadian shield model
with no sediments.

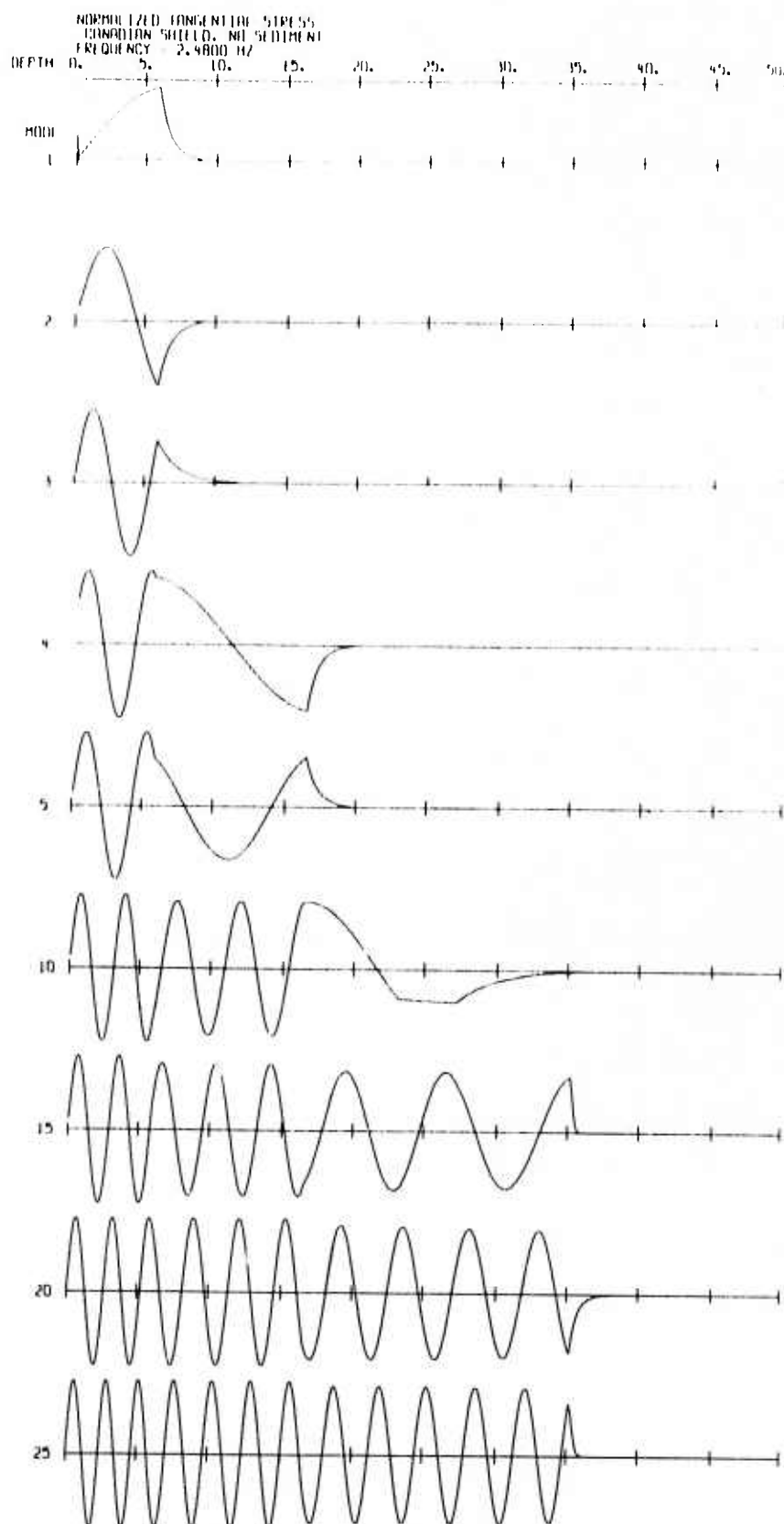


Figure 15c. $f = 2.48 \text{ Hz}$
Stress eigenfunction versus depth for selected
Love-wave modes of the Canadian shield model
with no sediments.

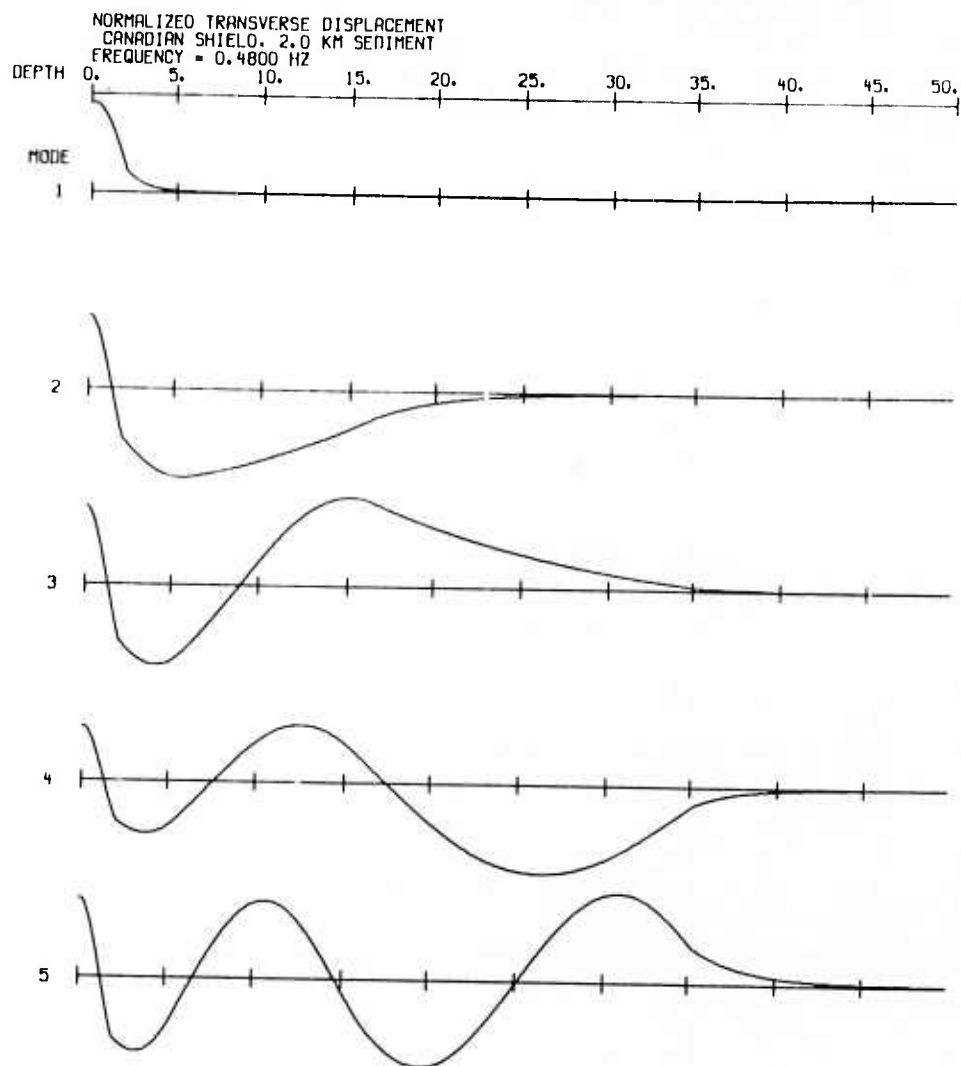


Figure 16a. $f = 0.48$ Hz
Particle displacement eigenfunction versus
depth for selected Love-wave modes of the
Canadian shield model with 2 km of sediments.

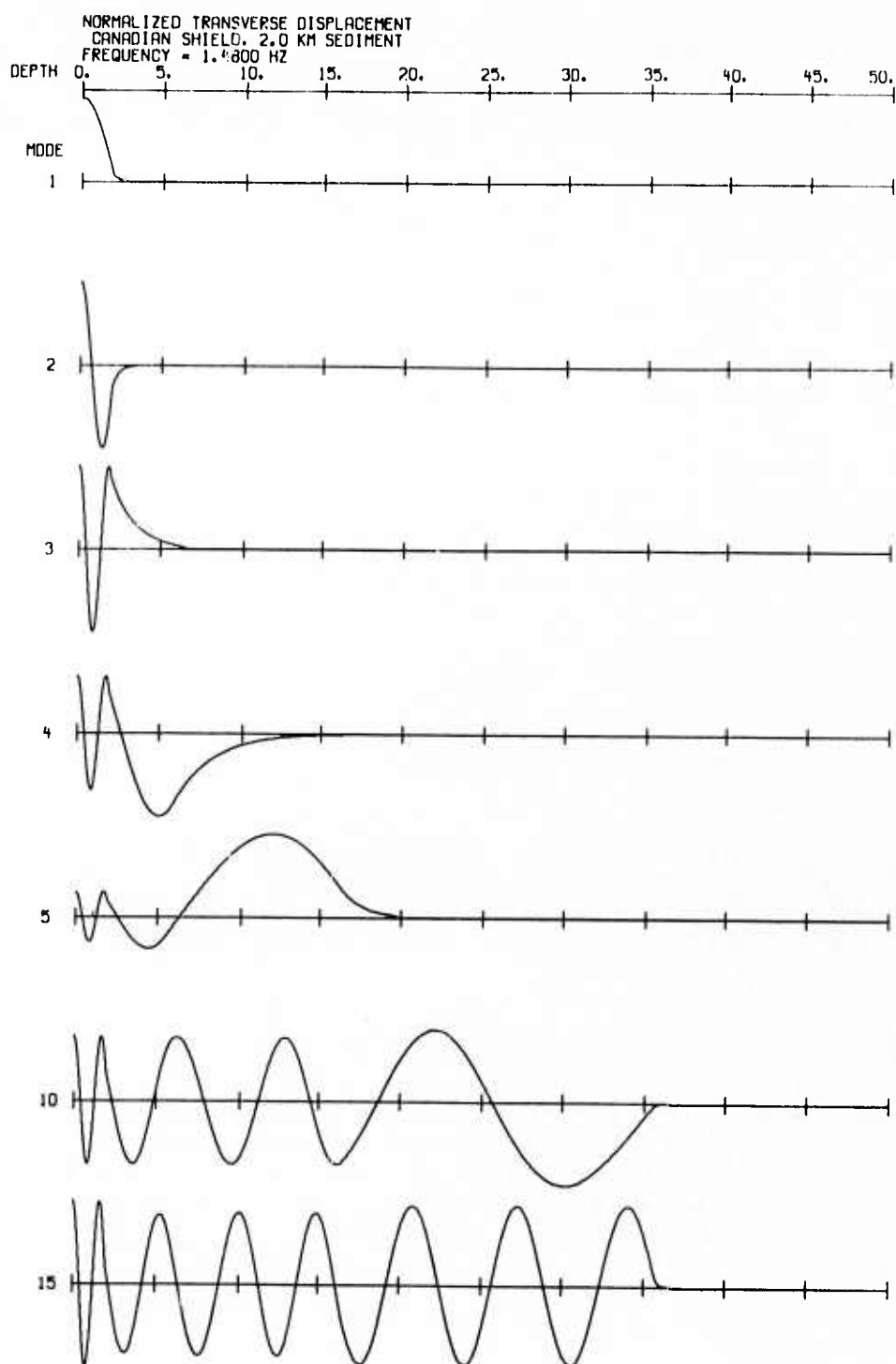


Figure 16b. $f = 1.48 \text{ Hz}$
Particle displacement eigenfunction versus
depth for selected Love-wave modes of the
Canadian shield model with 2 km of sediments.

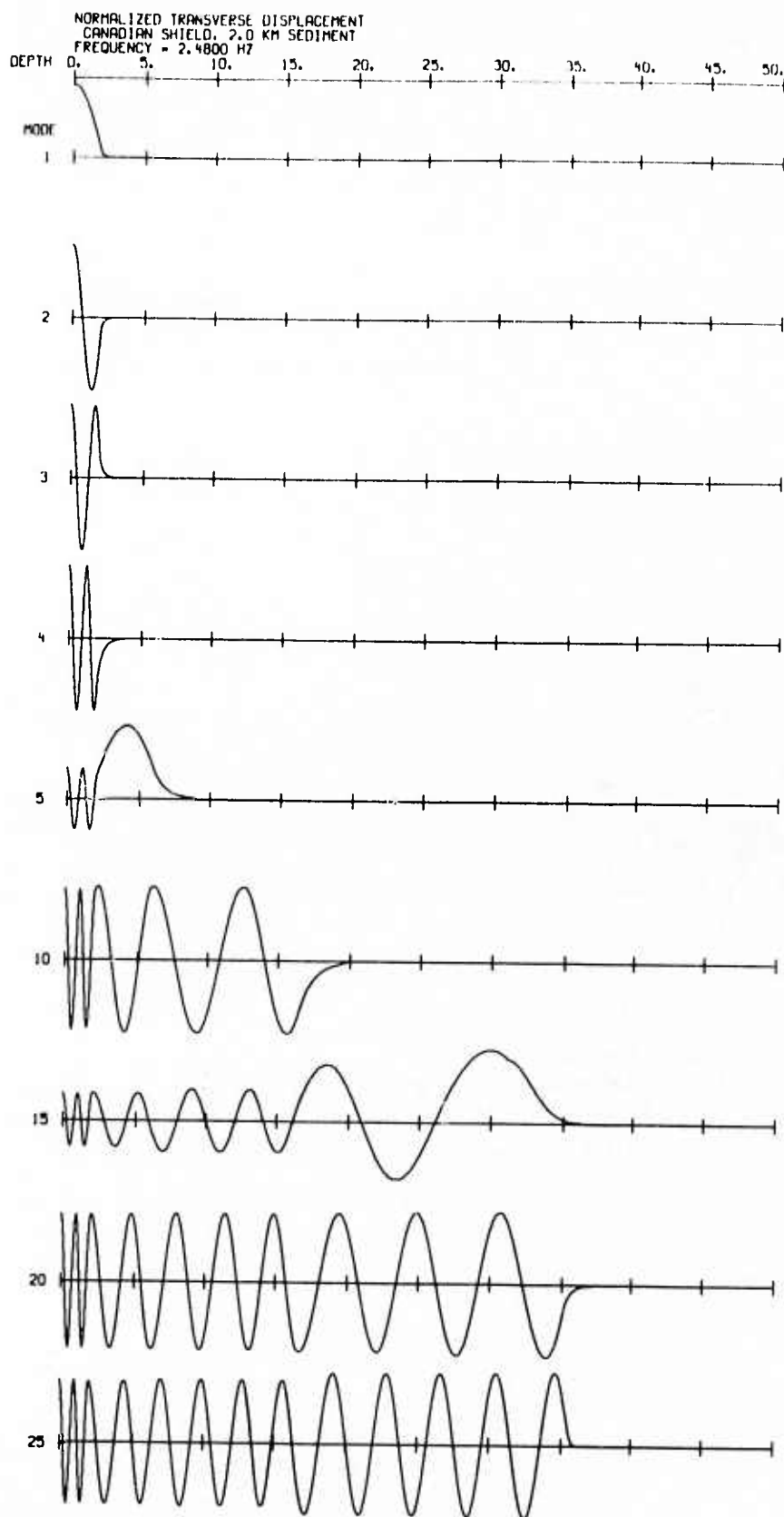


Figure 16c. $f = 2.48$ Hz
Particle displacement eigenfunction versus
depth for selected Love-wave modes of the
Canadian shield model with 2 km of sediments.

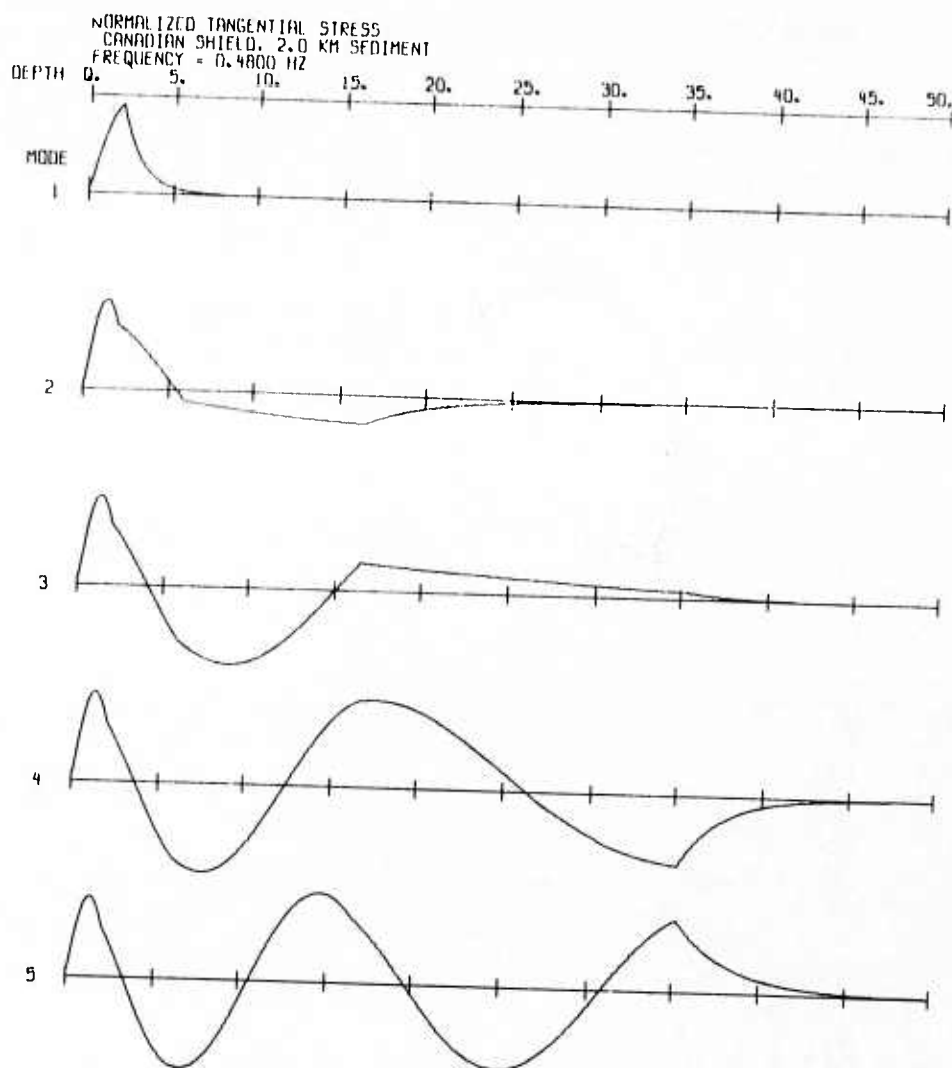


Figure 17a. $f = 0.48$ Hz
Stress eigenfunction versus depth for the
selected Love-wave modes of the Canadian
shield model with 2 km of sediments.

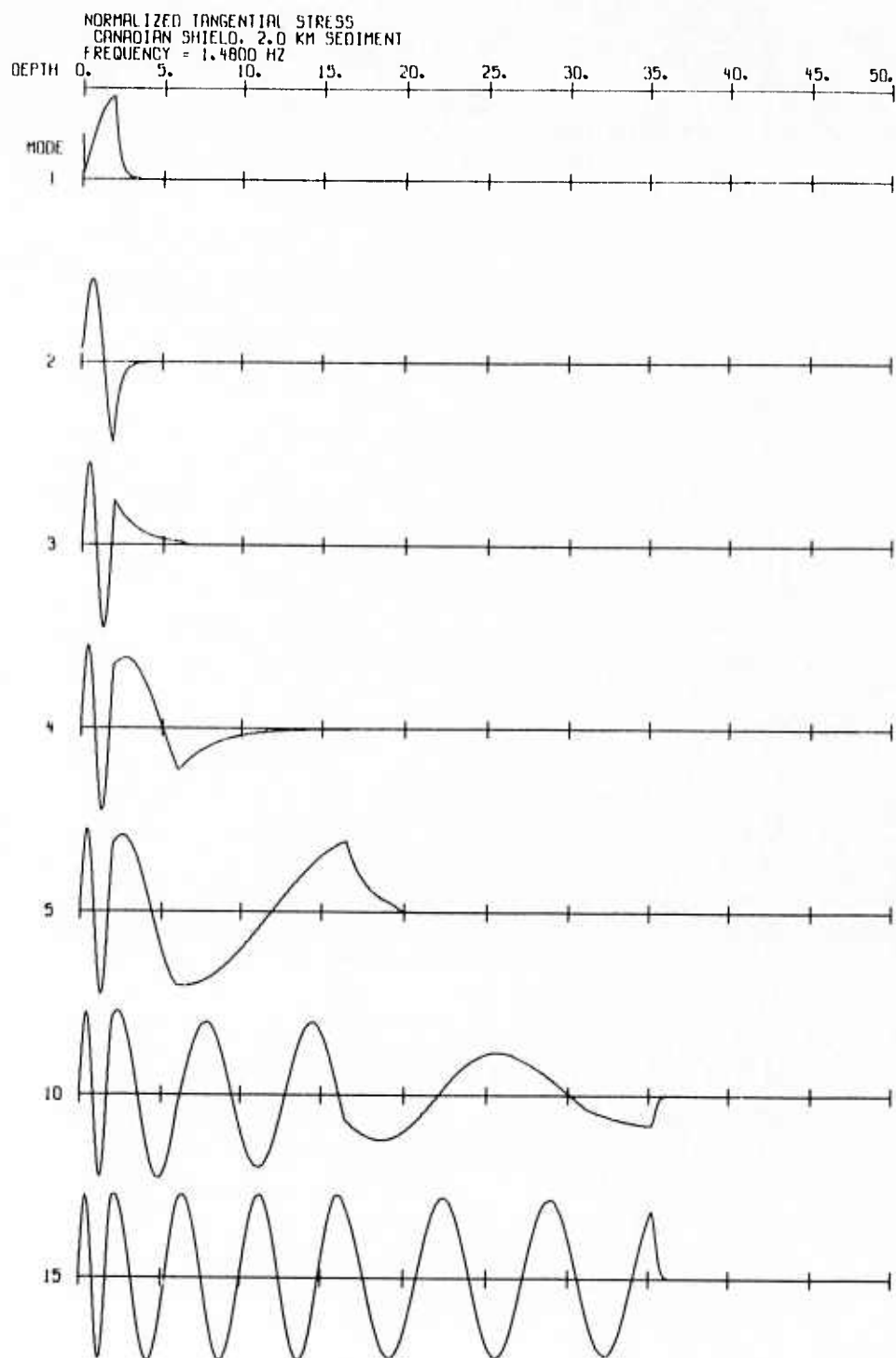


Figure 17b. $f = 1.48 \text{ Hz}$
Stress eigenfunction versus depth for the
selected Love-wave modes of the Canadian
shield model with 2 km of sediments.

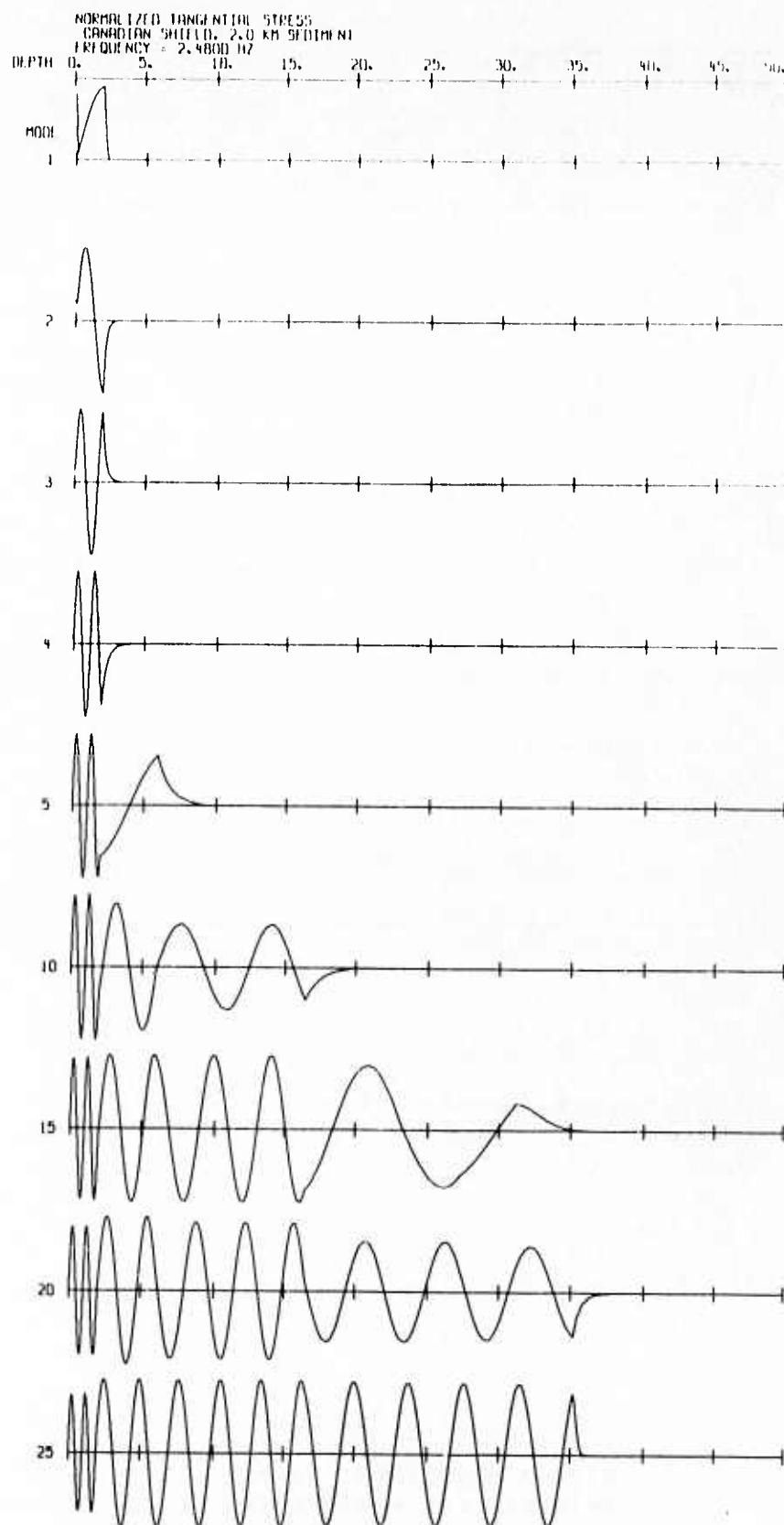


Figure 17c. $f = 2.48$ Hz
Stress eigenfunction versus depth for the
selected Love-wave modes of the Canadian
shield model with 2 km of sediments.

at high frequencies. These figures also show that, as the frequency increases, the maxima and nulls of the higher-order modes move into the near-surface layers. In the soft-rock model, when the particle displacement eigenfunction has a concentration of energy in the sedimentary layer, most of the energy in that mode is attenuated, giving rise to the minima in the graphs of Q_L in Figure 13. Similarly, if the energy is concentrated in the underlying shield, Q_L has a maximum. This is well illustrated by the behavior of mode 5 at 0.48 and 1.48 Hz.

Although this report is intended to investigate the effect of crustal structure on the propagation of L_g in shields, we now digress briefly in order to compare the results of our computations with those which would result from using a very different earth model, namely that of the Basin-Range province in the southwestern United States. The shear-wave velocity profile for this earth model, which we take from Keller et al. (1976), is shown in Figure 18. An important difference between this model and our shield model is the presence of a crustal LVZ. As we have suggested in our previous discussions, the LVZ causes the phase velocity dispersion curves in Figure 19 to osculate at the shear-wave velocity of that layer. The high-velocity "lid" traps energy in the LVZ, with the osculating modes in Figure 19 forming a continuous link and creating a nondispersive wave in that layer. This linkage of modes is also illustrated in Figure 20, which shows that the transfer function for mode 3, for example, decreases by more than six orders of magnitude at 0.8 Hz, where the transfer function for mode 2 increases, and then it increases again at 1.6 Hz, where the transfer function for mode 4 plummets. This trade-off causes these curves to link up, yielding a relatively flat graph for $A_L(f)$ for the channel wave. Although we cannot make any quantitative estimates without actually computing the synthetic seismograms for the Basin-Range model, we conclude that this trapping of energy in the crustal LVZ may be one of the principal differences between L_g propagation in shield regions and in the southwestern United States. The presence of the LVZ correlates with high heat flow and is probably indicative of partial melting, so we anticipate that the energy in this layer will be dissipated by attenuation, perhaps resulting in a stronger L_g attenuation than in

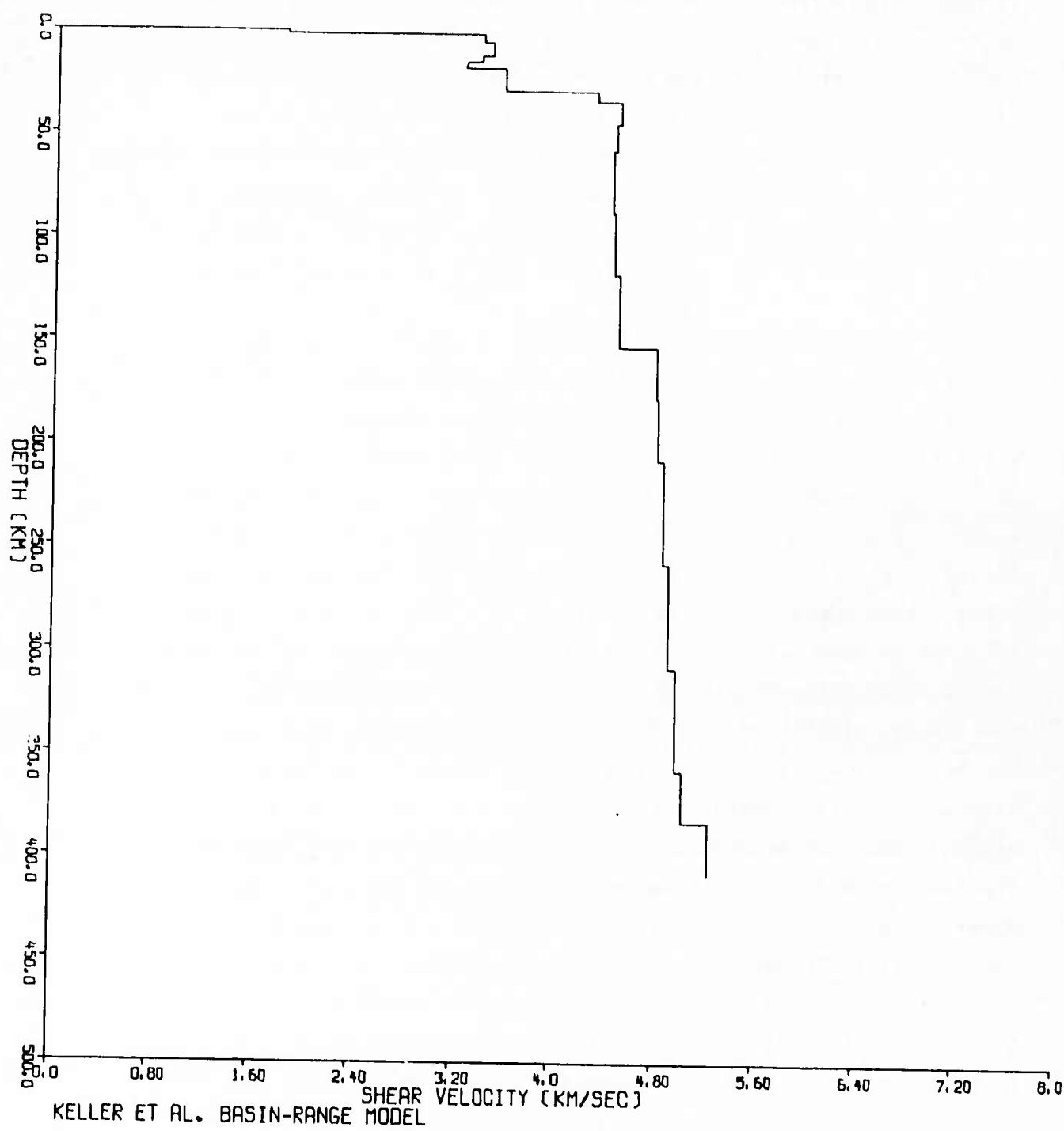


Figure 18. Shear wave velocity versus depth for the Basin-Range model.

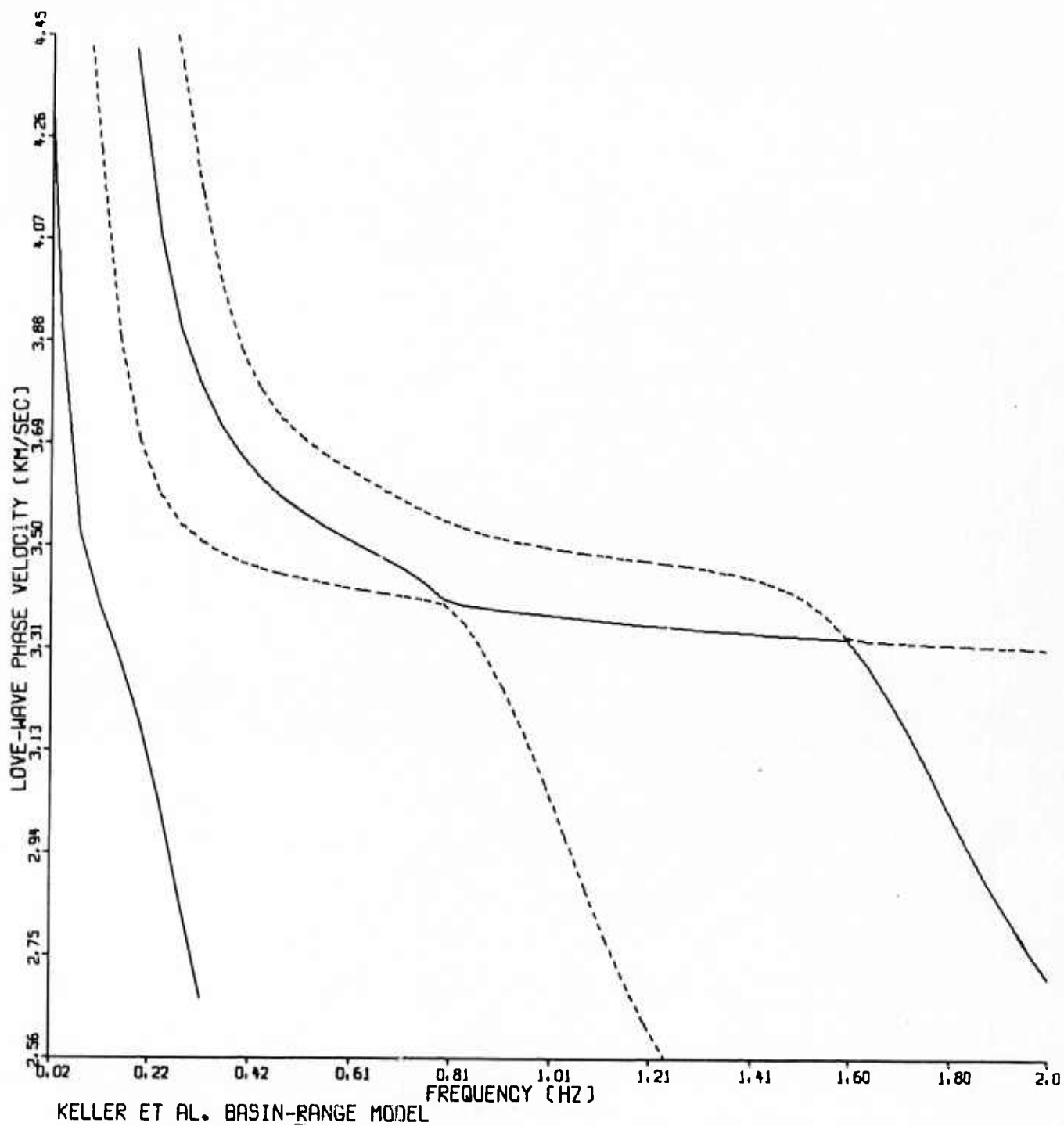


Figure 19. Phase velocity versus frequency for four Love-wave modes of the Basin-Range model.

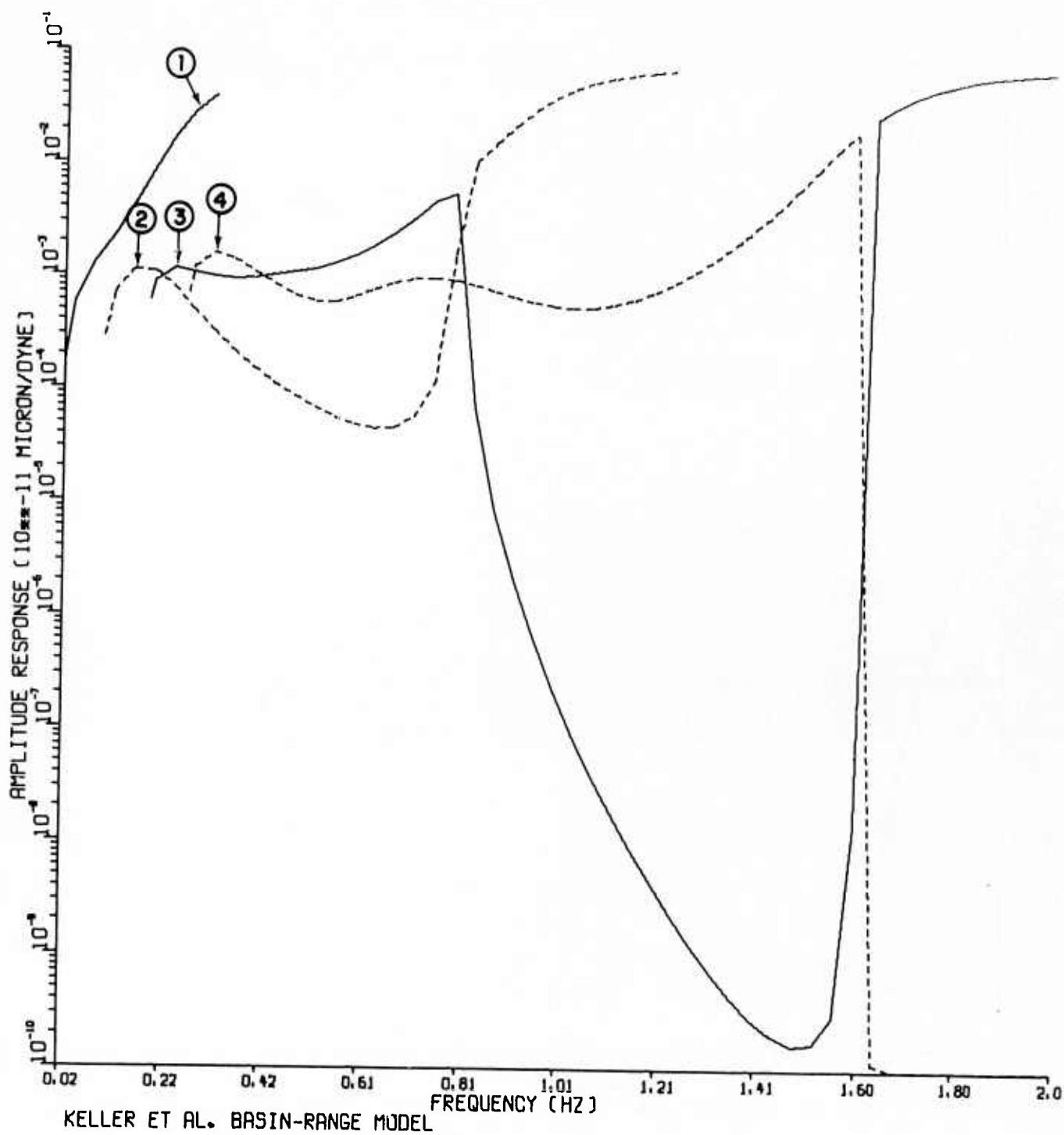


Figure 20. Layered medium amplitude response for four Love-wave modes of the Basin-Range model. The fundamental mode is labelled mode 1, with modes 2-4 as the first three higher order modes.

shield structures. Schwab and Knopoff (1971) appealed to similar reasoning in order to explain the failure of L_g (at longer periods, which sense the upper mantle structure) to propagate through oceanic paths. Although we have considered only Love-wave modes, we note that the high-velocity lid and the LVZ will also trap energy which propagates as Rayleigh-wave modes, and so P-SV-type head waves will be guided along the interfaces. These phenomena may contribute to the amplitude of crustal phases such as P_g which are more prominent in the southwestern United States than in shield regions; there may in fact be a sort of trade-off whereby the crustal structure is responsible for partitioning energy between P_g and L_g . We suggest that in a future study both Love-wave and Rayleigh-wave synthetic seismograms be generated for the Basin-Range model in order to investigate the generation and propagation of regional phases in a tectonically active province. In particular, the relationship between P_g and L_g needs to be understood if these two phases are to be used as seismic discriminants.

Returning now to our Canadian shield models, we shall generate synthetic seismograms using the methodology which we have described previously. We shall use these synthetics to investigate:

- 1) the frequency- and modal-dependence of L_g for various source mechanisms and focal depths;
- 2) the decay of L_g with distance for propagation in the hard-rock and soft-rock models;
- 3) the phase-velocity structure of L_g ; and
- 4) differences between synthetic and observed L_g seismograms.

RESULTS

Hard Rock Model

We examine first the results of applying the previously described process of seismogram synthesis to the "hard-rock" Canadian shield model illustrated in Figures 1-6. Figure 21 shows the contribution of selected modes to the transverse seismogram which would be recorded on an LRSM short-period instrument at a distance of 500 km from a 0.5-km deep strike-slip earthquake. The figure illustrates each of the first five modes, the superposition of these five modes, the tenth mode, the superposition of the first ten modes, the fifteenth mode, etc., and finally, the superposition of all 26 modes. We see that, as we had anticipated, for this shallow source almost all of the energy is transmitted in the lowest-order modes. The first two modes show very strong pulses where energy distributed throughout broad ranges of frequencies arrives almost simultaneously. These spikes in the L_g envelope correspond to the flat parts of the group velocity dispersion curves (cf. Figure 5), 3.46 km/sec for mode 1 and 3.42 km/sec for mode 2. Although a group-velocity gate was imposed on the synthetic seismogram in order to prevent "wrap-around", some numerical error appears to be responsible for the late-arriving ($U \leq 3.29$ km/sec) energy, since no such arrivals are predicted in Figure 5. The principle source of the computational error is aliasing, which becomes problematic at frequencies higher than about $f \geq 2.2$ Hz. Because the LRSM instrument response attains its maximum value at $f = 2.7$ Hz, there is substantial energy in the wavetrain at frequencies only slightly less than the 2.5-Hz Nyquist frequency, and the stroboscopic effect introduced by the sparse sampling of this energy produces "beats" which can be seen as regularly spaced low-amplitude peaks in the otherwise featureless portions of the seismogram both before and after the passage of the large wavepacket containing the true signal. This numerical problem can be eliminated by suppressing the high-frequency portion of the spectrum by means of an anti-aliasing filter or by increasing the sampling rate (in which case more modes would be required to extend the synthesis to the new Nyquist frequency).

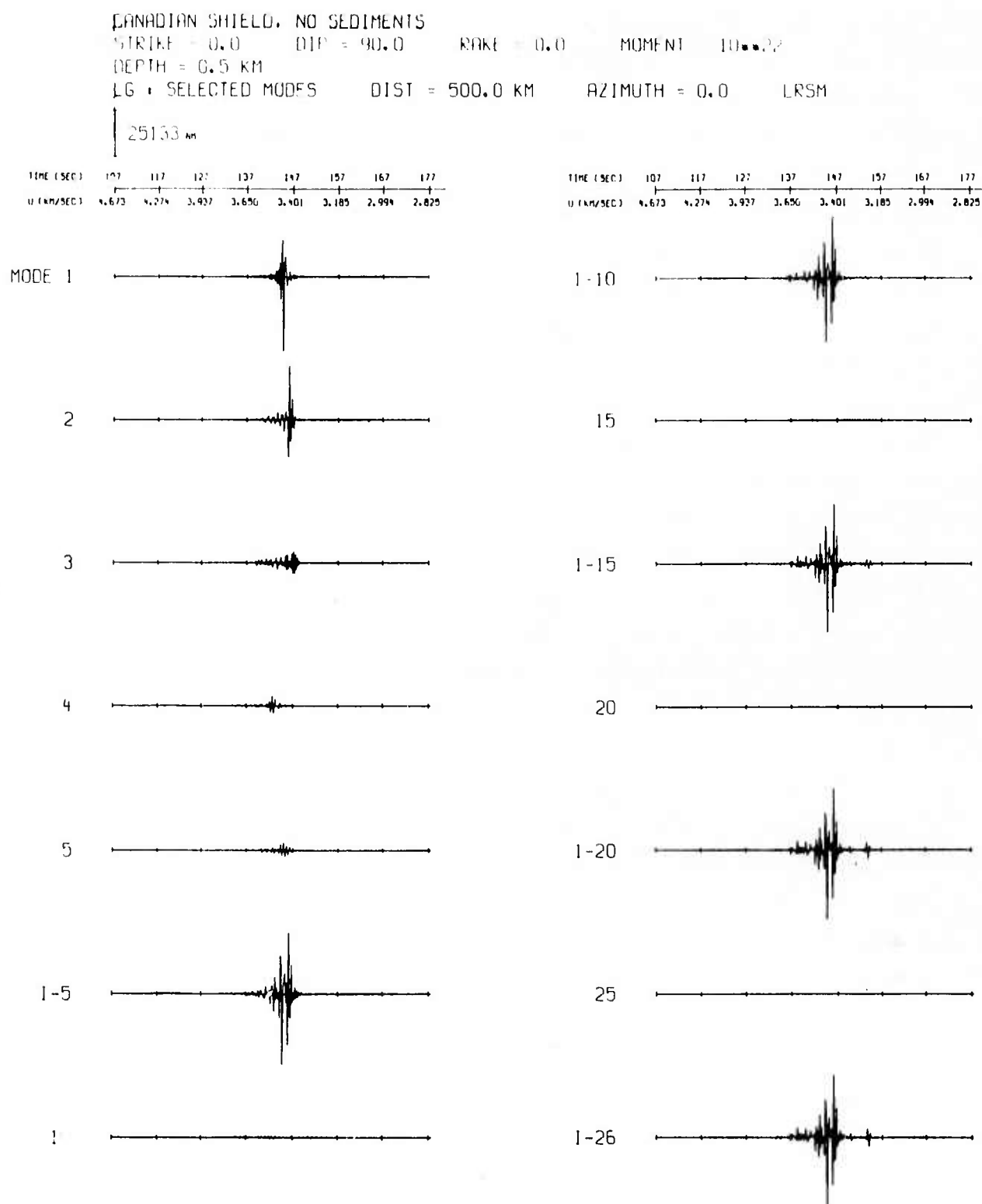


Figure 21. Synthetic seismogram for a strike-slip source 0.5 km deep in the hard-rock model.

The behavior of the higher modes can be seen better by moving the source to greater depth, as is done in Figure 22. We see that the influence of the first two modes is much smaller for this 10-km deep source and that the $U = 3.46$ km/sec pulse is in fact all that can be seen of the fundamental mode when all the modes are plotted on the same scale. The second mode is seen to increase in amplitude as the frequency of the dispersed wavetrain increases to about $F = 1$ Hz, and then it remains approximately constant, in accordance with the behavior of $A_L(f)$ for this mode, which is shown as the left-most dashed curve in Figure 6. The dispersed wavetrain for this mode terminates abruptly when all the high frequencies arrive simultaneously at $U = 3.42$ km/sec. The fourth and all higher modes exhibit reverse dispersion, with the lowest frequencies arriving last; again, this follows from Figure 5. Note that group velocities of the maximum amplitudes of the higher modes are less than those of the lower-order modes; this is the reverse of the situation for the phase velocities, which are faster for the (deeper-penetrating) higher-order modes (cf. Figure 4). Moving the source still further down to a focal depth of 20 km (Figure 23) results in the complete vanishing of the fundamental mode and in the significant propagation of energy by even the highest-order modes. Comparing the traces for mode 5 in Figures 22 and 23, we see that the frequency content of this mode is lower for the deeper source. The low-pass filtering effect is brought about by the near vanishing of the stress and displacement eigenfunctions for mode 5 at 20 km depth for frequencies greater than 1 Hz, and the existence of these eigenfunctions at frequencies less than 1 Hz, as is shown in Figure 14a-c and 15a-c. The sum of all 26 modes is marked by sharp spikes, as are, to some extent, almost all of the synthetic L_g seismograms which we have generated. We note that the envelopes of observed L_g phases are expected to be smoother than those of the synthetics on account of scattering, which broadens out the sharp pulse-like arrivals. In Figures 21-23 we have considered only the simple case of strike-slip motion on a vertical fault. The shape of the L_g envelope will of course change as the focal mechanism is varied (while the depth is held constant), as is shown in Figure 24. Note that the wavetrain of these seismograms is more dispersed, since the source-to-receiver separation is now taken to be 1000 km.

CANADIAN SHIELD, NO SEDIMENTS

STRIKE = 0.0 DIP = 90.0 RAKE = 0.0 MOMENT = 10^{22}

DEPTH = 10.0 km

LG : SELECTED MODES DIST = 500.0 km AZIMUTH = 0.0 LRSM

6733 km

TIME (SEC)	107	117	127	137	147	157	167	177
U (KM/SEC)	4.673	4.274	3.937	3.650	3.401	3.185	2.994	2.825

TIME (SEC)	107	117	127	137	147	157	167	177	187
U (KM/SEC)	4.673	4.274	3.937	3.650	3.401	3.185	2.994	2.825	2.674

MODE 1

1-10

2

15

3

1-15

4

20

5

1-20

1-5

25

10

1-26

Figure 22. Synthetic seismogram for a strike-slip source. 10 km deep in the hard-rock model.

CANADIAN SHIELD, NO SEDIMENTS

STRIKE = 0.0 DIP = 90.0 RAKE = 0.0 MOMENT = 10^{22}

DEPTH = 20.0 KM

LG = SELECTED MODES DIST = 500.0 KM AZIMUTH = 0.0 LRSM

3058 km

TIME (SEC)	107	117	127	137	147	157	167	177	187
U (KM/SEC)	4.673	4.274	3.937	3.650	3.401	3.185	2.994	2.825	2.674

TIME (SEC)	107	117	127	137	147	157	167	177	187
U (KM/SEC)	4.673	4.274	3.937	3.650	3.401	3.185	2.994	2.825	2.674

MODE 1



1-10




2



15



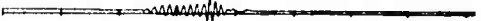
3



1-15



4



20



5



1-20



1-5



25



10



1-26



Figure 23. Synthetic seismogram for a strike-slip source 20 km deep in the hard-rock model.

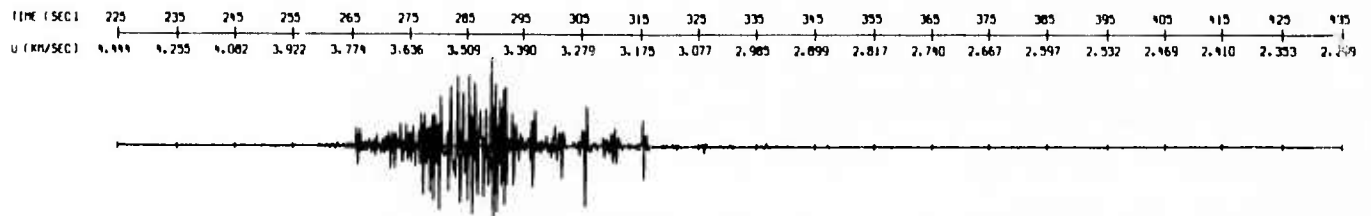
CANADIAN SHIELD. NO SEDIMENTS

STRIKE = 0.0 DIP = 90.0 RAKE = 45.0 MOMENT = 10^{22}

DEPTH = 10.0 KM

LG = SUM OF 26 MODES DIST = 1000.0 KM AZIMUTH = 0.0 LRSM

1105 μm



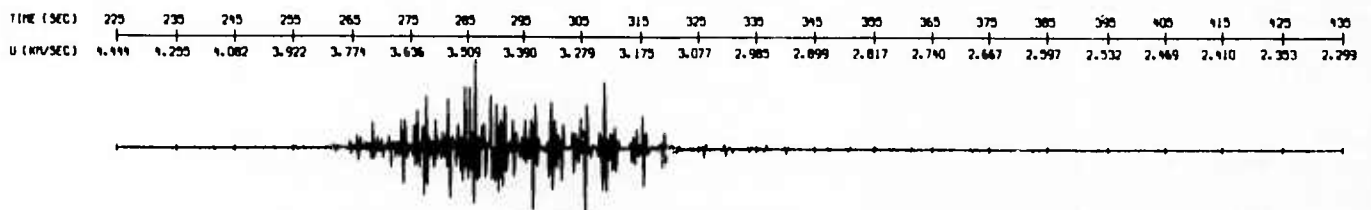
CANADIAN SHIELD. NO SEDIMENTS

STRIKE = 0.0 DIP = 90.0 RAKE = 90.0 MOMENT = 10^{22}

DEPTH = 10.0 KM

LG = SUM OF 26 MODES DIST = 1000.0 KM AZIMUTH = 0.0 LRSM

547 μm



CANADIAN SHIELD. NO SEDIMENTS

STRIKE = 0.0 DIP = 60.0 RAKE = 0.0 MOMENT = 10^{22}

DEPTH = 10.0 KM

LG = SUM OF 26 MODES DIST = 1000.0 KM AZIMUTH = 0.0 LRSM

1527 μm

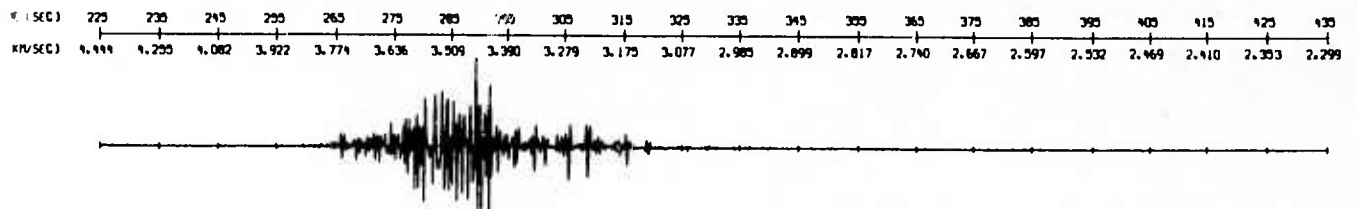


Figure 24. Synthetic seismogram for different focal mechanisms at a depth of 10 km in the hard-rock model.

The decrease in the maximum amplitude of the L_g envelope with increasing focal depth is illustrated in Figure 25 for 3 different combinations of focal mechanism and receiver distance, all for the same value of the seismic moment. It is shown that, for the most part, the deeper sources have a smaller L_g amplitude, and that the sharpest decrease in amplitude occurs at depths between 5 and 10 km. We should note that, as Figures 21-24 indicate, the visual smoothing of the synthetic wavetrains to form envelopes around the wave packets is a rather subjective procedure, so the maximum amplitudes plotted in Figure 25 are subject to some uncertainty.

We now wish to measure the rate of decay of the maximum amplitude with increasing source-to-receiver separation. Nuttli (1973) assumed that the L_g maximum is an Airy phase, in which case its amplitude may be expressed as

$$A = K \Delta^{-1/3} (\sin \Delta)^{-1/2} \exp(-\gamma \Delta) \quad (2)$$

where K is related to the seismic moment of the event and to its efficiency of L_g excitation, Δ is the angular distance from the source to the receiver, and γ is a coefficient which we shall determine empirically. In Figures 26a-g we show the envelope maxima of synthetic seismograms generated using several different focal mechanisms and depths in the hard-rock model. In each case synthetics were generated at distances of 300, 600, 900, 1200, 1500, and 1800 km, and the best-fitting value of γ was found by the technique of least squares applied to equation (2). The amplitude decay which is computed using this value of γ and Nuttli's (1973) formula is plotted for the range $100 \text{ km} \leq \Delta \leq 2000 \text{ km}$ along with the measured amplitudes of the synthetic seismograms in Figures 26a-g. These plots show that in every case some value of γ can be found so that Nuttli's (1973) Airy-phase formula yields a close approximation to the measured values of the envelope maxima, even though these maxima were not necessarily measured at the same group velocity for each seismogram. It should be noted that the strong nonlinearity of these best-fitting curves (on a log-log scale) except over short distance ranges precludes describing the amplitude decay in terms of a simple $\Delta^{-\alpha}$ falloff, as is normally done for longer-period surface waves

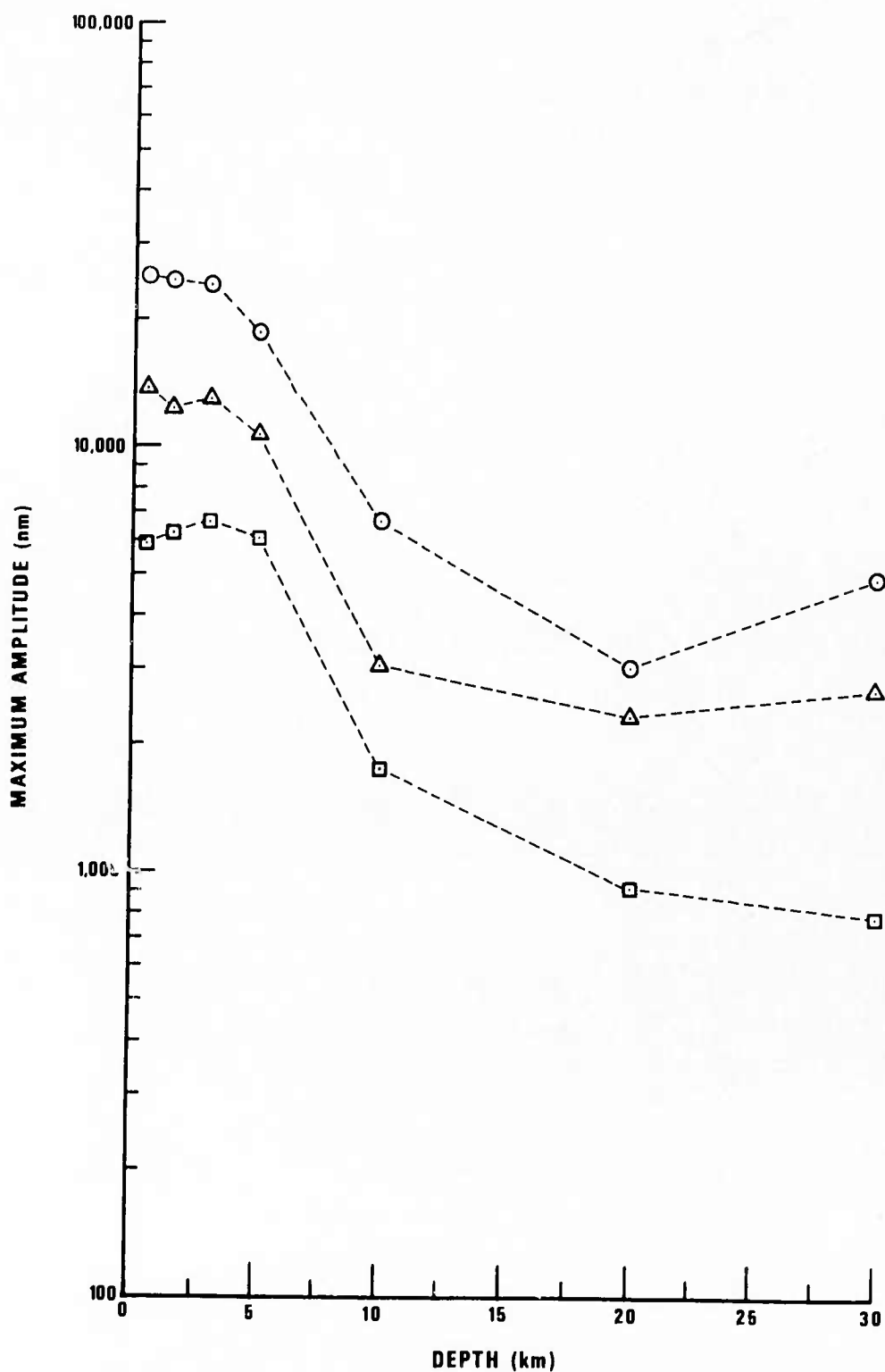


Figure 25. Amplitudes of envelope maxima of synthetic seismograms for source at various depths in the hard-rock model.
 Circles: rake = 0° , dip = 90° , strike = 0° , Δ = 500 km.
 Triangles: rake = 40° , dip = 70° , strike = 30° , Δ = 500 km.
 Squares: rake = 0° , dip = 90° , strike = 0° , Δ = 1000 km.

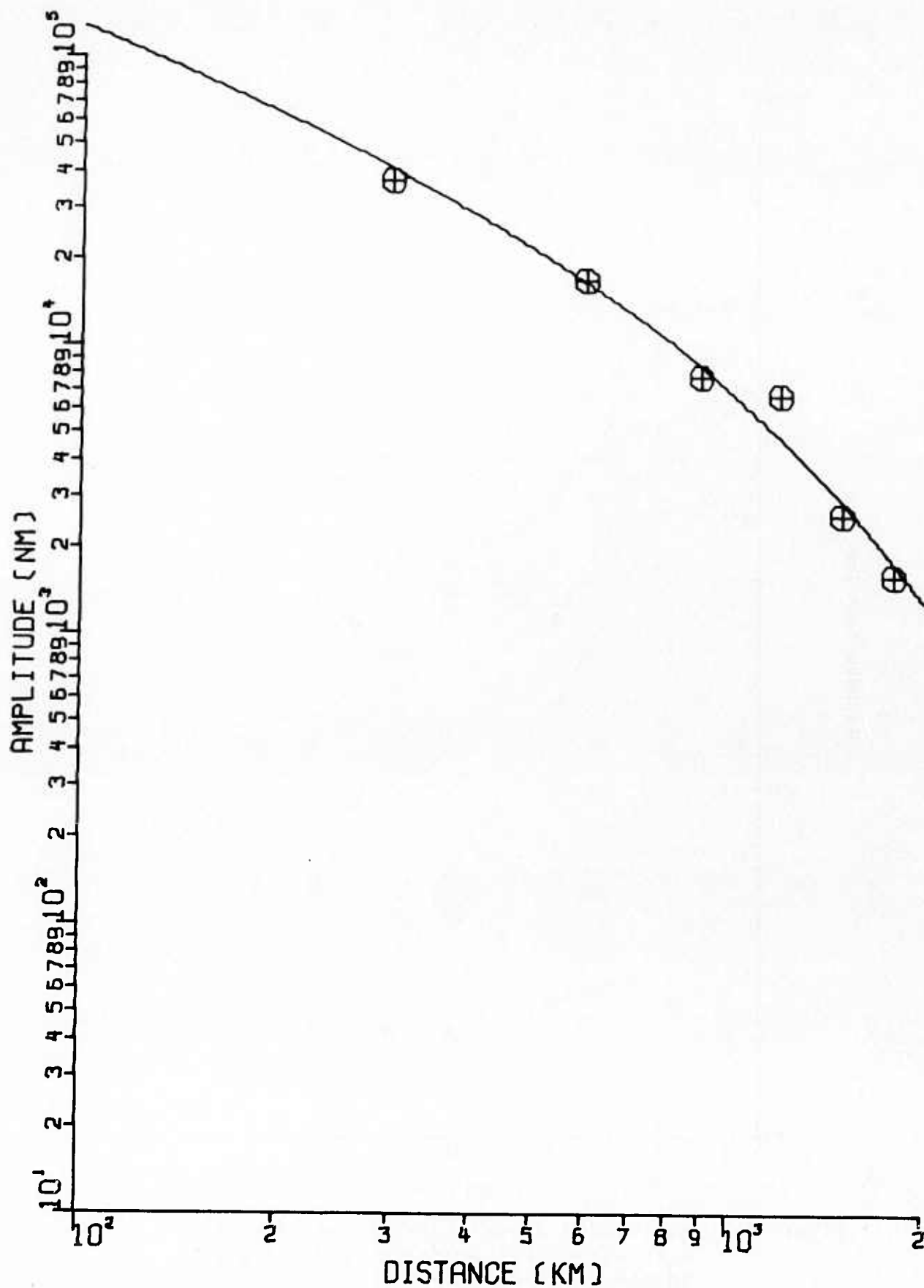


Figure 26a. depth = 0.5 km, rake = 0°, dip = 90°:
 $\gamma = 0.1229$ deg
 Amplitudes of envelope maxima of synthetic
 seismograms for the hard-rock model as
 observed at various distances.

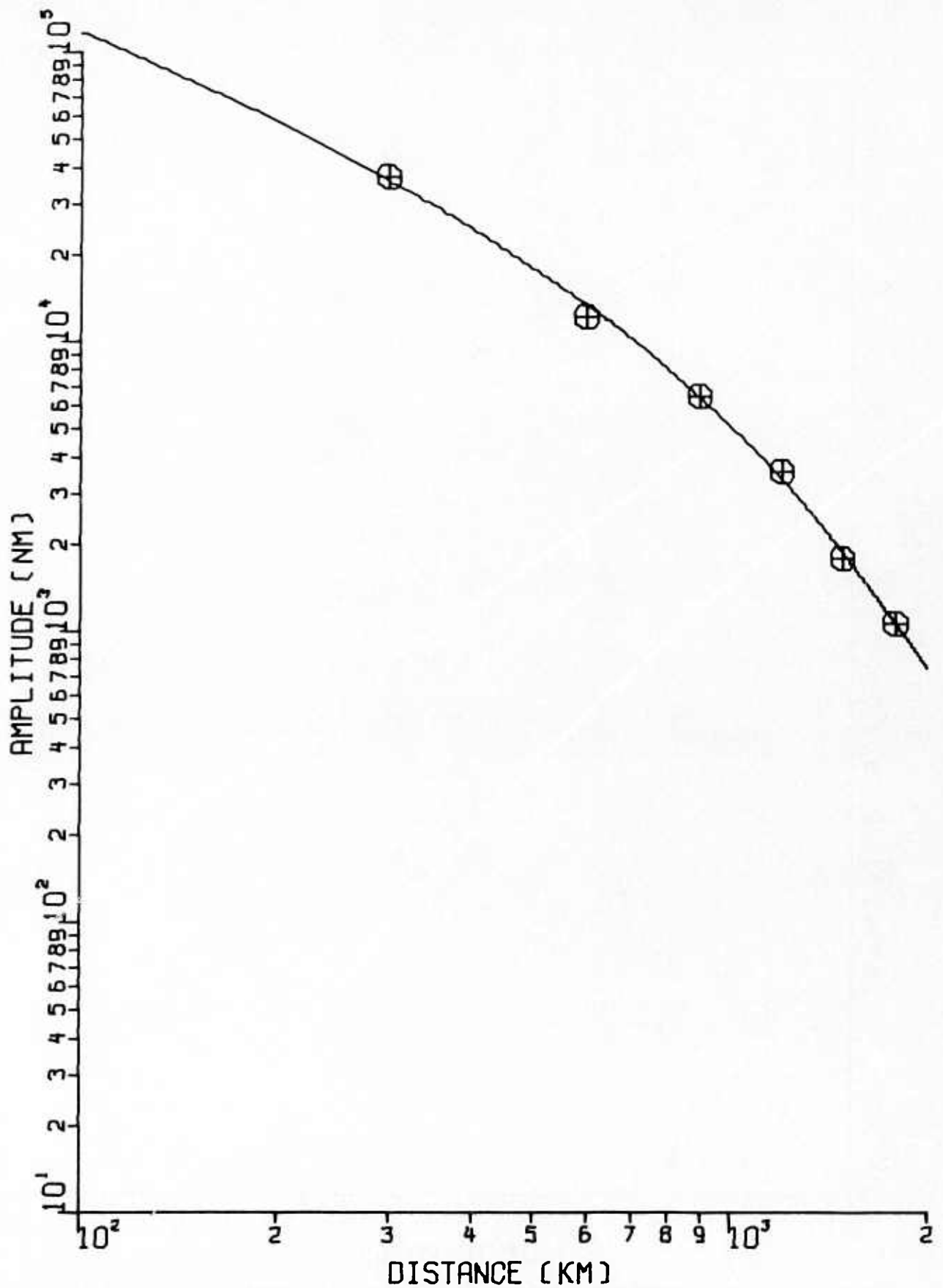


Figure 26b. depth = 5 km, rake = 0° , dip = 90° :
 $\gamma = 0.1505$ deg
 Amplitudes of envelope maxima of synthetic
 seismograms for the hard-rock model as
 observed at various distances.

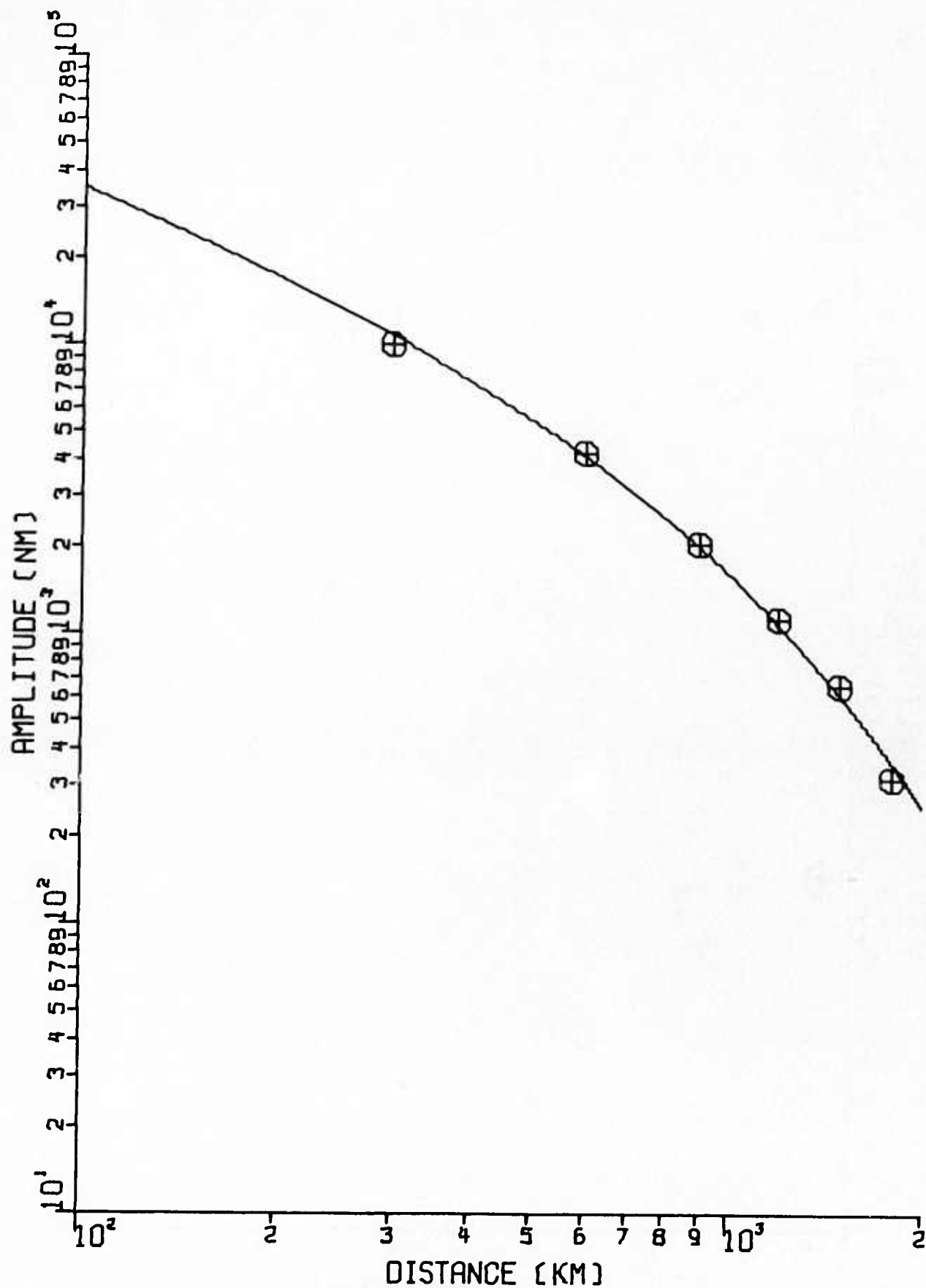


Figure 26c. depth = 10 km, rake = 0°, dip = 90°:
 $\gamma = 0.1421$ deg
 Amplitudes of envelope maxima of synthetic
 seismograms for the hard-rock model as
 observed at various distances.

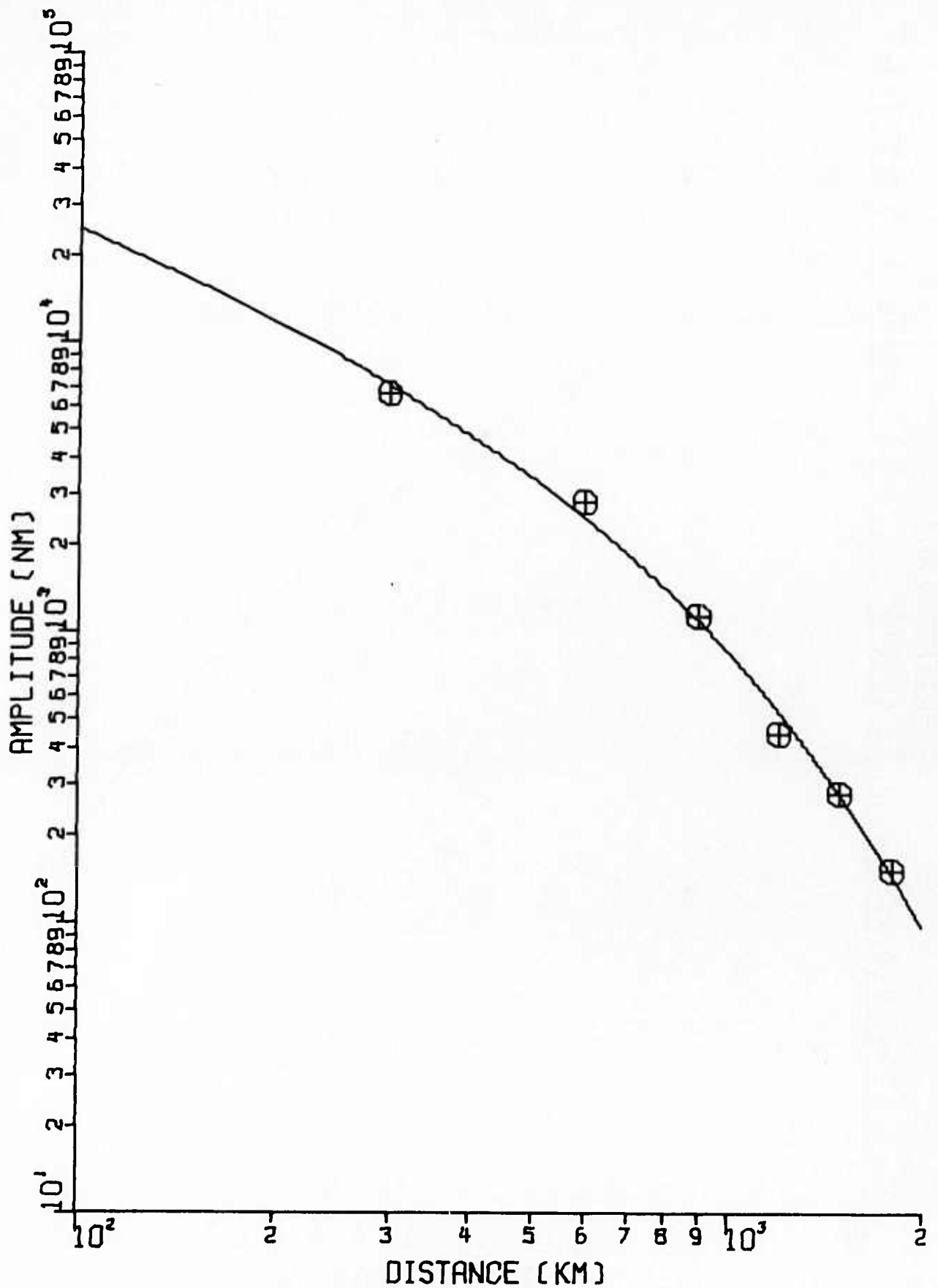


Figure 26d. depth = 20 km, rake = 0°, dip = 90°:
 $\gamma = 0.1785$ deg
 Amplitudes of envelope maxima of synthetic
 seismograms for the hard-rock model as
 observed at various distances.

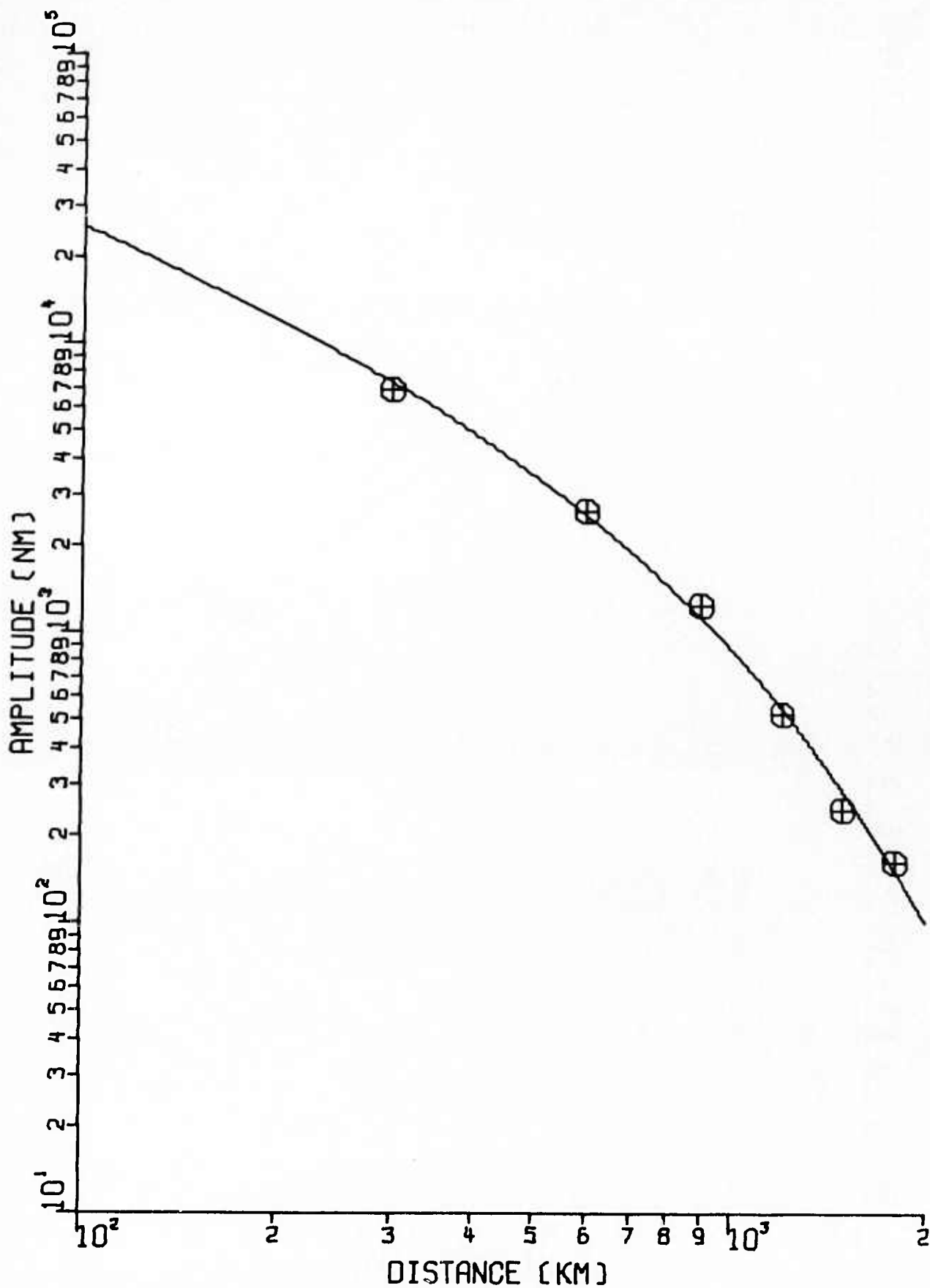


Figure 26e. depth = 30 km, rake = 0°, dip = 90°:
 $\gamma = 0.1778$ deg
 Amplitudes of envelope maxima of synthetic
 seismograms for the hard-rock model as
 observed at various distances.

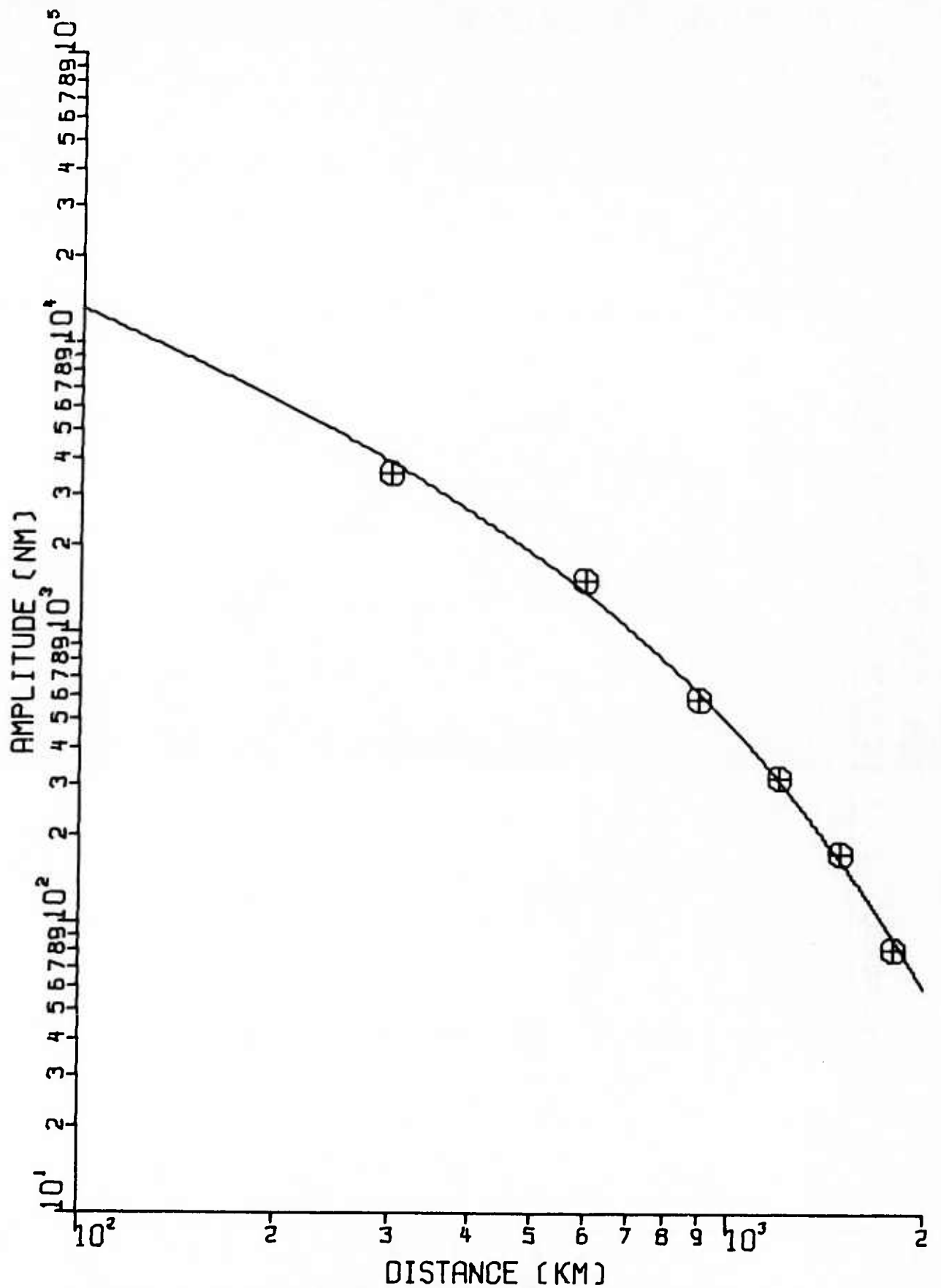


Figure 26f. depth = 10 km, rake = 90°, dip = 90°:
 $\gamma = 0.1698 \text{ deg l}$
 Amplitudes of envelope maxima of synthetic
 seismograms for the hard-rock model as
 observed at various distances.

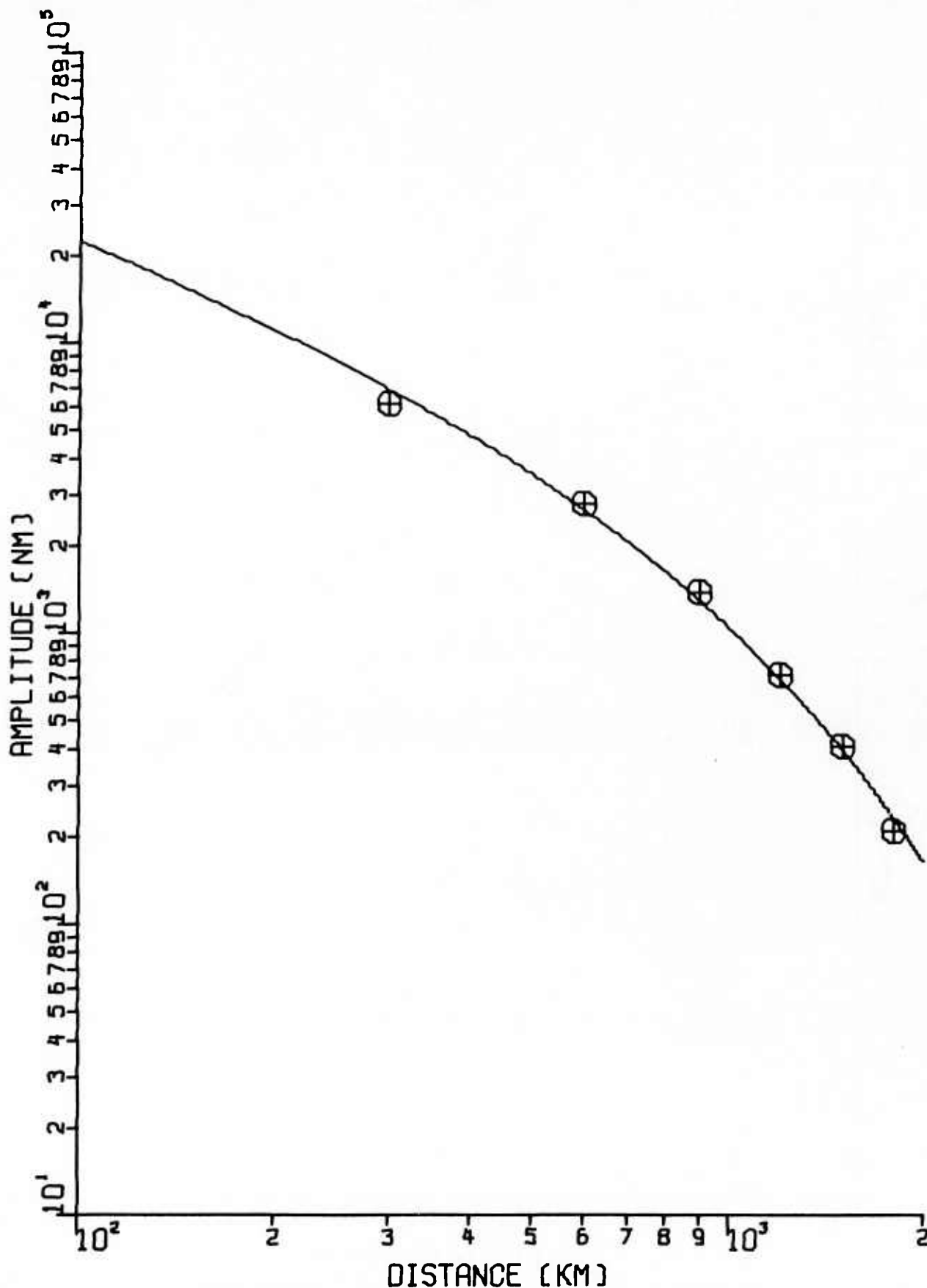


Figure 26g. depth = 10 km, rake = 45° , dip = 60° :
 $\gamma = 0.1415 \text{ deg}^{-1}$
 Amplitudes of envelope maxima of synthetic
 seismograms for the hard-rock model as
 observed at various distances.

(conventionally, $\alpha = 1.66$ for $T \approx 20$ sec). If we do attempt to approximate the observed amplitude decay curves by straight lines on these log-log plots, it appears that perhaps the best fits are given by slopes of -1 in the distance range $600 \text{ km} \leq \Delta \leq 900 \text{ km}$, -2 in the distance range $900 \text{ km} \leq \Delta \leq 1200 \text{ km}$, and -3 in the range $1200 \text{ km} \leq \Delta \leq 1800 \text{ km}$. For the 0.5 km-deep source, better fits are given by slopes of -1 for $300 \text{ km} \leq \Delta \leq 600 \text{ km}$ and by -2 for $600 \text{ km} \leq \Delta \leq 1800 \text{ km}$.

A potentially valuable technique for distinguishing earthquakes from explosions is the measurement of the phase velocity of the crustal surface wave L_g . We anticipate that since deeper sources preferentially excite the higher modes, they will generate signals which propagate at a higher phase velocity than do the signals from shallow sources, which are enriched in lower-order modes. Such an effect has been observed at the Yellowknife array by Barley (1978). As a crude rule of thumb, then, an L_g signal with a high phase velocity may be considered as evidence that the seismic source is located at intermediate or large depths within the crust, and hence that it is an earthquake rather than an explosion. In order to test this rule of thumb, we have simulated the measurement of L_g by a closely-spaced linear array. We have generated synthetic seismograms for nine receivers located along a line at distances of 500.0, 501.3, 502.2, 503.0, 503.5, 504.0, 504.8, 505.7, and 507.0 km from the source and also for nine other receivers located at distances of 1000.0, 1001.3, ..., 1007.0 km. Either one of these two linear arrays can be used to compute the phase velocity of a dispersed wavetrain by means of frequency-wavenumber (F-K) analysis (Barker et al., 1980b). We use the two arrays in order to see whether the phase velocity is affected by either dispersion or attenuation as the signal travels over longer paths. The results of the phase-velocity measurements for synthetic seismograms representing several different depths and focal mechanisms are shown in Table II. We have, in some cases, computed the phase velocity for two separate 0.4-Hz wide frequency bands, representing both a particular frequency band which was chosen to remain fixed for comparing different seismograms and another band which windows the frequency determined by an F-statistic test to contain the strongest signal for each individual case. It is important to note that

TABLE II

Phase Velocities for Synthetic Waveforms Generated Using the Hard-Rock Model

Depth (km)	Rake (degrees)	Dip (degrees)	Distance (km)	Frequency Range (Hz)	Phase Velocity (km/sec)
0.5	0	90	500	1.1 - 1.5	3.67
0.5	0	90	1000	1.1 - 1.5	3.79
5.0	0	90	500	{ 1.0 - 1.0 }	{ 3.37 }
				{ 1.2 - 1.6 }	{ 3.43 }
5.0	0	90	1000	1.1 - 1.5	3.46
				{ 1.0 - 1.4 }	{ 3.27 }
10.0	0	90	500	1.1 - 1.5	3.79
				{ 1.2 - 1.6 }	{ 3.76 }
20.0	0	90	500	1.1 - 1.5	4.01
				{ 1.2 - 1.6 }	{ 4.66 }
20.0	0	90	1000	1.1 - 1.5	3.88
40.0	0	90	500	1.1 - 1.5	4.66
				{ 0.6 - 1.0 }	{ 4.71 }
40.0	0	90	1000	1.1 - 1.5	4.63
				{ 0.5 - 0.9 }	{ 4.49 }
10.0	90	90	500	1.1 - 1.5	4.33
				{ 1.3 - 1.7 }	{ 4.01 }
10.0	45	60	500	1.1 - 1.5	3.91
				{ 1.3 - 1.7 }	{ 3.88 }
10.0	45	90	500	1.2 - 1.6	3.86
10.0	0	60	500	1.2 - 1.6	3.74
10.0	90	60	500	1.2 - 1.6	4.29
10.0	0	45	500	1.2 - 1.6	4.41
10.0	45	45	500	1.2 - 1.6	4.41
10.0	90	45	500	1.2 - 1.6	4.15

a 128-point (i.e., 25.6-sec) time-domain window was chosen which included the maximum-amplitude segment of the signal. Moving the window forward or backward in time will change the value which is measured for the phase velocity for each frequency band, as we shall demonstrate later. Table II shows that our rule of thumb about higher phase velocities for deeper events has some validity, but there is a large scatter in the measurements which tends to blur out any depth dependence in C_L . We have already noted that the phase velocity is dependent on both the time and frequency windows which are selected for analysis; we observe from Table II that it is also dependent on the distance from the source to the receiver and on the focal mechanism of the source. In particular, we note that for a consistently chosen time- and frequency-domain window at a fixed distance of 500 km from a 10-km deep source, the phase velocity varies between 3.743 km/sec for a strike-slip fault dipping at 60° and 4.412 km/sec for a strike-slip fault (or for one with equal strike-slip and thrust components) dipping at 45° . Since this variability at a single depth is half as large as the variability over all depths shown in Table II, we see that L_g phase velocity perhaps does serve as a seismic discriminant, but only a weak one. It is also possible, however, that our 5 samples/sec synthetic seismograms are inadequate for showing the power of this discriminant, as we shall discuss later.

Soft Rock Model

We shall now repeat the preceding analysis, this time using synthetic seismograms generated using the "soft-rock" model of a shield structure overlain by strongly attenuating sediments. Figure 27 shows that the low-Q layer effectively absorbs all energy propagating in the fundamental mode, even for a shallow source which tends to excite that mode preferentially (cf. Figure 21). It is also shown that, as was anticipated on the basis of Figure 13, this earth model acts as a low-pass filter, especially for the lower-order modes. This filter effect is also evident in Figures 28 and 29, which show the wavetrains for a 10-km deep earthquake as recorded at distances of 500 and 1000 km. We see that the high frequencies become less and less prominent the further the wavetrain propagates. Figure 30 shows the envelope maxima

CANADIAN SHIELD, 2 KM SEDIMENTS

SLIP 0.0 DIP 90.0 FAKE 0.0 MOMENT = 10²²

DEPTH = 0.5 KM

LG : SELECTED MODES DIST = 500.0 KM AZIMUTH = 0.0 LRSM

671 km

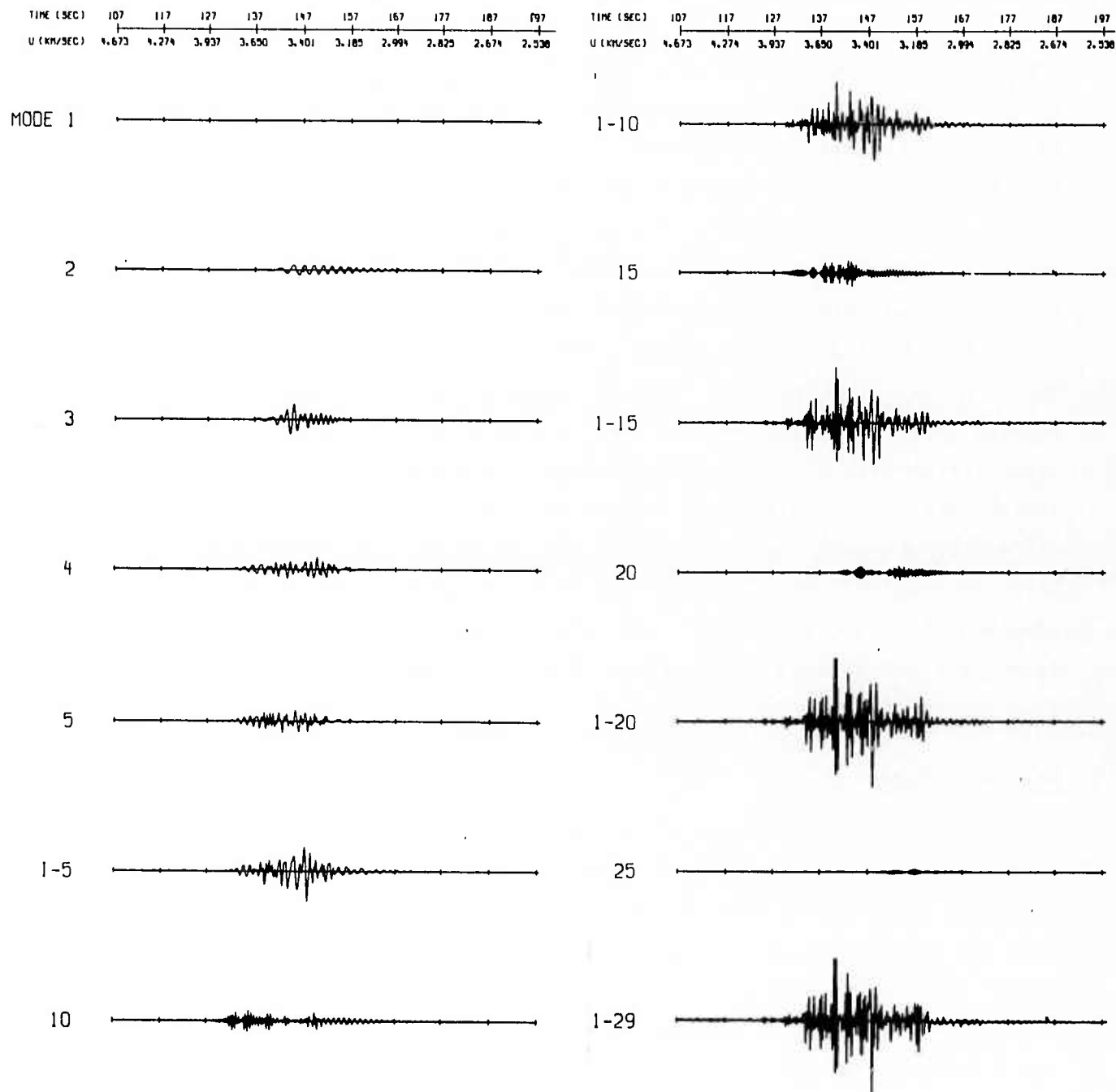


Figure 27. Synthetic seismogram for a strike-slip source 0.5 km deep in the soft-rock model.

CANADIAN SHIELD, 2 KM SEDIMENTS

STRIKE = 0.0 DIP = 90.0 RAKE = 0.0 MOMENT = 10^{22}

DEPTH = 10.0 KM

LG • SELECTED MODES DIST = 500.0 KM AZIMUTH = 0.0 LRSM

1235 mm

TIME (SEC) 107 117 127 137 147 157 167 177 187
U (KM/SEC) 4.673 4.274 3.937 3.650 3.401 3.185 2.994 2.825 2.674

TIME (SEC) 107 117 127 137 147 157 167 177
U (KM/SEC) 4.673 4.274 3.937 3.650 3.401 3.185 2.994 2.825

MODE 1

1-10

2

15

3

1-15

4

20

5

1-20

1-5

25

10

1-29

Figure 28. Synthetic seismogram for a strike-slip source 10.0 km deep in the soft-rock model as observed at a distance of 500 km.

CANADIAN SHIELD, 2 KM SEDIMENTS

STRIKE = 0.0 DIP = 90.0 RAKE = 0.0 MOMENT = 10^{22}

DEPTH = 10.0 KM

LG = SELECTED MODES DIST = 1000.0 KM AZIMUTH = 0.0 LRSM

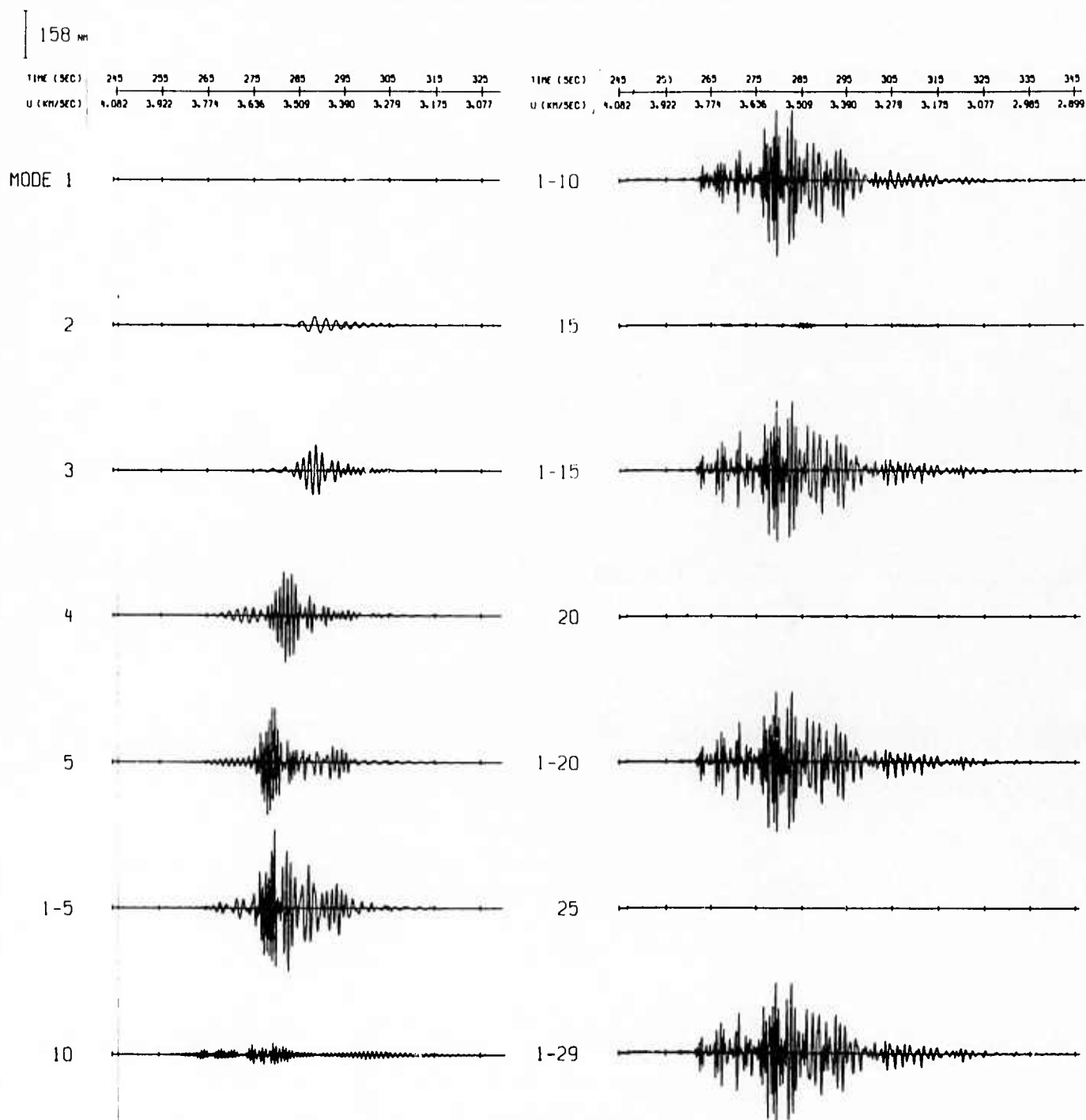


Figure 29. Synthetic seismogram for a strike-slip source 10.0 km deep in the soft-rock model as observed at a distance of 1000 km.

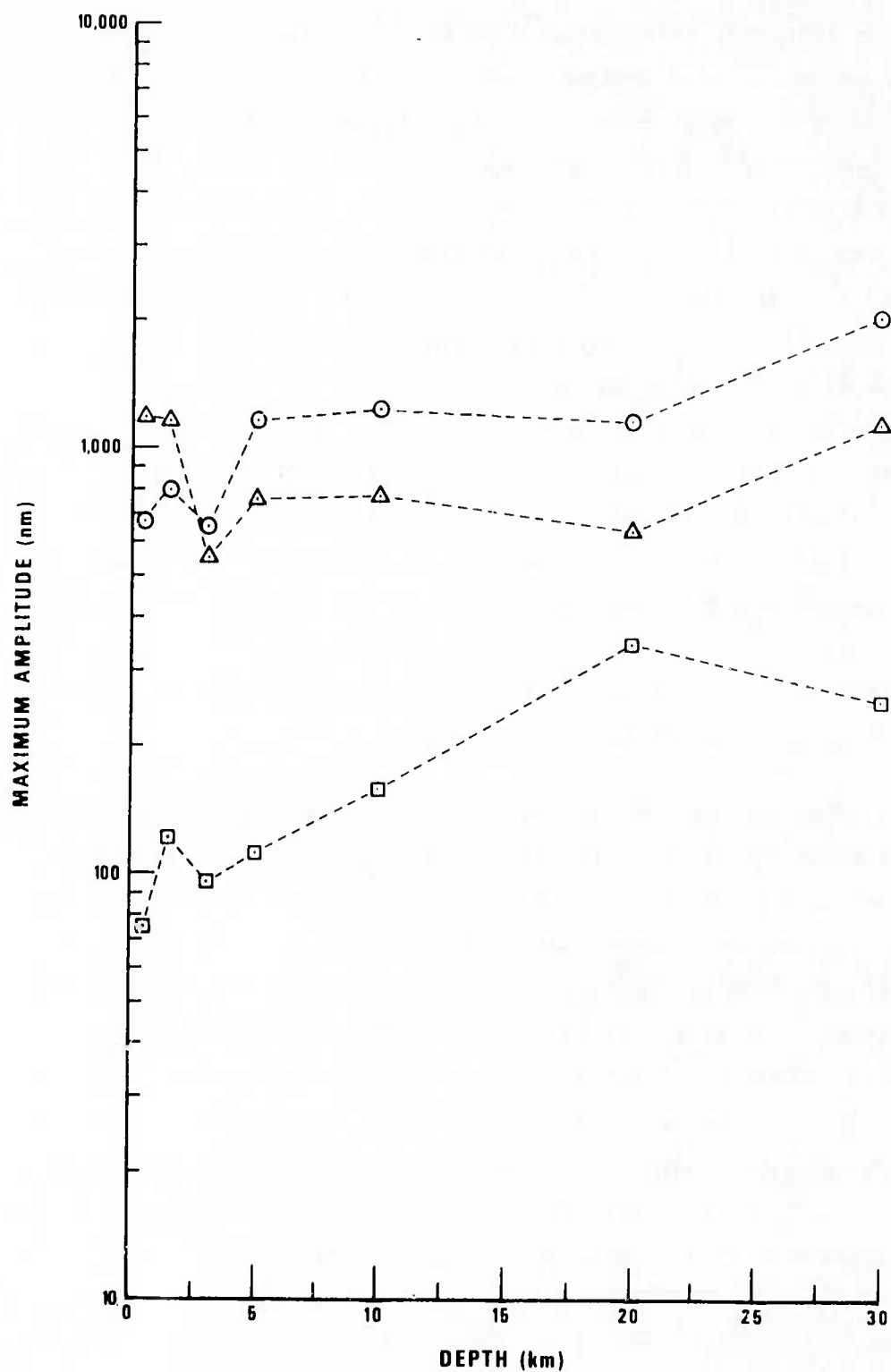


Figure 30. Amplitudes of envelope maxima of synthetic seismograms for sources at various depths in the soft-rock model.
 Circles: rake = 0° , dip = 90° , strike = 0° , Δ = 500 km.
 Triangles: rake = 40° , dip = 70° , strike = 30° , Δ = 500 km.
 Squares: rake = 0° , dip = 90° , strike = 0° , Δ = 1000 km.

for soft-rock synthetic seismograms computed using the same focal mechanisms, distances, and depths as were used for the hard-rock model in Figure 25. The amplitudes are no longer large for shallow events, since the lower-order modes are strongly attenuated. It should be noted that the amplitudes in Figure 30 are smaller for sources at a depth of 3 km than at depths of 1.5 and 5 km. The signals from 5-km deep sources are stronger than are those from 3-km deep sources because the deeper events are more effective at generating higher-mode energy, which is less attenuated at distance than is the energy in the lowest-order modes. The signals from 1.5-km deep sources are stronger than are those from 3-km sources because they are trapped by the big increase in shear-wave velocity at the base of the 2-km thick sedimentary layer. This is especially true for the case denoted by triangles in Figure 30, since for events with this focal mechanism the excitation of Love waves is more strongly affected by the low value of the modulus of rigidity at the hypocenter than are the pure strike-slip events, which are denoted in Figure 30 by circles and squares (Harkrider, 1970).

Figure 31 shows that the attenuation is in fact unrealistically high: γ is about three times larger than is commonly observed. This too-large value of γ is of course brought about by the low value of Q_β , independent of frequency, which was used for the 2-km thick sedimentary layer overlying the shield structure. Table III shows that the phase velocity cannot be used effectively as a depth discriminant for signals in this model, since the measured values of C_L depend not only on depth but also on Δ . As the waveform travels from $\Delta = 500$ km to $\Delta = 1000$ km, the lower-order modes vanish and so what remains are the higher-order modes for which C_L is greater. The phase velocity thus increases as the amplitude decreases with increasing source-to-receiver separation.

Constant Q Model

As we have stated, we feel that the anomalously large value which we found for γ was brought about by our using too low a value for Q_β in the 2-km thick sedimentary layer. In order to isolate the effects introduced by the elastic parameters β and ρ in the sediments as opposed to the effects of Q_β , we have generated another set of synthetic

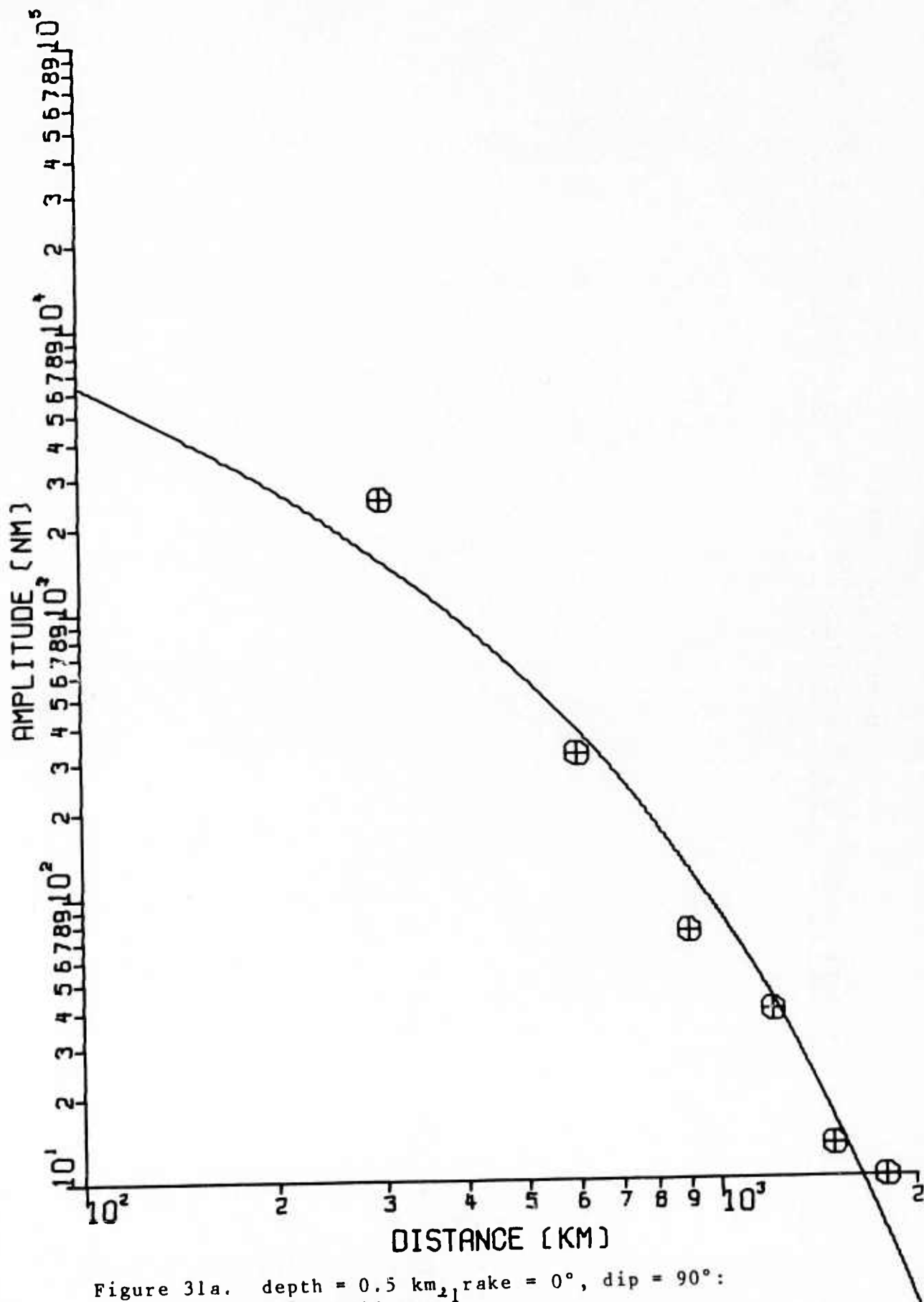


Figure 31a. depth = 0.5 km, rake = 0°, dip = 90°:
 $\gamma = 0.2946$ deg
 Amplitudes of envelope maxima of synthetic
 seismograms for the soft-rock model as
 observed at various distances:

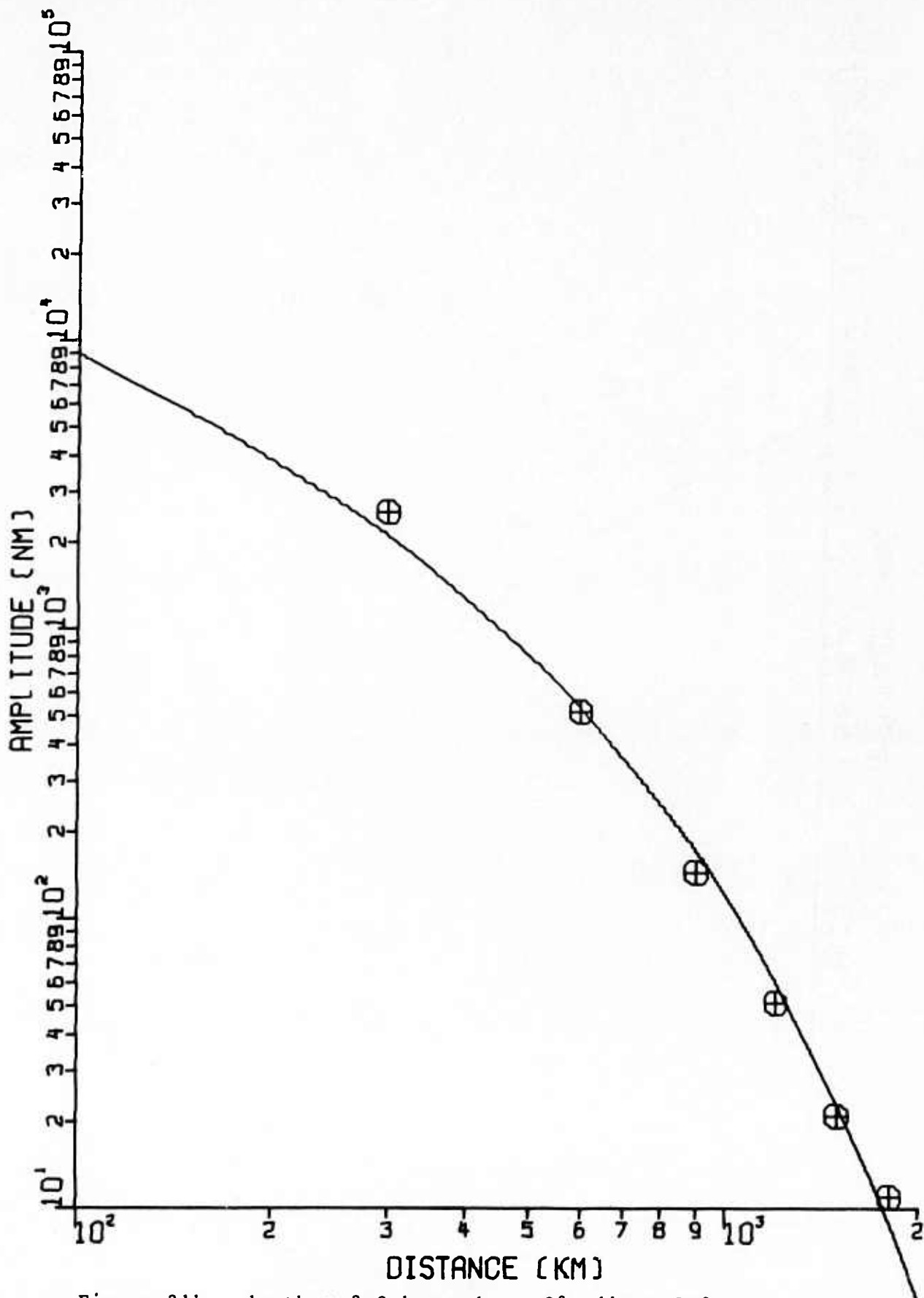


Figure 31b. depth = 3.0 km, rake = 0°, dip = 90°:
 $\gamma = 0.2955$ deg
 Amplitudes of envelope maxima of synthetic
 seismograms for the soft-rock model as
 observed at various distances:

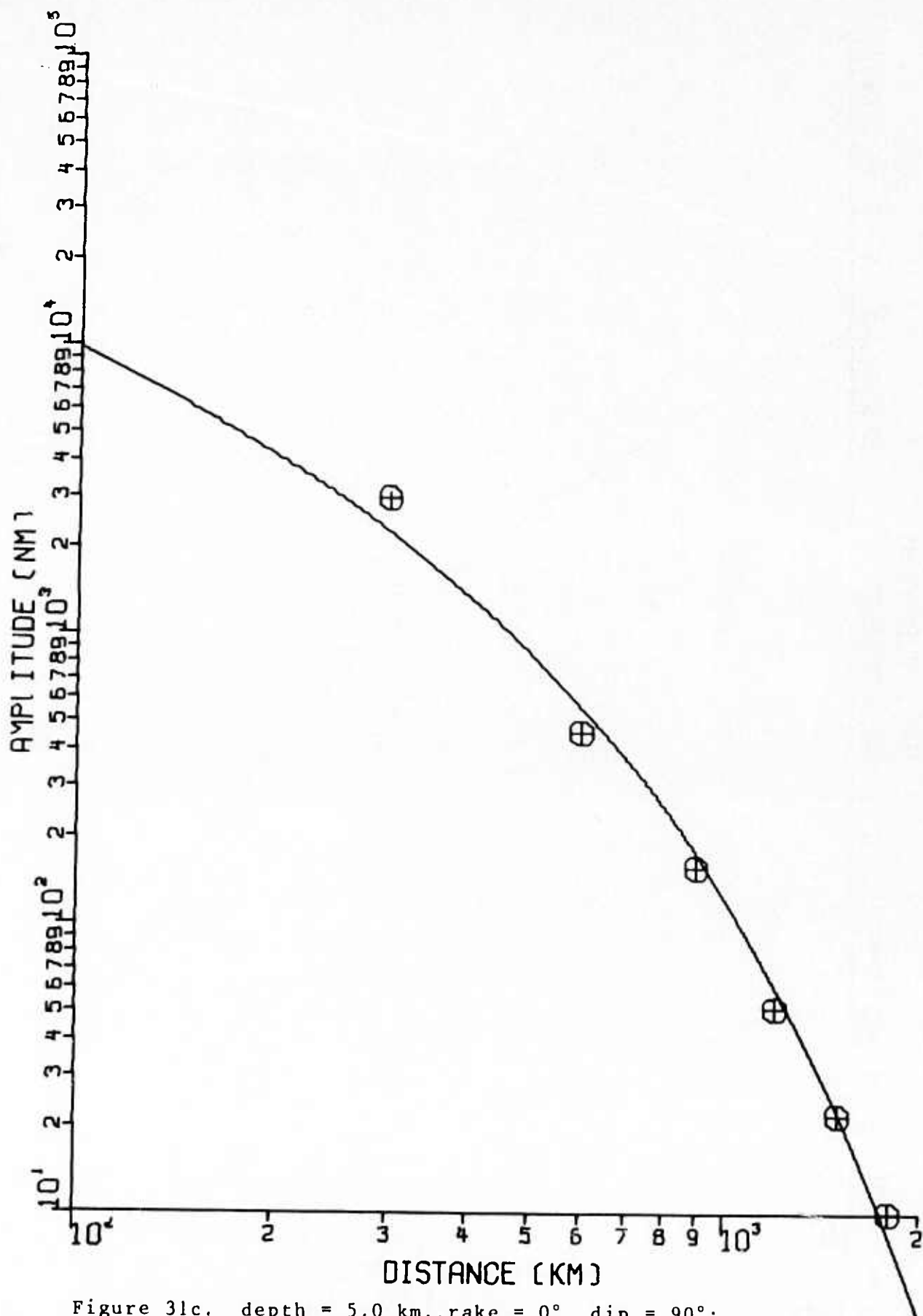


Figure 3lc. depth = 5.0 km, rake = 0° , dip = 90° :
 $\gamma = 0.3041$ deg
 Amplitudes of envelope maxima of synthetic
 seismograms for the soft-rock model as
 observed at various distances:

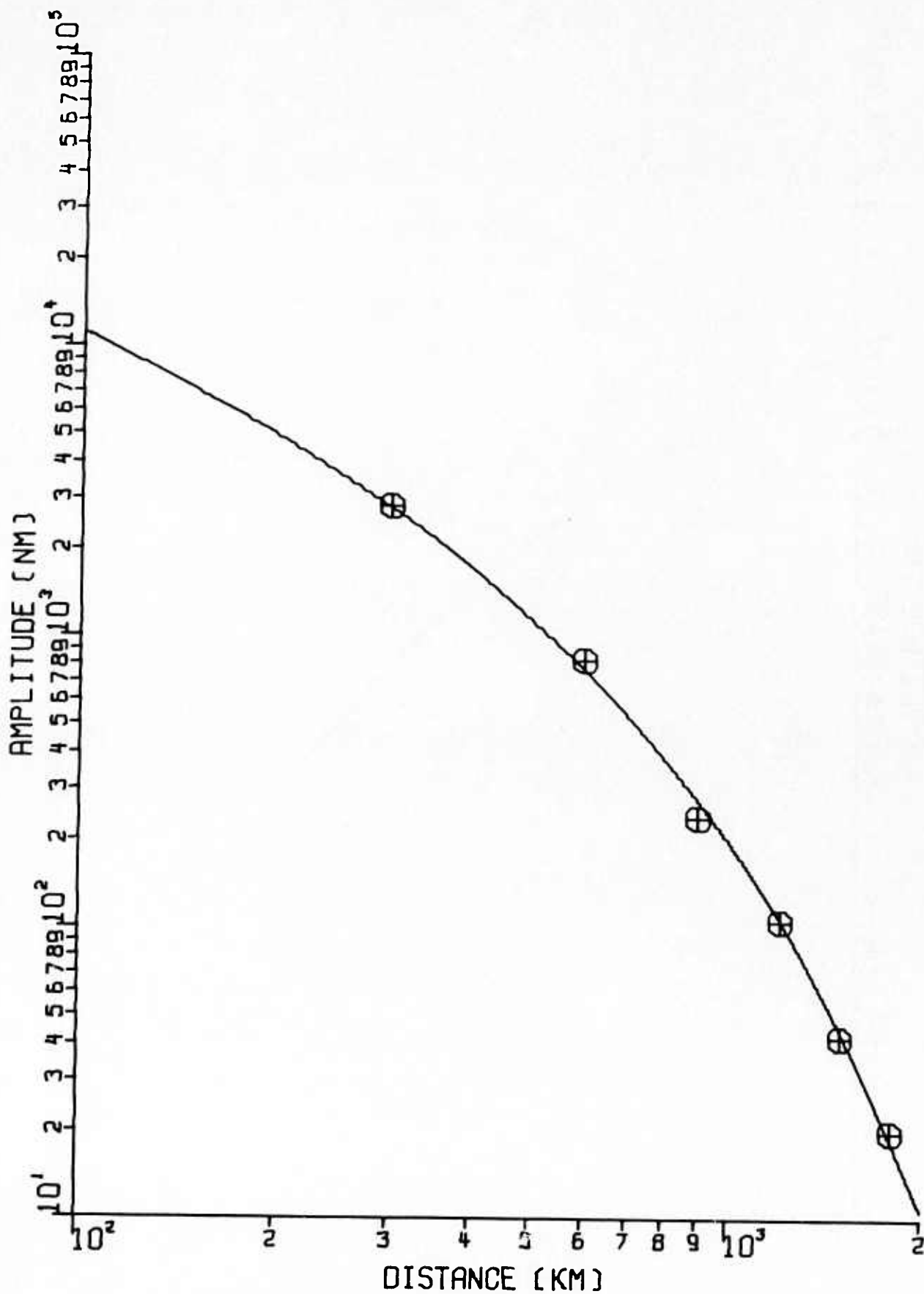


Figure 3ld. depth = 10.0 km, rake = 0°, dip = 90°:
 $\gamma = 0.2601$ deg
 Amplitudes of envelope maxima of synthetic
 seismograms for the soft-rock model as
 observed at various distances:

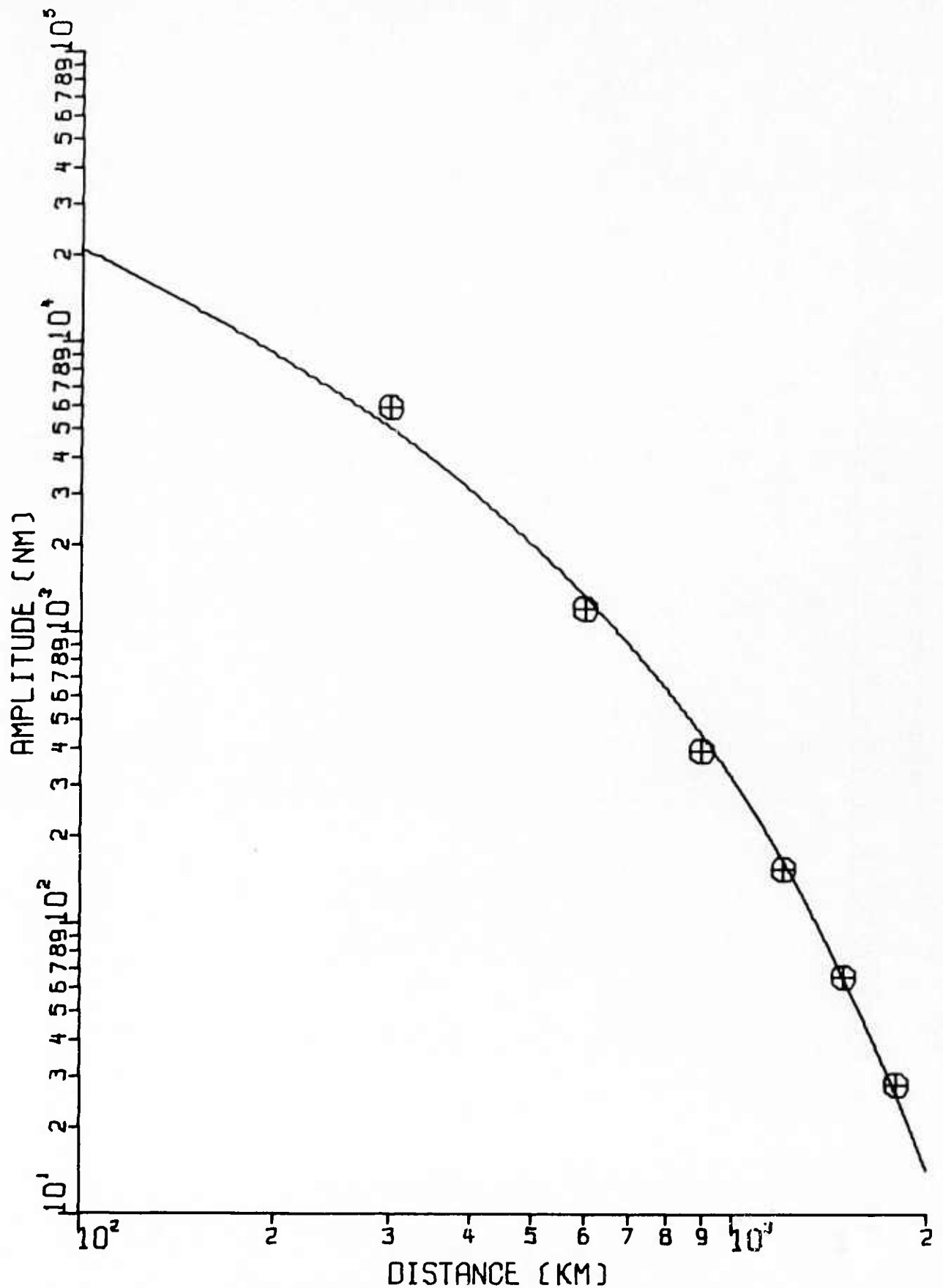


Figure 3le. depth = 20.0 km, rake = 0° , dip = 90° :
 $\gamma = 0.2807$ deg
 Amplitudes of envelope maxima of synthetic
 seismograms for the soft-rock model as
 observed at various distances:

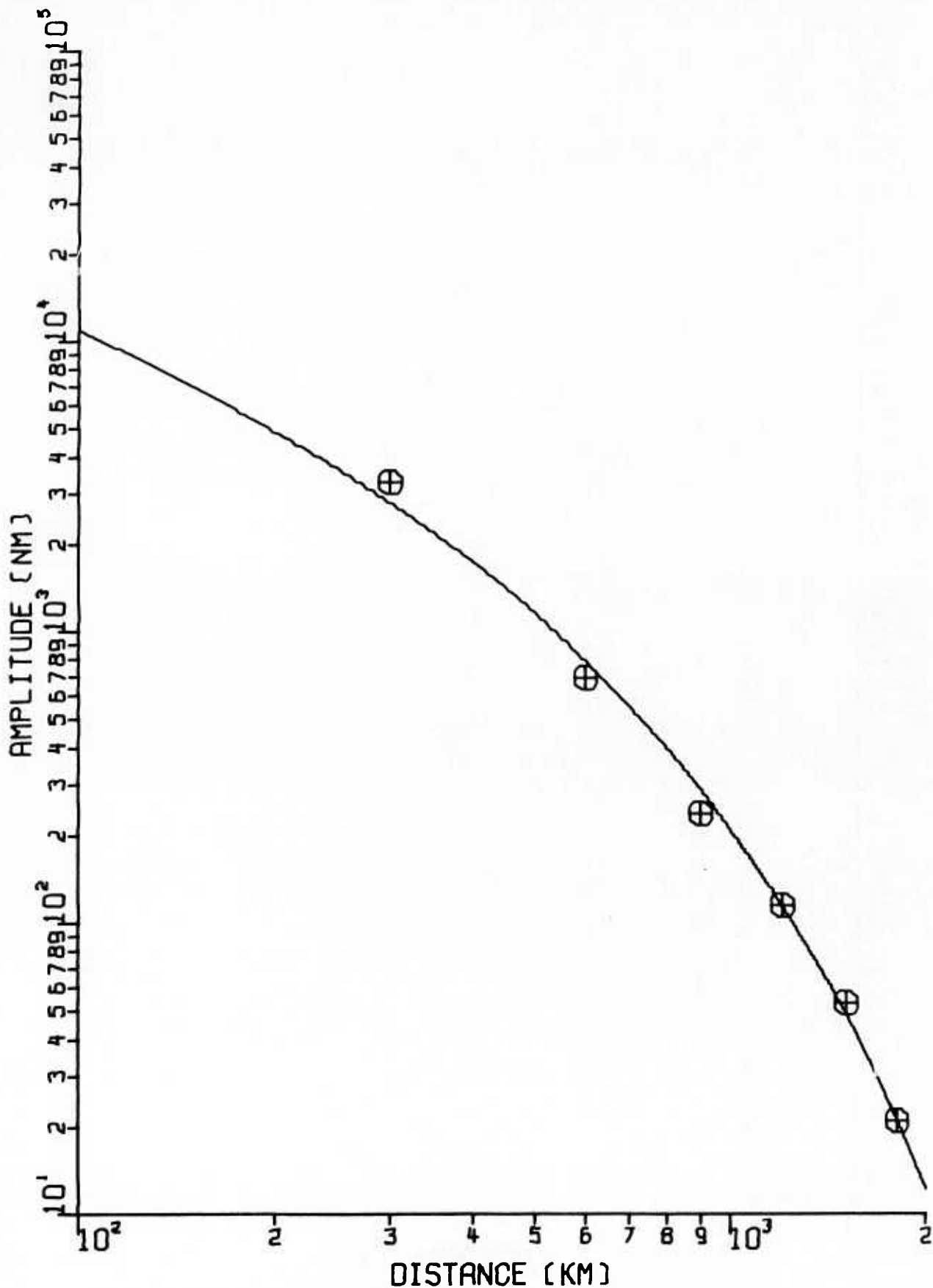


Figure 3lf. depth = 30.0 km, rake = 0° , dip = 90° :
 $\gamma = 0.2514$ deg
 Amplitudes of envelope maxima of synthetic
 seismograms for the soft-rock model as
 observed at various distances:

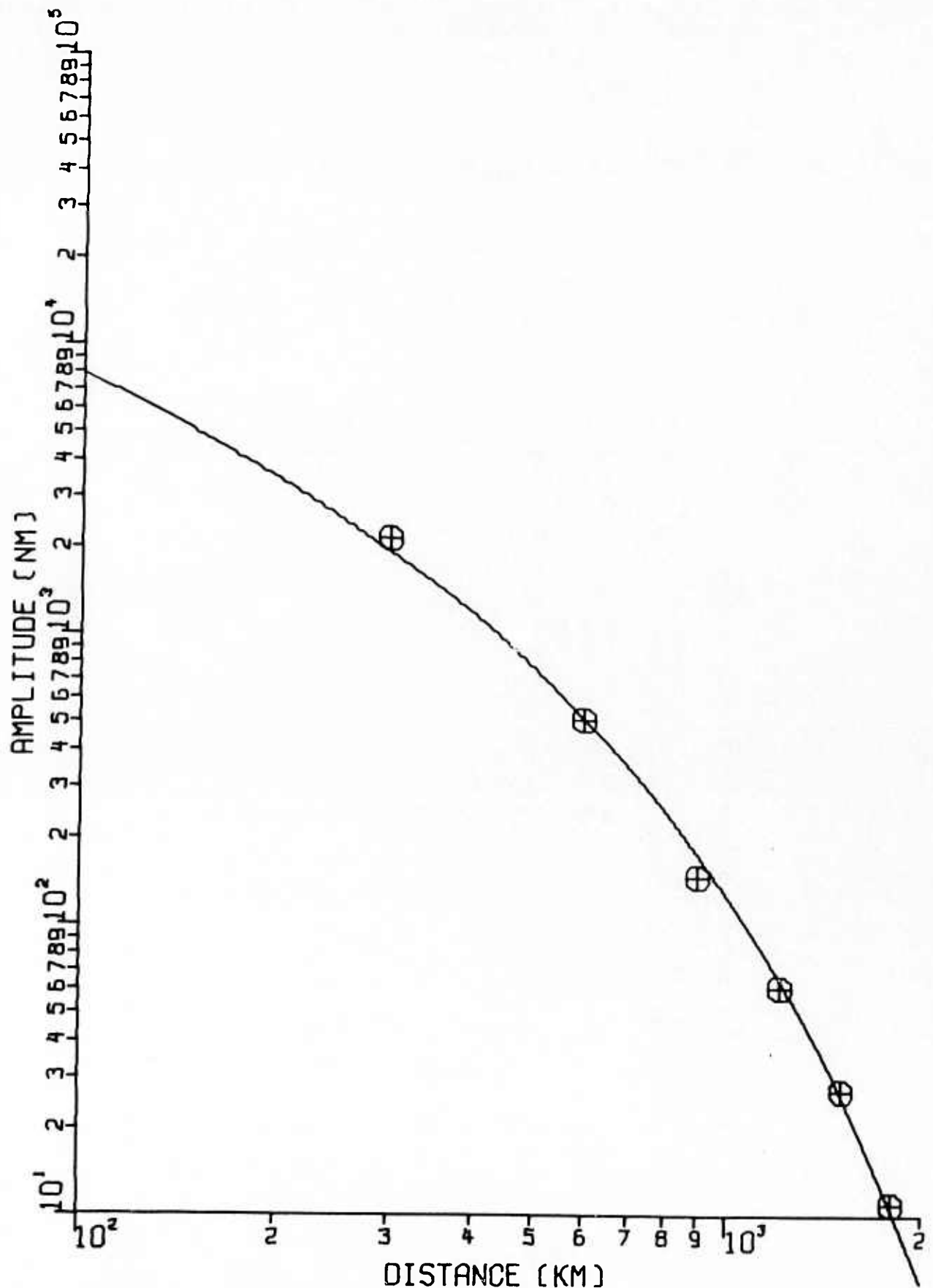


Figure 3lg. depth = 10.0 km₁, rake = 45°, dip = 60°:
 $\gamma = 0.2760$ deg
 Amplitudes of envelope maxima of synthetic
 seismograms for the soft-rock model as
 observed at various distances:

TABLE III
Phase Velocities for Synthetic Waveforms Generated Using the Soft-Rock Model

Depth (km)	Rake (degrees)	Dip (degrees)	Distance (km)	Frequency Range (Hz)	Phase Velocity (km/sec)
0.5	0	90	500	1.2 - 1.6	3.64
0.5	0	90	1000	0.8 - 1.2	4.53
3.0	0	90	500	1.1 - 1.5	4.40
3.0	0	90	1000	0.8 - 1.2	3.71
5.0	0	90	500	1.0 - 1.4	4.18
5.0	0	90	1000	{ 1.1 - 1.5 }	{ 4.18 }
10.0	0	90	500	0.8 - 1.2	4.22
10.0	0	90	1000	{ 1.0 - 1.4 }	{ 3.79 }
20.0	0	90	500	0.9 - 1.3	3.84
20.0	0	90	1000	{ 1.0 - 1.4 }	{ 4.04 }
30.0	0	90	500	1.1 - 1.5	3.91
30.0	0	90	1000	{ 1.0 - 1.4 }	{ 3.91 }
50.0	0	90	500	1.0 - 1.4	3.91
50.0	0	90	1000	1.0 - 1.4	4.04
100.0	0	90	500	1.0 - 1.4	4.04
100.0	0	90	1000	1.0 - 1.4	4.04

seismograms for the soft-rock model, this time keeping Q constant at 1000, even for the sedimentary layer. The dependence of amplitude on depth in this model is shown in Figure 32; note that the focal mechanism represented by the triangles is different from the one in Figures 25 and 30. As one would expect, the amplitudes for the deep ($h \geq 10$ km) sources are roughly the same in Figures 25 and 32, since the two models appear almost identical to the deeper-penetrating higher modes. This is in contrast to the situation shown in Figure 30, where the sedimentary layer exerts a major influence on the amplitudes of the wavetrains from even the deepest sources. We conclude that this influence is due almost entirely to the Q_β , and not to β and ρ , in the sedimentary layer. For shallow sources, however, we see that the presence of the sedimentary layer reduces the amplitudes from those of the hard-rock model even if the value of Q_β is left at 1000. This reduction is due to the absence of the fundamental mode from the portion of the wavetrain in which L_g is measured. Figure 11 shows that the modal superposition which constitutes L_g propagates at about 3.5 km/sec, but the Airy phases of the four lowest order modes propagate at velocities of less than 2.0 km/sec. The fundamental mode will thus arrive much later (by 107 sec at $z = 500$ km) than does the phase which is taken to be L_g , so it will contribute little to the measured L_g amplitude, regardless of Q_β . Figure 11 shows that the portion of the fundamental mode which is contained within the L_g velocity window is at frequencies too low to be seen by a short-period seismograph, so L_g in the soft-rock model will not contain the large pulse-like fundamental mode arrivals which characterized the wavetrains of shallow sources in the hard-rock model.

We note that in practice no late arrivals are actually observed which can be identified as uncontaminated fundamental mode wavetrains. It was, of course, in order to explain the absence of the fundamental mode that the strong attenuation was introduced into the model. We see in Figure 32 that simple dispersion, rather than attenuation, is sufficient to remove the fundamental mode from L_g in the soft-rock model; we must still, however, find a way to account for the absence on real seismograms of the predicted late-arriving fundamental mode wavetrain. Although introducing low Q_β into the sedimentary layer did

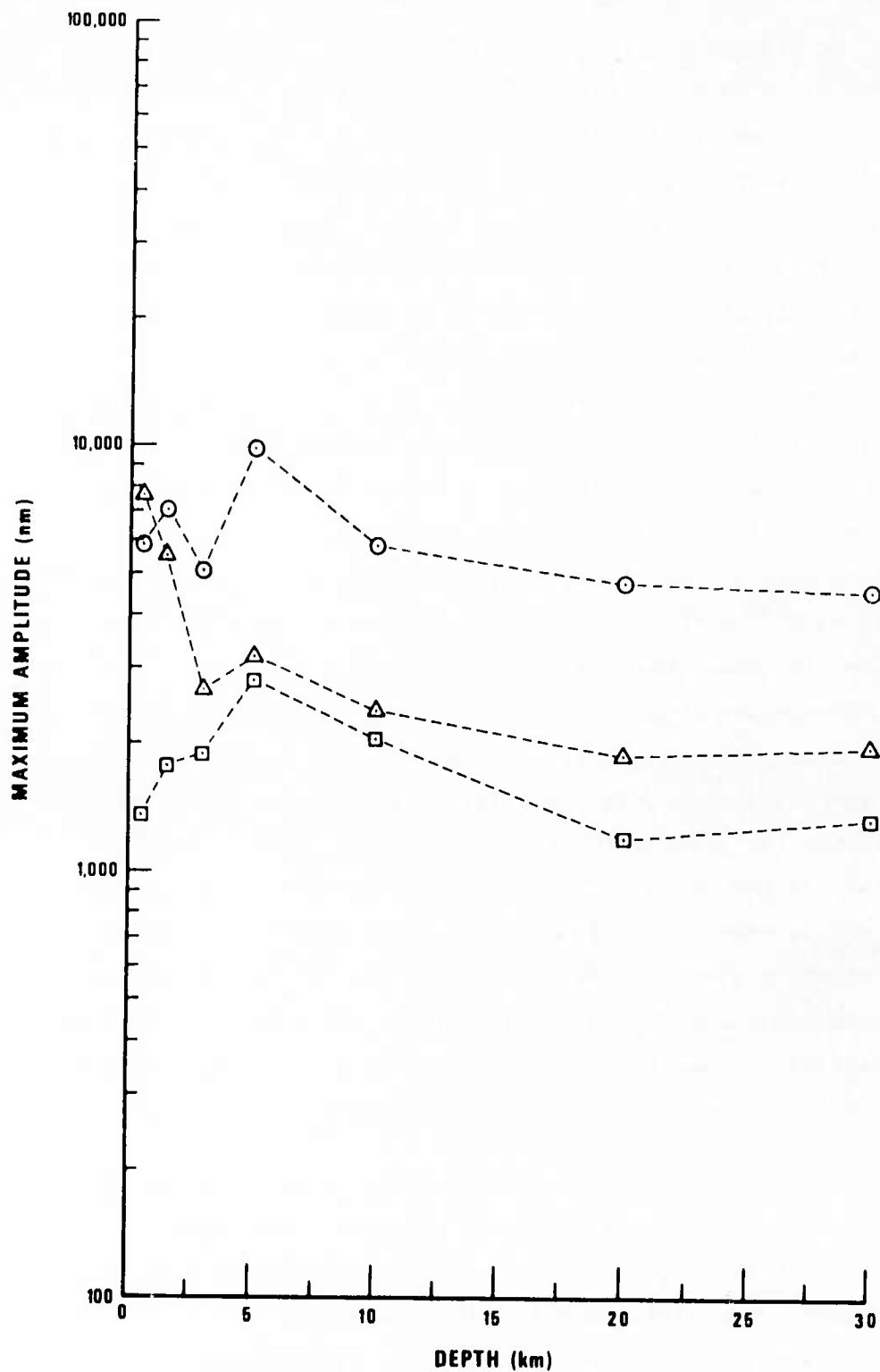


Figure 32. Amplitudes of envelope maxima of synthetic seismograms for sources at various depths in the high-Q soft-rock model.
 Circles: rake = 0° , dip = 90° , strike = 0° , Δ = 500 km.
 Triangles: rake = -30° , dip = 70° , strike = 40° , Δ = 500 km.
 Squares: rake = 0° , dip = 90° , strike = 0° , Δ = 1000 km.

suppress this later phase, we have seen that it led to unacceptably large values of γ for L_g . We therefore feel that a more likely explanation of the absence of the fundamental mode is scattering. It is at least a viable hypothesis that, on account of topography and geological heterogeneity, the upper layer of the crust is more effective at scattering the surface-wave energy trapped within it than are the lower crustal layers. If this be true, then scattering will more strongly dissipate the shallow fundamental mode than the deeper modes which contribute to L_g in the soft-rock model. Scattering will also prolong the L_g coda, thus obscuring any sharp fundamental mode arrival. We therefore believe that a more accurate model of L_g propagation could be formulated by using a higher value of Q_β in the sedimentary layer, say perhaps $Q_\beta \approx 200$, and introducing a mechanism for scattering at shallow depths. Figure 33 shows that a more nearly realistic, but still somewhat too large, value of γ would be obtained in the soft-rock model if Q_β were larger. We note that phase velocity is still a poor depth discriminant in this model even if $Q_\beta = 1000$ in the sedimentary layer, since L_g (defined as the phase which propagates at about 3.5 km/sec) contains little energy from the lower-order, shallow modes, and thus the phase velocity is high, regardless of source depth.

A comparison of the synthetic L_g seismograms with real waveforms has been presented elsewhere (Der et al., 1981). The synthetic seismograms which were used in that report differ somewhat from those which have been presented herein, since the upper (i.e., sedimentary) layers of the crust were modified to represent the structure for individual stations. It was found that the envelopes of the synthetic seismograms decay faster than do those of the real waveforms, i.e., the synthetics do not contain long enough codas. As we have stated, we believe that in order to reproduce on the synthetics the prolonged envelopes which are characteristic of real data, it will be necessary to take account of the late-arriving energy which arrives at the receiver by scattering rather than by travelling along the direct path. The observed coda shapes exhibit significant variations even among stations close to each other, thereby showing that localized site effects can dominate the behavior of L_g . Evidence for the effects on L_g of strictly

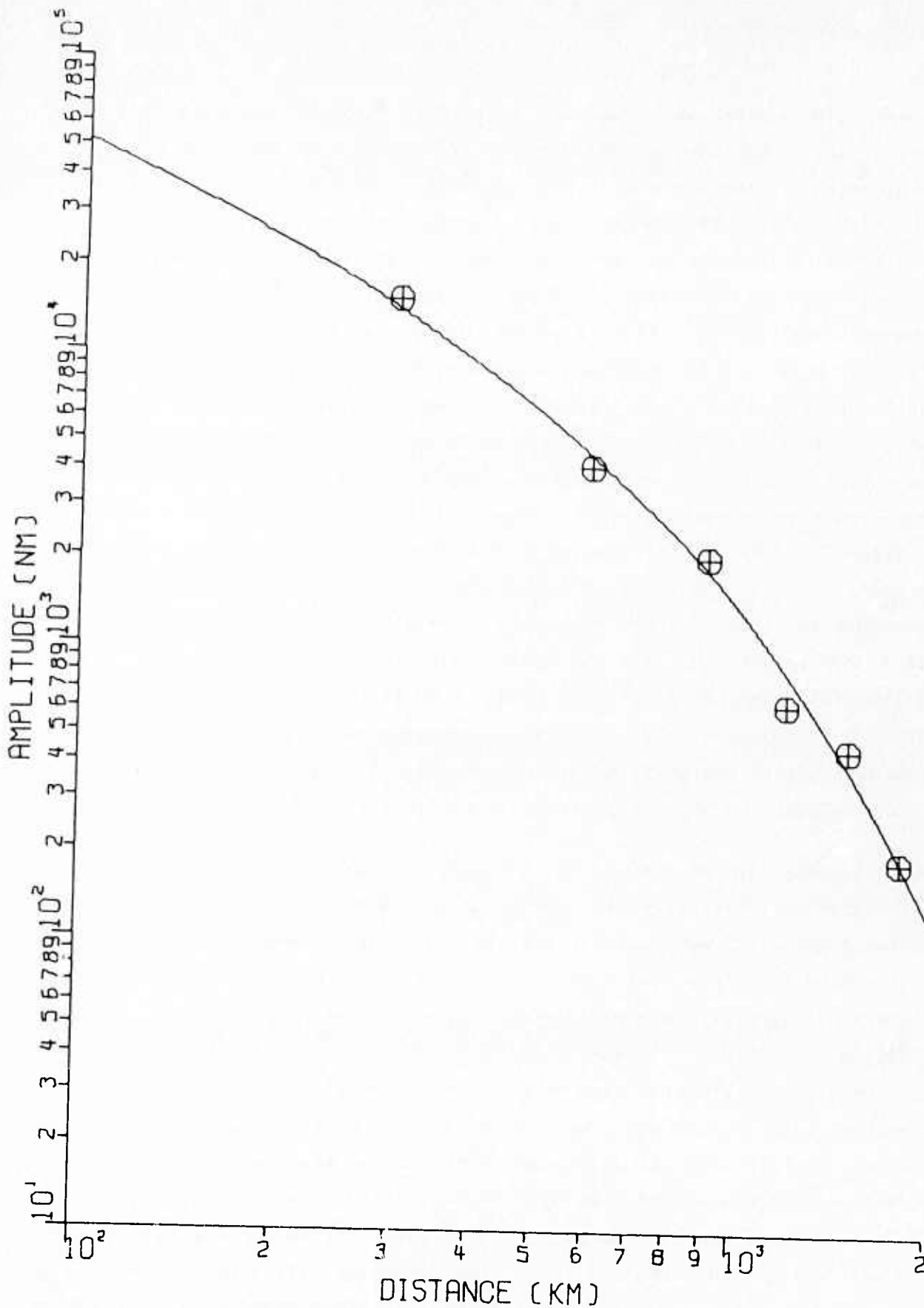


Figure 33a. depth = 0.5 km, rake = 0°, dip = 90°:
 $\gamma = 0.2096$ deg
 Amplitudes of envelope maxima of synthetic
 seismograms for the high-Q soft-rock model as
 observed at various distances:

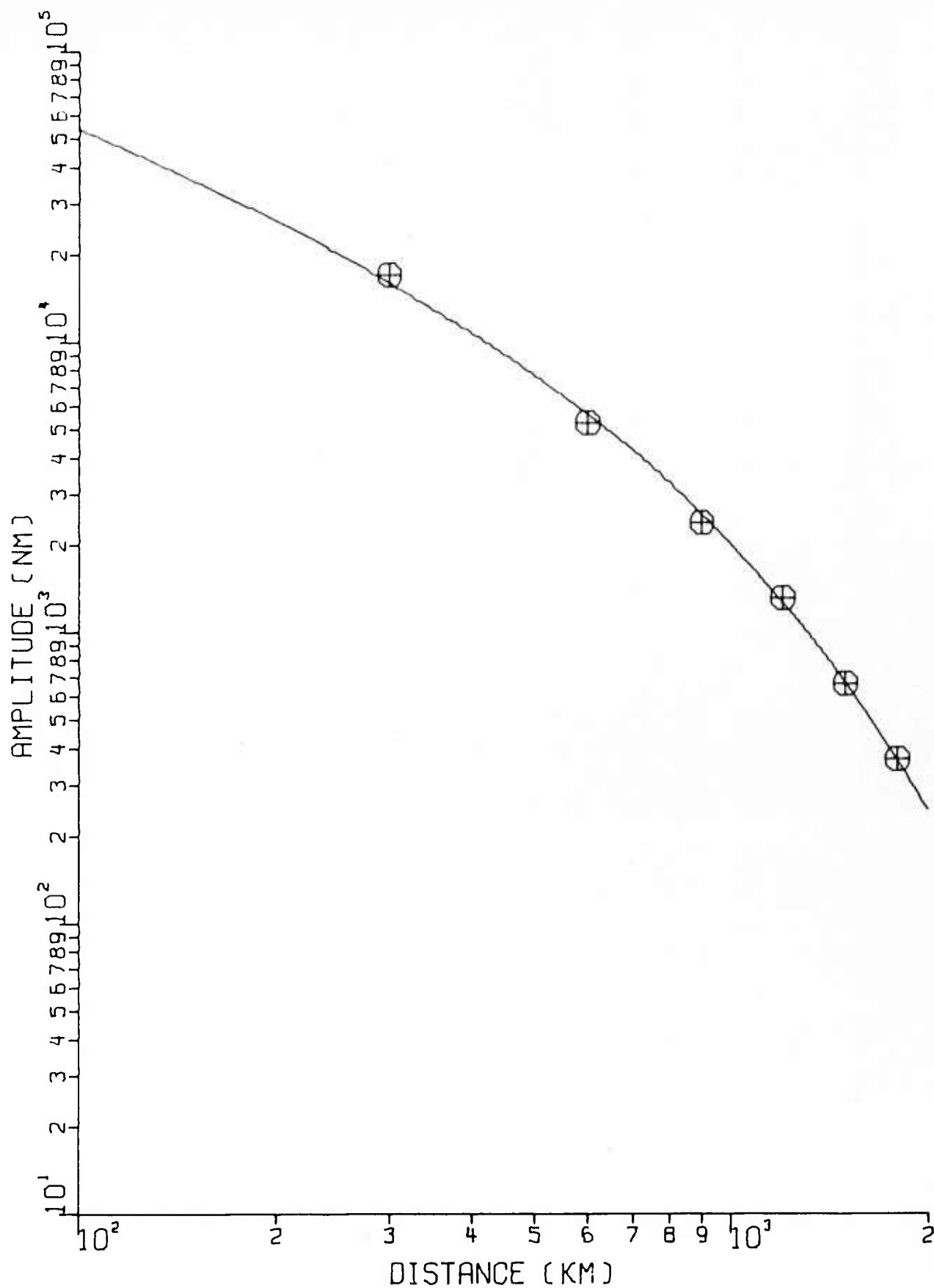


Figure 33b. depth = 3.0 km, rake = 0°, dip = 90°;
 $\gamma = 0.1704$ deg
 Amplitudes of envelope maxima of synthetic
 seismograms for the high-Q soft-rock model as
 observed at various distances:

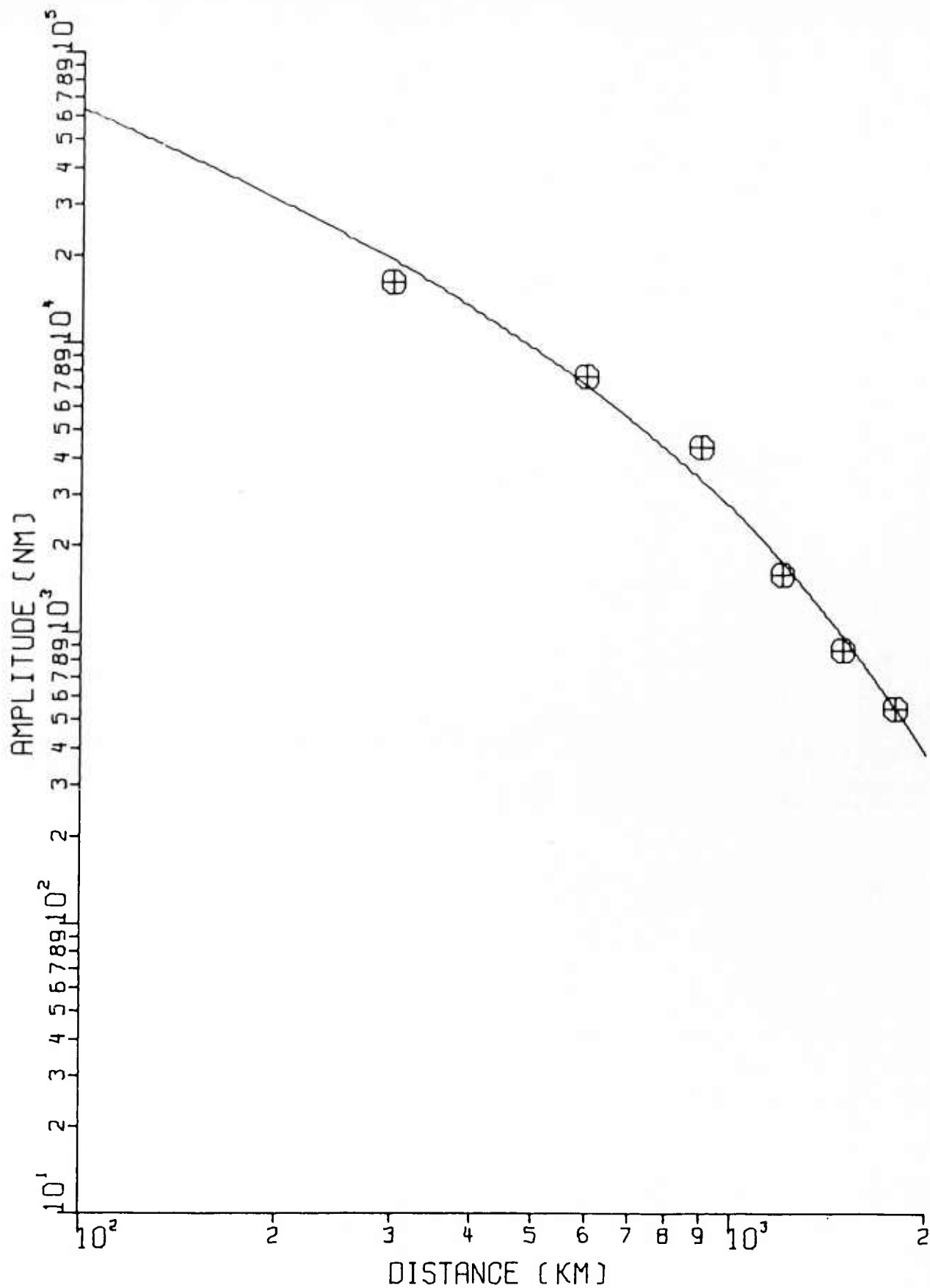


Figure 33c. depth = 5.0 km, rake = 0°, dip = 90°:
 $\gamma = 0.1538$ deg
 Amplitudes of envelope maxima of synthetic
 seismograms for the high-Q soft-rock model as
 observed at various distances:

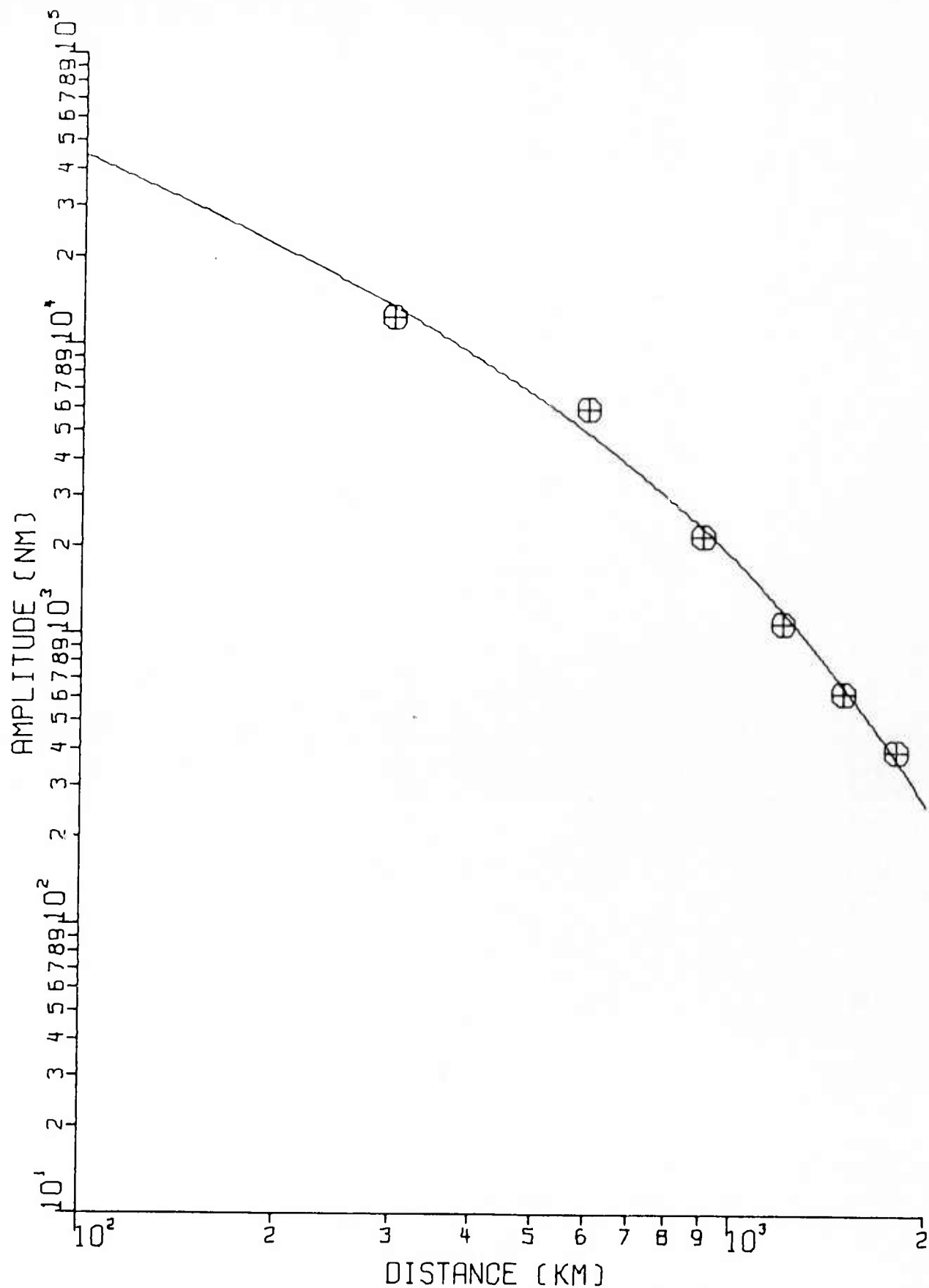


Figure 33d. depth = 10.0 km, rake = 0°, dip = 90°:
 $\gamma = 0.1555$ deg
 Amplitudes of envelope maxima of synthetic
 seismograms for the high-Q soft-rock model as
 observed at various distances:

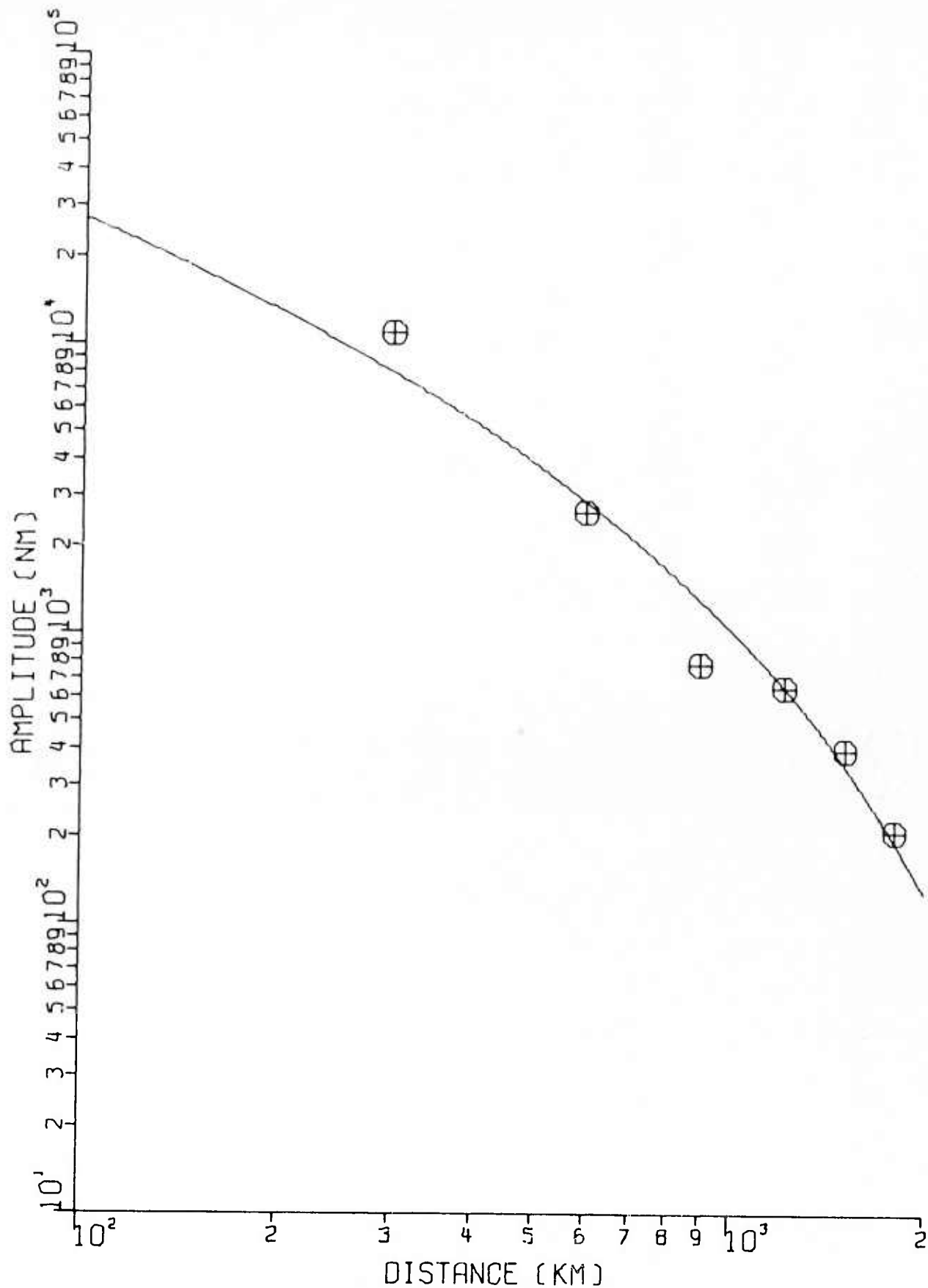


Figure 33e. depth = 20.0 km, rake = 0° , dip = 90° :
 $\gamma = 0.1665$ deg
 Amplitudes of envelope maxima of synthetic
 seismograms for the high-Q soft-rock model as
 observed at various distances:

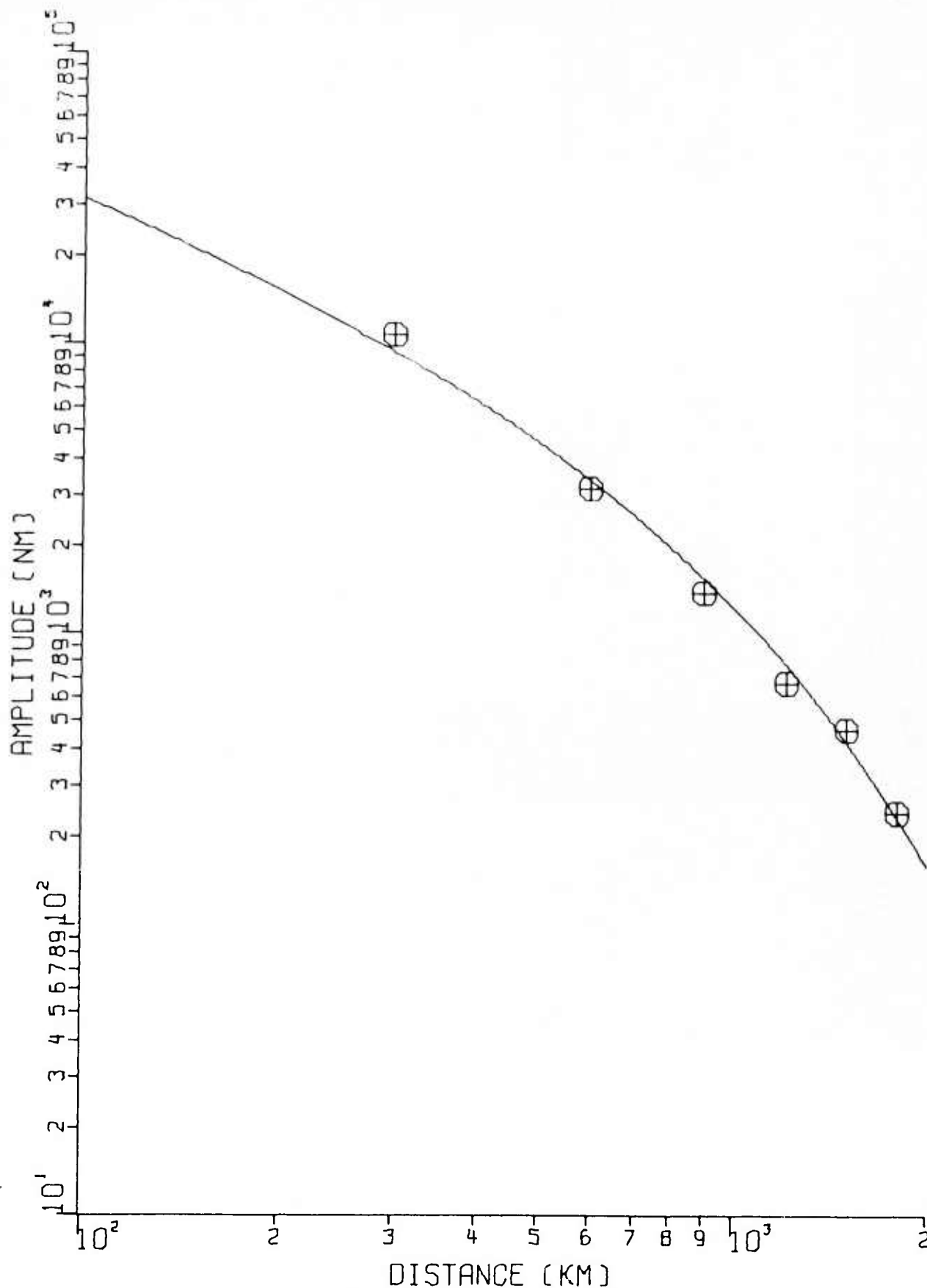


Figure 33f. depth = 30.0 km, rake = 0°, dip = 90°:
 $\gamma = 0.1632$ deg
 Amplitudes of envelope maxima of synthetic
 seismograms for the high-Q soft-rock model as
 observed at various distances:

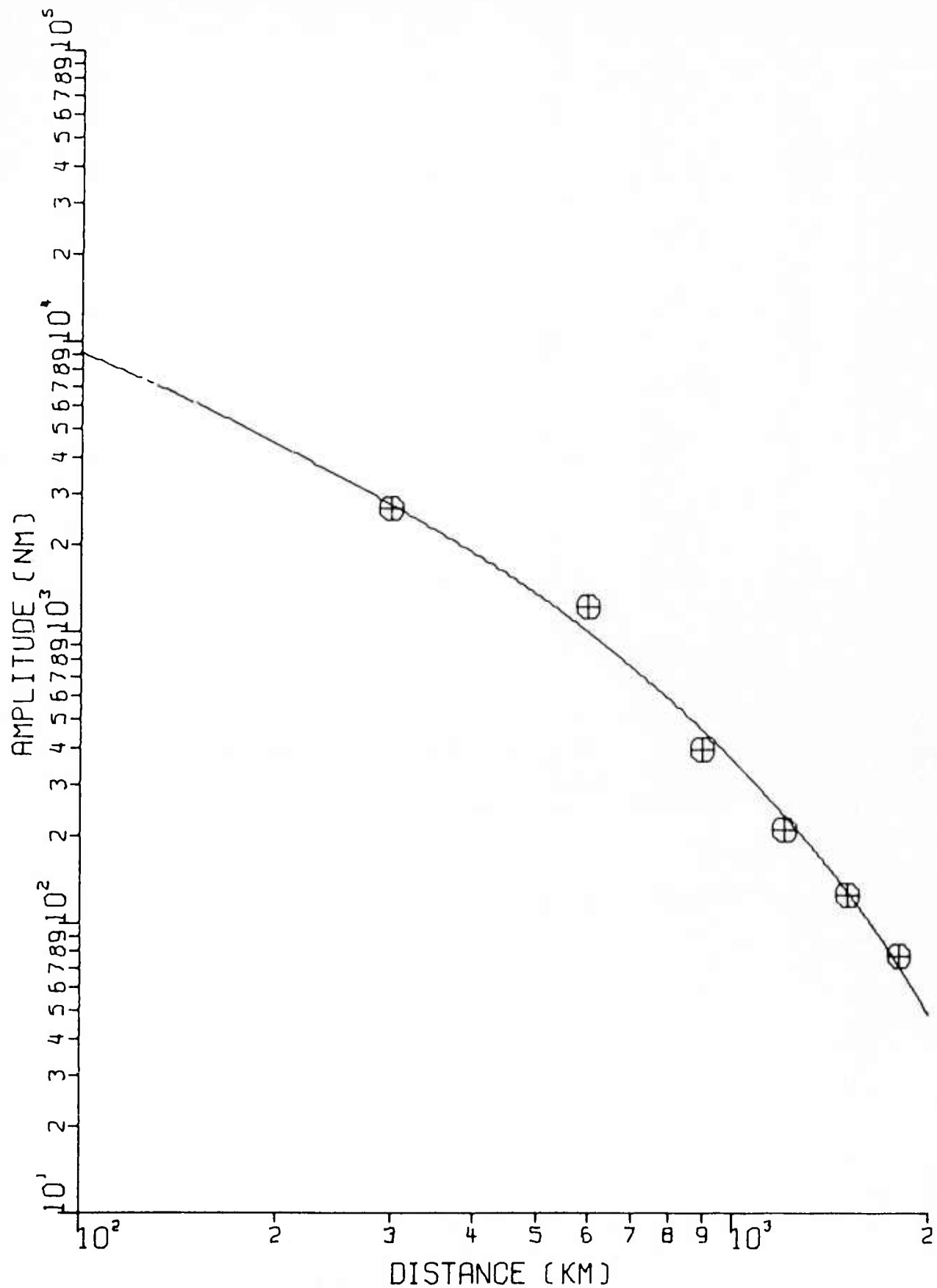


Figure 33g. depth = 10.0 km, rake = 45°, dip = 60°,
 strike = 40°: $\gamma = 0.1611$ deg
 Amplitudes of envelope maxima of synthetic
 seismograms for the high-Q soft-rock model as
 observed at various distances:

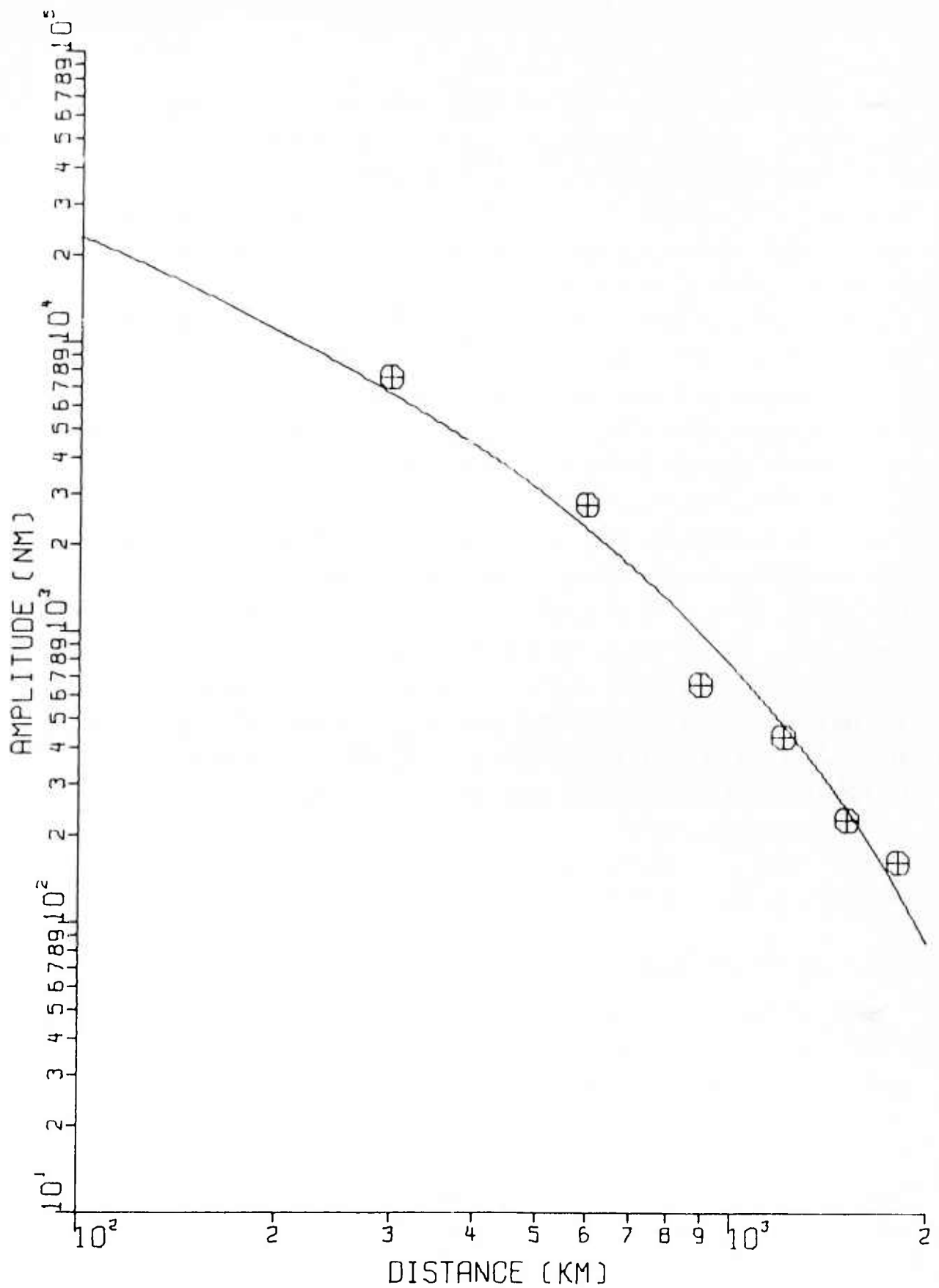


Figure 33h. depth = 10.0 km, rake = -70° , dip = 70° ,
 strike = 40° ; $\gamma = 0.1820$ deg
 Amplitudes of envelope maxima of synthetic
 seismograms for the high-Q soft-rock model as
 observed at various distances:

local structure at Yucca Flats and Pahute Mesa is presented by Barker et al. (1980a). Our synthetic seismograms are thus inadequate in that we have assumed a single earth model which is presumed to describe the structure at the source, throughout the entire propagation path, and at the receiver. Obviously, our approximation of uniform plane-parallel layers is inadequate over long distances, so our synthetics will reproduce only the gross behavior of L_g . An important phenomenon in L_g propagation is almost certainly the conversion of energy between modes, which is caused by scattering and by the departure of the structure along the propagation path from the assumed uniform model. We have made no attempt to account for even the conversion among Love-wave modes, much less the conversion between Love and Rayleigh modes which takes place in a three-dimensional scattering problem. We note that taking into account the Love-wave energy which has propagated over a large fraction of the path as (slower) Rayleigh-wave modes would extend the codas, since most of the scattering along the path occurs at shallow depths and hence tends to excite the fundamental (i.e., slowest) mode preferentially. The "scattered" fundamental mode will of course arrive at the receiver after the higher-order modes but before the direct-path fundamental mode which is prominent on our synthetics as a separate arrival in the soft-rock model. Interference between these multiple arrivals will tend to obscure the appearance of the fundamental mode as a separate phase.

Deficiency of the Model

We have mentioned that it is difficult to use L_g phase velocity as a depth discriminant since the value which is measured for C_L will vary temporally as the Airy phases of different modes arrive at different times throughout the coda. In Table IV we demonstrate this difficulty by using synthetics which were generated using a crustal model appropriate for WN-SD, a station located on thick sediments atop a shield-like structure. It is shown that the phase velocity is strongly influenced by the particular 25.6-sec time window which is chosen for making the measurement. The F-statistic is also shown to vary temporally throughout the coda, presumably depending upon whether most of the energy within the given time window propagates as pulse-like Airy

TABLE IV

Temporal Variation of the Measured L_g Phase Velocity

Depth (km)	Window Start Time (sec)*	0.8-1.2 Hz		1.0-1.4 Hz		1.2-1.6 Hz	
		F-Statistic	Phase Velocity (km/sec)	F-Statistic	Phase Velocity (km/sec)	F-Statistic	Phase Velocity (km/sec)
3.0	21	54.2	4.06	35.7	4.04	55.3	3.91
	25	57.9	4.23	31.7	4.04	50.0	3.91
	29	51.9	4.23	37.7	4.18	39.1	4.02
	33	52.3	4.23	43.2	4.04	36.8	4.02
	37	19.9	3.76	53.8	3.78	60.2	4.26
	41	63.3	4.84	89.2	4.33	122.5	4.69
	45	61.8	4.84	110.3	4.18	132.7	4.69
	49	23.0	3.91	138.6	4.18	59.0	4.69
13.0	21	86.4	3.91	54.3	4.04	65.0	4.40
	25	104.5	3.91	52.3	4.04	66.5	4.40
	29	106.7	3.91	53.5	4.04	75.0	4.40
	33	90.5	3.91	63.7	4.18	77.5	4.40
	37	65.2	3.91	78.7	4.33	39.7	4.40
	41	97.2	4.06	77.1	4.49	77.5	4.54
	45	103.5	4.06	103.4	4.49	47.8	4.54
	49	76.3	4.42	52.8	4.49	62.3	4.54
23.0	21	33.9	4.06	49.3	4.33	23.8	4.14
	25	36.4	4.06	63.1	4.33	27.6	4.40
	29	37.2	4.06	63.9	4.33	27.9	4.40
	33	23.7	4.06	31.5	4.33	24.2	4.54
	37	43.4	4.06	67.7	4.33	46.3	4.54
	41	43.8	4.06	63.4	4.33	47.8	4.54
	45	36.4	4.06	62.5	4.33	64.9	4.54
	49	92.6	4.23	95.4	4.66	40.9	4.68

* relative to an arbitrary reference point approximately 21 sec before the first motion.

phases or as dispersed wavetrains, which are less coherent across the 7.0-km long array (since our frequency bands have finite bandwidth, and hence dispersion occurs within them). We note that our assessment of the value of this depth discriminant well might change if our seismograms were sampled at the more conventional rate of 20 samples per second, in which case the time windows would be only 6.4 sec in duration and would therefore more nearly contain only single Airy phases. These shorter time windows would thus measure better the modal structure of L_g .

One would suspect that a more realistic value of the attenuation parameter γ would be obtained if we allow the shear-wave quality factor Q_β to vary with frequency. In a study involving synthesis of the Rayleigh-wave modes of L_g , Bache et al. (1980) found abnormally large values of γ for a model representing the eastern United States, a result which is compatible with the overestimation of γ which we found for the Love-wave modes in the low-Q soft-rock model. Bache et al. (1980) speculated that introducing a frequency-dependent Q_β into their earth model would result in more nearly realistic synthetic seismograms, but in a subsequent study (Bache et al., 1981) they found that making this change resulted in synthetics which still suffered from the same inadequacies as before. They concluded that scattering, rather than frequency-dependent attenuation, is the best explanation for the observed rate of decay of amplitude with distance. As we have stated, we believe the neglect of scattering to be a principal deficiency of the seismograms synthesized by modal superposition, and until some account is made for this deficiency, we are reluctant to introduce further refinements into the process such as increasing the sampling rate and the number of modes, adding more layers to the earth model, or making assumptions about the variation of Q_β with depth and with frequency.

CONCLUSIONS

We have attempted to analyze the propagation of the seismic phase L_g in order to increase our understanding of how its propagation across a tectonic shield affects its observed characteristics at the receiver. It is necessary to understand the propagation path effects in order to determine what information can be determined about the seismic source from observations of L_g . Our synthetic seismograms have involved exclusively the Love-wave modes (i.e., the SH component) of L_g , and we have thus been unable to examine seismograms corresponding to explosions, since, in theory, purely radial source functions produce no transverse motion. Restricting our study to earthquakes, we have reached certain conclusions about the propagation of L_g across shield structures:

- o There is a tendency for the phase velocity to increase with depth, but the potential use of this tendency as a seismic discriminant to identify deep events (i.e., earthquakes) is obscured by large variations in the phase velocity which are due to focal mechanisms. The measured value of the phase velocity also depends on the exact time window which is processed and, in a structure overlain by strongly attenuating sediments, on the distance from the source to the receiver.
- o A good fit to the observed amplitude-versus-distance relationship is given by Nuttli's (1973) Airy-phase formula, which matches the amplitudes of the synthetic seismograms over a greater distance range than does any simple $\Delta^{-\alpha}$ falloff. In order to use Nuttli's (1973) formula to calculate the seismic magnitude from the observed amplitude, however, it is necessary to evaluate the anelastic attenuation γ , and our attempts to estimate this parameter in an earth model with a strongly attenuating upper crust resulted in its overestimation. Although we might try varying the assumed depth dependence of Q_β , we are skeptical of being able to do so with sufficient accuracy to estimate γ adequately for any particular propagation path for which this parameter has not already been determined by direct observation.
- o Synthesis of L_g by modal superposition is inadequate, in that discrepancies between observed and predicted envelope shapes are introduced by departures of the actual earth structure, on both a regional and a purely local scale, from the assumed laterally homogeneous model consisting of plane-parallel layers. Our synthetics predict strong excitation of the fundamental mode, which will appear as a strong pulse for shallow sources in a shield model without sediments or as a later arrival in a model with a sedimentary veneer. In fact,

this strong fundamental mode is not observed, but introducing a thick, low- Q_p layer into our crustal model in order to damp it out leads to too large a value of γ . We conclude that a more likely explanation for our failure to observe the fundamental mode is that it is scattered more strongly by topography and by shallow inhomogeneities than are the higher-order modes. The effects of the propagation path structure on the observed characteristics of L_g cannot be fully understood until the scattering among modes and between Rayleigh- and Love-wave modes is taken into account. Seismogram synthesis which includes scattering would attempt to reproduce observed seismograms in a stochastic, rather than a deterministic, sense.

REFERENCES

- Bache, T. C., W. L. Rodi, and D. G. Harkrider (1978). Crustal structures inferred from Rayleigh-wave signatures of NTS explosions, Bull. Seism. Soc. Am., 68, 1399.
- Bache, T. C., H. Swanger, and B. Shkoller (1980). Synthesis of L_g in eastern United States crustal models with frequency independent Q , SSS-R-81-4668, Systems, Science and Software, La Jolla, California.
- Bache, T. C., H. J. Swanger, B. Shkoller, and S. M. Day (1981). Simulation of short period L_g , expansion of three-dimensional source simulation capabilities and simulation of near-field ground motion for the 1971 San Fernando, California, earthquake, SSS-R-81-5081, Systems, Science, and Software, La Jolla, California.
- Barker, B. W., Z. A. Der, and C. P. Mrazek (1980a). The effect of crustal structure on the regional phases P and L at NTS, In: Studies of Seismic Wave Characteristics at Regional Distances, AL-80-1, Teledyne Geotech, Alexandria, Virginia.
- Barker, B. W., Z. A. Der, and R. H. Shumway (1980b). Phase velocities of regional phases P , S , and L_g observed at the Cumberland Plateau Observatory (CPO) and LASA, In: Studies of Seismic Wave Characteristics at Regional Distances, AL-80-1, Teledyne Geotech, Alexandria, Virginia.
- Barley, B. J. (1978). On the use of seismometer arrays to locate sources of higher mode Rayleigh waves, AWRE, Blacknest, England.
- Bath, M. (1954). The elastic waves L_g and R_g along Euroasiatic paths, Arkiv. Geofys., 2, 295-324.
- Bath, M. (1968). Mathematical Aspects of Seismology, Elsevier Publishing Company, New York.
- Brune, J., and J. Dorman (1963). Seismic waves and earth structure in the Canadian shield, Bull. Seism. Soc. Am., 53, 167-210.
- Der, Z. A., A. O'Donnell, and P. J. Klouda (1981). An investigation of attenuation, scattering and site effects on regional phases, VSC-TR-81-11, Teledyne Geotech, Alexandria, Virginia.
- Gilbert, F., and G. E. Backus (1966). Propagator matrices in elastic wave and vibration problems, Geophysics, 31, 326-332.
- Gutenberg, B. (1955). Channel waves in the earth's crust, Geophysics, 20, 283-294.

REFERENCES (Continued)

- Harkrider, D. H. (1970). Surface waves in multilayered elastic media. Part II. Higher mode spectral and spectral ratios from point source in plane layered earth models, Bull. Seism. Soc. Am., 60, 1937-1987.
- Haskell, N. A. (1953). The dispersion of surface waves on multilayered media, Bull. Seism. Soc. Am., 43, 17-34.
- Kausel, E., and F. Schwab (1973). Contributions to Love wave transformation theory: earth-flattening transformation for Love waves from a point source on a sphere, Bull. Seism. Soc. Am., 63, 983-993.
- Keller, G. R., R. B. Smith, L. W. Braile, R. Hearney, and D. H. Shurbet (1976). Upper crustal structure of the eastern Basin and Range, northern Colorado Plateau, and middle Rocky Mountains from Rayleigh-wave dispersion, Bull. Seism. Soc. Am., 66, 869-876.
- Knopoff, L. (1974). Q, Rev. Geophys. Space Phys., 2, 625-660.
- Knopoff, L., F. Schwab, and E. Kausel (1973). Interpretation of L_g. Geophys. J. R. Astr. Soc., 33, 389-404.
- Knopoff, L., F. Schwab, K. Nakanishi, and F. Chang (1974). Evaluation of L_g as a discriminant among different continental crustal structures, Geophys. J. R. Astr. Soc., 39, 41-70.
- Knopoff, L., R. G. Mitchel, E. G. Kausel, and F. Schwab (1979). A search for the oceanic L_g phase, Geophys. J. R. Astr. Soc., 56, 211-218.
- Kovach, R. L., and D. L. Anderson (1964). Higher mode surface waves and their bearing on the structure of the earth's mantle, Bull. Seism. Soc. Am., 54, 161-182.
- Mantovani, E., F. Schwab, H. Liao, and L. Knopoff (1977). Teleseismic S₁: a guided wave in the mantle, Geophys. J. R. Astr. Soc., 51, 709-726.
- Mendiguren, J. A. (1977). Inversion of surface wave data in source mechanism studies, J. Geophys. Res., 82, 889-894.
- Nuttli, O. W. (1973). Seismic wave attenuation and magnitude relations for eastern North America, J. Geophys. Res., 78, 876-885.
- Oliver, J., and M. Ewing (1957). Higher modes of continental Rayleigh waves, Bull. Seism. Soc. Am., 47, 187-204.
- Oliver, J., and M. Ewing (1958a). Normal modes of continental surface waves, Bull. Seism. Soc. Am., 48, 33-49.

REFERENCES (Continued)

- Oliver, J., and M. Ewing (1958b). The effect of superficial sedimentary layers on continental surface waves, Bull. Seism. Soc. Am., 48, 339-354.
- Panza, G. F., and G. Calcagnile (1975). L , L_1 , and R from Rayleigh modes, Geophys. J. R. Astr. Soc., 40, ~~8475~~⁸487.
- Pomeroy, P. W., W. J. Best, and T. V. McEvilly (1982). Test ban treaty verification with regional data - a review, Bull. Seism. Soc. Am., 72, 589-5129.
- Press, F., and M. Ewing (1952). Two slow surface waves across North America, Bull. Seism. Soc. Am., 42, 219-228.
- Schwab, F., and L. Knopoff (1971). Surface waves on multilayered anelastic media, Bull. Seism. Soc. Am., 61, 893-912.
- Stephens, C., and B. L. Isacks (1977). Toward an understanding of S_n : normal modes of Love waves in an oceanic structure, Bull. Seism. Soc. Am., 67, 69-78.

(THIS PAGE INTENTIONALLY LEFT BLANK)

DISTRIBUTION LIST
(UNCLASSIFIED REPORTS)
DARPA FUNDED PROJECTS
(Last Revised 20 Feb 1985)

<u>RECIPIENT</u>	<u>NUMBER OF COPIES</u>
DEPARTMENT OF DEFENSE	
DARPA/GSD 1400 Wilson Boulevard Arlington, VA 22209	2
DARPA/PM 1400 Wilson Boulevard Arlington, VA 22209	1
Defense Technical Information Center Cameron Station Alexandria, VA 22314	12
Defense Intelligence Agency Directorate for Scientific and Technical Intelligence Washington, D.C. 20301	1
Defense Nuclear Agency Shock Physics Directorate/SS Washington, D.C. 20305	1
Defense Nuclear Agency/SPSS ATTN: Dr. Michael Shore 6801 Telegraph Road Alexandria, VA 22310	1
DEPARTMENT OF THE AIR FORCE	
AFGL/LW ATTN: Dr. J. Cipar Terrestrial Sciences Division Hanscom AFB, MA 01730	1
AFOSR/NPG ATTN: Director Bldg 410, Room C222 Bolling AFB, Washington D.C. 20332	1
AFTAC/TG Patrick AFB, FL 32925-6471	4
AFTAC/CA (STINFO) Patrick AFB, FL 32925-6441	1
AFWL/NTESC Kirtland AFB, NM 87171	1

DEPARTMENT OF THE NAVY

NORDA
ATTN: Dr. J. A. Ballard
Code 543
NSTL Station, MS 39529

1

DEPARTMENT OF ENERGY

Department of Energy
ATTN: Dr. F. Dickerson (DP-52)
International Security Affairs
1000 Independence Avenue
Washington, D.C. 20545

1

Lawrence Livermore National Laboratory
ATTN: Dr. J. Hannon and Dr. M. Nordyke
University of California
P.O. Box 808
Livermore, CA 94550

2

Los Alamos Scientific Laboratory
ATTN: Dr. K. Olsen
P.O. Box 1663
Los Alamos, NM 87544

1

Sandia Laboratories
ATTN: Mr. P. Stokes
Geosciences Department 1255
Albuquerque, NM 87115

1

OTHER GOVERNMENT AGENCIES

Central Intelligence Agency
ATTN: Dr. L. Turnbull
OSI/NED, Room 5G48
Washington, D.C. 20505

1

U.S. Arms Control and Disarmament Agency 2
ATTN: Mrs. M. Hoinkes
Division of Multilateral Affairs
Room 5499
Washington, D.C. 20451

U.S. Geological Survey 1
ATTN: Dr. T. Hanks
National Earthquake Research Center
345 Middlefield Road
Menlo Park, CA 94025

U.S. Geological Survey 1
ATTN: Dr. Robert Masse
Global Seismology Branch
Box 25046, Stop 967
Denver Federal Center
Denver, CO 80225

UNIVERSITIES

University of California, Berkeley 1
ATTN: DR. T. McEvelly
Department of Geology and Geophysics
Berkeley, CA 94720

California Institute of Technology 1
ATTN: Dr. D. Harkrider
Seismological Laboratory
Pasadena, CA 91125

University of California, San Diego 1
ATTN: Dr. J. Orcutt
Scripps Institute of Oceanography
La Jolla, CA 92093

Columbia University 1
ATTN: Dr. L. Sykes
Lamont-Doherty Geological Observatory
Palisades, NY 10964

Massachusetts Institute of Technology 3
ATTN: Dr. S. Soloman, Dr. N. Toksoz, Dr. T. Jordan
Department of Earth and Planetary Sciences
Cambridge, MA 02139

University of Nevada, Reno 1
ATTN: Dr. A. Ryall
Seismological Laboratory
Reno, NV 89557

The Pennsylvania State University 1
ATTN: Dr. S. Alexander
Department of Mineral Sciences
University Park, PA 16802

Southern Methodist University 1
ATTN: Dr. E. Herrin
Geophysical Laboratory
Dallas, TX 75275

CIRES 1
ATTN: Dr. C. Archambeau
University of Colorado
Boulder, CO 80309

Georgia Institute of Technology 1
ATTN: Professor Anton Dainty
The School of Geophysical Sciences
Atlanta, GA 30332

St. Louis University 1
ATTN: Dr. O. Nuttli
Department of Earth and Atmospheric Sciences
3507 Laclede
St. Louis, MO 63156

DEPARTMENT OF DEFENSE CONTRACTORS

Applied Research Associates, Incorporated 1
ATTN: Dr. N. Higgins
2101 San Pedro Boulevard North East
Suite A
Albuquerque, NM 87110

Applied Theory, Incorporated 1
ATTN: Dr. J. Trullio
930 South La Brea Avenue
Suite 2
Los Angeles, CA 90036

Center for Seismic Studies 2
ATTN: Dr. Carl Romney, and Dr. William Dean
1300 N. 17th Street, Suite 1450
Arlington, VA 22209

ENSCO, Incorporated 1
ATTN: Mr. G. Young
5400 Port Royal Road
Springfield, VA 22151

ENSCO, Incorporated 1
ATTN: Dr. R. Kemerait
1930 Highway A1A
Indian Harbour Beach, FL 32937

Pacific Sierra Research Corporation ATTN: Mr. F. Thomas 12340 Santa Monica Boulevard Los Angeles, CA 90025	1
R&D Associates ATTN: Dr. E. Martinelli P.O. Box 9695 Marina del Rey, CA 90291	1
Rockwell International ATTN: Dr. B. Tittmann 109 Camino Dos Rios Thousand Oaks, CA 91360	1
Gould Incorporated ATTN: Mr. R. J. Woodard Chesapeake Instrument Division 6711 Baymeado Drive Glen Burnie, MD 21061	1
Rondout Associates, Incorporated ATTN: Dr. P. Pomeroy P.O. Box 224 Stone Ridge, NY 12484	1
Science Applications, Incorporated ATTN: Dr. T. Bache P.O. Box 2351 La Jolla, CA 92038	1
Science Horizons ATTN: Dr. T. Cherry and Dr. J. Minster 710 Encinitas Blvd Suite 101 Encinitas, CA 92024	2
Sierra Geophysics, Incorporated ATTN: Dr. R. Hart and Dr. G. Mellman 15446 Bell-Red Road Redmond, WA 98052	2
SRI International 333 Ravensworth Avenue Menlo Park, CA 94025	1

S-Cubed, A Division of
Maxwell Laboratories Inc.
Attn: Dr. Steven Day
P.O. Box 1620
La Jolla, CA 92038 1

S-Cubed, A Division of
Maxwell Laboratories Inc.
Attn: Mr. J. Murphy
11800 Sunrise Valley Drive
Suite 1212
Reston, VA 22091 1

Teledyne Geotech
ATTN: Dr. Z. Der & Mr. W. Rivers
314 Montgomery Street
Alexandria, VA 22314 2

Woodward-Clyde Consultants
ATTN: Dr. Larry Burdick
556 El Dorado St
Pasadena, CA 91105 1

Weidlinger Associates
ATTN: Dr. J. Isenberg
3000 Sand Hill Road
Menlo Park, CA 94025 1

NON-U.S. RECIPIENTS

National Defense Research Institute
ATTN: Dr. Ola Dahlman
Stockholm 80, Sweden 1

Blacknest Seismological Center
ATTN: Mr. Peter Marshall
Atomic Weapons Research Establishment
UK Ministry of Defense
Brimpton, Reading RG7-4RS
United Kingdom 1

NTNF NORSAR
ATTN: Dr. Frode Ringdal
P.O. Box 51
N-2007 Kjeller
Norway 1

To be determined by the project office 6